Infrared and Terahertz Near-Field Spectroscopy and Microscopy on 3*d* and 4*d* Correlated Electron Materials

A Dissertation Presented

by

Jiawei Zhang

to

The Graduate School

in Partial Fulfillment of the

Requirements

for the Degree of

Doctor of Philosophy

in

Physics

Stony Brook University

August 2019

Stony Brook University

The Graduate School

Jiawei Zhang

We, the dissertation committee for the above candidate for the

Doctor of Philosophy degree, hereby recommend

acceptance of this dissertation.

Mengkun Liu – Dissertation Advisor

Professor, Department of Physics and Astronomy

Philip B. Allen - Chairperson of Defense

Professor Emeritus and Research Professor, Department of Physics and Astronomy

Laszlo Mihaly – Committee Member

Professor, Department of Physics and Astronomy

Dmitri Kharzeev – Committee Member

Distinguished Professor, Department of Physics and Astronomy

Qiang Li – External Committee Member

Group Leader, Condensed Matter Physics and Materials Sciences Division, Brookhaven National Laboratory

This dissertation is accepted by the Graduate School

Richard Gerrig

Interim Dean of the Graduate School

Abstract of the Dissertation

Infrared and Terahertz Near-field Spectroscopy and Microscopy on 3*d* and 4*d* Correlated Electron Materials

by

Jiawei Zhang

Doctor of Philosophy

in

Physics

Stony Brook University

2019

The electromagnetic waves in the far infrared and terahertz range have ubiquitous applications to the optical characterization of solid-state materials in which numerous physical phenomena occur within the energy range below ~ 100 meV (molecular rotation, exciton transition, superconducting gap opening, etc.). Conventional infrared and terahertz characterization methods have been suffering from low spatial resolution due to optical diffraction effects. This thesis presents a new type of micro-imaging technique named scattering-type scanning near-field optical microscopy (s-SNOM) which can reach deep subwavelength spatial resolution regardless of the wavelength of probing light. The working principle of far infrared s-SNOM is introduced with an illustration of two experimental measurements on the insulator-to-metal phase transition (IMT) of transition metal oxides Ca_2RuO_4 and VO_2, the images of phase boundaries on sample surfaces show exotic nanoscale phase patterns, revealing the competition between strain and domain wall energy, showing the complex interplay between non-equilibrium electronic and lattice steady states. The second part of the thesis discusses the terahertz time domain spectroscopy (THz-TDS) and optical-pump-terahertz-probe (OPTP) schemes. An experiment is demonstrated to explore the ultrafast electronic dynamics of correlated electron materials $V_{1-x}Nb_xO_2$ thin films, revealing a novel way of tuning electron-electron and electron-phonon interaction dynamics. The last part of the thesis reports our recent progress in THz s-SNOM with a demonstration of near field imaging on graphene. Measurement suggests that a single layer graphene acts as a perfect terahertz reflector in the near-field regime due to high-momentum effects. Conclusions and potential works for the future are mentioned at last.

Table of Contents

List of Figures ... vi
List of Tables ... viii
Acknowledgements ... ix
Publications ... x
Chapter 1 ... 1
Introduction ... 1
1.1 Applications of Infrared and Terahertz Light ... 1
Chapter 2 ... 5
Infrared Scattering-type Scanning Near-field Optical Microscopy (IR s-SNOM) ... 5
2.1 History ... 5
2.2 Working Principle of IR s-SNOM ... 6
2.2.1 System Setup and Operation ... 6
2.2.2 Dipole Model versus Monopole Model ... 9
2.2.3 Background Free Detection ... 11
Chapter 3 ... 16
IR s-SNOM Experiments ... 16
3.1 IR s-SNOM on Ca_2RuO_4 single crystal ... 16
3.1.1 Introduction ... 16
3.1.2 Experiments ... 17
3.1.3 Analysis of Insulator-Metal Phase Boundary ... 22
3.1.4 Conclusions ... 28
3.2 IR s-SNOM on VO_2 film ... 28
3.2.1 Introduction ... 28
3.2.2 Methodology for Nanoscale Permittivity Extraction ... 30
3.2.3 Nanoscale Permittivity Extraction from Infrared s-SNOM Imaging of VO_2 ... 33
3.2.4 Conclusions ... 37
Chapter 4 ... 39
Terahertz Time Domain Spectroscopy ... 39
4.1 Introduction ... 39
4.2 Terahertz Generation and Detection ... 40
4.2.1 Terahertz Time Domain Spectroscopy ... 40
4.2.2 Optical Pump Terahertz Probe (OPTP) ... 47

4.3 Optical Pump Terahertz Probe on $V_{1-x}Nb_xO_2$ 50
4.3.1 Introduction 50
4.3.2 Experiments on Electric and Optical Properties 51
4.3.3 Discussions 58
4.3.4 Conclusion 60
Chapter 5 62
Terahertz Near Field Microscopy and Spectroscopy 62
5.1 Introduction 62
5.2 THz s-SNOM on Graphene 65
5.2.1 Introduction 65
5.2.2 THz s-SNOM on single and multi-layer graphene samples 68
5.2.3 Analysis 72
5.2.4 Conclusions 74
Chapter 6 75
Conclusions and Outlook 75
Bibliography 77

List of Figures

Figure 1.1: Fraunhofer diffraction pattern of a circular aperture 2
Figure 1.2: Rayleigh and Sparrow criteria for the limit of spatial resolution 3
Figure 2.1: Synge's proposal and first experimental demonstration by Nicholls. 5
Figure 2.2: Schematic setup of IR s-SNOM. Red arrows represent light direction 7
Figure 2.3: Schematic setup of the readout systems. 8
Figure 2.4: Light path of guide beam in the IR s-SNOM setup 9
Figure 2.5: Dipole model for near-field interaction 10
Figure 2.6: Monopole model for near field interaction 10
Figure 2.7: Scheme to suppress background signal.. 12
Figure 2.8: Non-interference, Homodyne and Pseudo-Heterodyne for background free detection 13
Figure 3.1: DC transport characterization and optical photographs of a Ca_2RuO_4 bulk single crystal at different stages of the IMT. 19
Figure 3.2: IR nano spectra and IR s-SNOM imaging of the L-S' phase boundary 21
Figure 3.3: Current dependent near-field phonon response at currents lower than those needed to initiate the IMT 22
Figure 3.4: Oriented stripe formation across the PB 25
Figure 3.5: Topography and progression/regression of the PB 27
Figure 3.6: The quantitative relationship between predicted near-field signal S_3 and optical permittivity calculated using three different theoretical models 32
Figure 3.7: Temperature dependent evolution of metallic stripes in VO_2 thin films 34
Figure 3.8: Self-consistent extraction of spatially resolved optical permittivities throughout a metallic domain in the IMT of VO_2 35
Figure 3.9: X-ray diffraction study and strain simulation of VO_2 films 37
Figure 4.1: Scheme of optical rectification for terahertz generation. 40
Figure 4.2: Scheme of terahertz time domain spectroscopy (THz-TDS). 41
Figure 4.3: Absorption of green and blue light by Ti: sapphire crystals and emission of near infrared light 41
Figure 4.4: Scheme of chirped pulse amplification (CPA). 42
Figure 4.5: Working principle of a stretcher to expand the seeding pulses in time duration. 43
Figure 4.6: ZnTe crystal used for electro-optical sampling 44
Figure 4.7: Synchronization between THz and gate pulses. 44
Figure 4.8: Measured THz time domain spectroscopy and Fourier transformed spectrum 45
Figure 4.9: THz wave transmission through a sample 46
Figure 4.10: Scheme of optical pump terahertz probe (OPTP). 47
Figure 4.11: Time relation of the pump, THz and gate pulses. The pump pulses are chopped at 500 Hz 48
Figure 4.12: Electron energy redistribution and relaxation during the ultrafast carrier dynamics. 49
Figure 4.13: Growth rate of $V_{1-x}Nb_xO_2$ films (nm/min) as a function of film composition. 52
Figure 4.14: Raman and X-ray spectra of $V_{0.45}Nb_{0.55}O_2$ film 54
Figure 4.15: Electrical conductivity and photoinduced conductivity change of $V_{1-x}Nb_xO_2$ as a function of Nb concentration x 56

Figure 4.16: Optically induced THz photoconductivity change ($\Delta\sigma$) of $V_{1-x}Nb_xO_2$ films 57
Figure 5.1: Terahertz s-SNOM on semiconductor transistors. 62
Figure 5.2: Structure of photoconductive antenna for THz generation. 63
Figure 5.3: Image and structure of photoconductive antenna for THz generation. 64
Figure 5.4: Comparison between far field and near field spectrum and measurement setup on gold. 65
Figure 5.5: Schematic of the THz s-SNOM setup 67
Figure 5.6: AFM topography and THz near-field (S_2) mapping of graphene on SiO_2 69
Figure 5.7: Single layer graphene dispersion relation 71

List of Tables

Table 3.1: Dielectric constant of VO_2 film on sapphire substrate measured by ellipsometry 33
Table 3.2: Dielectric constant of V_2O_3 film on sapphire substrate measured by ellipsometry 33
Table 4.1: Optimized deposition condition parameters for VO_2 and NbO_2 films on sapphire (0001) substrates 52

Acknowledgments

I want to express the highest gratitude to my advisor Mengkun Liu for his ebullient support and sagacious guidance to my career and life. As a newly founded group since the spring of 2015, we worked together to build our lab from scratch during which I learned numerous knowledge and experimental experiences from him. It is his genius, creativity and enthusiasm in physics that ensure the success of my research projects, encouraging me and every other group member in the pursuit of unprecedent discoveries. More importantly, from his integrity and charm of personality, I am learning how to establish a good communication with other people. His extensive collaborations give me many opportunities to broad my view in the most prestigious research institutes around the world. It's my great fortune and honor to be his student both in and after my PhD program.

I also want to express my special thanks to Professor Jacobus Verbaarschot. It was his encouragement at the end of 2013 that made I decide to pursue a PhD degree in physics, the precondition of everything happened since then.

I would like to thank Prof. Matthew Dawber for his kind instructions and help to me in his group.

I would also like to thank my colleagues Stephanie Gilbert Corder, John Logan, Thomas Ciavatti, Xinzhong Chen and Ziheng Yao. It's our efforts that lead to the setup of the far field terahertz system. Special acknowledgement to Thomas for his primary contributions to the terahertz near-field system, and to Xinzhong and Ziheng for so much help in my experiments and lives.

I would like to extend my thanks to my collaborators: Scott Mills and Haiming Deng in Professor Xu Du's group, Qiang Han in Professor Andrew Millis's group and Mohammed Yusuf in Professor Matthew Dawber's group. Fanwei Liu in Professor Xi Chen's group. Chanchal Sow in Professor Yoshiteru Maeno's group. They help me gaining a lot of knowledge outside my research area.

Moreover, I would like to mention the short visitors to our group: Kongtao Chen, Leo Lo, William Zheng and Yanxing Li. Their contributions are also important.

I would like to thank my parents and grandparents for their love and supports, and with deepest miss of grandma Changzhen Miao forever.

Finally, I want to thank the committee members Prof. Philip B. Allen, Laszlo Mihaly, Dmitri Kharzeev and Qiang Li for their precise time on my thesis and defense.

Publications (2017-2019)

First Co-authors are marked with *

1. **Zhang, J**.; McLeod, A. S.; Han, Q.; Chen, X.; Bechtel, H. A.; Yao, Z.; Gilbert Corder, S. N.; Ciavatti, T.; Tao, T. H.; Aronson, M.; Carr, G.; Martin, M.; Sow, C.; Yonezawa, S.; Nakamura, F.; Terasaki, I.; Basov, D.; Millis, A.; Maeno, Y. and Liu, M. Nano-Resolved Current-Induced Insulator-Metal Transition in the Mott Insulator Ca_2RuO_4. *Phys. Rev. X* **2019**, *9* (1), 011032.

2. **Zhang, J**.; Chen, X.; Mills, S.; Ciavatti, T.; Yao, Z.; Mescall, R.; Hu, H.; Semenenko, V.; Fei, Z.; Li, H.; Perebeinos, V.; Tao, H.; Dai, Q.; Du, X. and Liu, M. Terahertz Nanoimaging of Graphene. *ACS Photonics* **2018**, *5* (7), 2645–2651.

3. Dai, S.*; **Zhang, J.***; Ma, Q.; Kittiwatanakul, S.; McLeod, A.; Chen, X.; Corder, S. G.; Watanabe, K.; Taniguchi, T.; Lu, J.; et al. Phase-Change Hyperbolic Heterostructures for Nanopolaritonics: A Case Study of HBN/VO_2. *Adv. Mater.* **2019**, *31* (18), 1900251.

4. Wang, Y.*; **Zhang, J.***; Ni, Y.; Chen, X.; Mescall, R.; Isaacs-Smith, R.; Comes, R.; Kittiwatanakui, S.; Wolf, S.; Lu, J.; and Liu, M.; Structural, transport, and ultrafast dynamic properties of $V_{1-x}Nb_xO_2$ thin films. *Phys. Rev. B* **2019**, *99* (24), 245129.

5. Gilbert Corder, S. N.; Jiang, J.; Chen, X.; Kittiwatanakul, S.; Tung, I.-C.; Zhu, Y.; **Zhang, J**.; Bechtel, H. A.; Martin, M. C.; Carr, G. L.; Lu, J.; Wolf, S.; Wen, H.; Tao, T. and Liu, M. Controlling Phase Separation in Vanadium Dioxide Thin Films via Substrate Engineering. *Phys. Rev. B* **2017**, *96* (16), 161110.

6. Yao, Z.; Semenenko, V.; **Zhang, J.**; Mills, S.; Zhao, X.; Chen, X.; Hu, H.; Mescall, R.; Ciavatti, T.; March, S.; et al. Photo-Induced Terahertz near-Field Dynamics of Graphene/InAs Heterostructures. *Opt. Express* **2019**, *27* (10), 13611.

7. Gilbert Corder, S. N.; Chen, X.; Zhang, S.; Hu, F.; **Zhang, J**.; Luan, Y.; Logan, J. A.; Ciavatti, T.; Bechtel, H. A.; Martin, M. C.; Aronson, M.; Suzuki, H.; Kimura, S.; Iizuka, T.; Fei, Z.; Imura, K.; Sato, N.; Tao, T. and Liu, M. Near-Field Spectroscopic Investigation of Dual-Band Heavy Fermion Metamaterials. *Nat. Commun.* **2017**, *8* (1), 2262.

8. Bolmatov, D.; Soloviov, D.; Zav’yalov, D.; Sharpnack, L.; Agra-Kooijman, D. M.; Kumar, S.; **Zhang, J**.; Liu, M. and Katsaras, J. Anomalous Nanoscale Optoacoustic Phonon Mixing in Nematic Mesogens. *J. Phys. Chem. Lett.* **2018**, *9* (10), 2546–2553.

Chapter 1

Introduction

Applications of Infrared and Terahertz Light

Infrared imaging technology has abundant applications in the fast-evolving fields in science and industry. Since the invention of infrared cameras during World War II, both active and passive infrared detectors have been widely applied in material sensing and energy monitoring, with decades of improvements of performance and reduction of cost. Infrared light covers a broad range in wavelength, ranging from ~1 μm to ~1000 μm with unique optical properties in specific spectral range. For example, the short-wavelength infrared (SWIR, 0.8 μm - 1.7 μm) sensors are commonly used in haze transmission photography due to weaker scattering of infrared light by haze particles[1]. Satellite-based SWIR hyperspectral imaging can clearly distinguish between green vegetation and minerals due to the strong scattering by cellular walls in interior cells[2]. Mid-wavelength infrared (MWIR, 1.8 μm - 6 μm) light has been widely applied to the identification of various gas molecules[3]. Absorption in this range happens when the electric dipole moment of a molecule changes due to molecular rotational-vibrational excitation. The spectral characteristics of CO_2 allow monitoring of CO_2 flow by MWIR cameras. This is vital to control of the greenhouse effect. Long-wavelength infrared (LWIR, 6 μm - 10 μm) light coincides with the peak of blackbody radiation of room temperature objects and has been widely used for monitoring human body temperature and room heat dissipation.

The last few decades have witnessed the spring-up of intense research in terahertz (THz) wavelength range (10 um – 1000 um), with a series of breakthroughs in the generation and detection methods. The terahertz wireless short-range communication can potentially meet the rapidly increasing demand for higher bandwidth and faster transmission rates, up to a few hundred Gbps[4]. THz and sub-millimeter wave have been applied to security scanning in airports, thanks to the high transmission of fibers and high reflection of metals, and unlike ionizing radiations such as X-rays, terahertz wave are less harmful to human bodies[5]. Since biomolecules and water has unique characteristic absorption features related to the breakage and formation of hydrogen bonds in the terahertz range. Bio-sensors are being developed for the diagnosis of tumors containing higher water concentration than normal tissues[6], [7]. Further applications include non-destructive evaluation of coated composites, pharmaceutical process monitoring, art conservation, and fault isolation for microelectronics[6].

One of the major interests in infrared and terahertz imaging is in microscopy, since the structures of many materials, as well as physical and chemical phenomena can only be observed on a sub-micrometer scale. High resolution microscopes in the visible range have been applied to observe biological cells as well as integrated circuits. To image even smaller structures such as proteins, viruses, and electronic structures at scales smaller than 200 nm, conventional optical microscopes are insufficient. For the imaging of objects with optical characteristics in the infrared and terahertz range, a corresponding microscopy is necessary which shines light at a certain wavelength onto the sample surface and detects the outgoing light. However, with increasing wavelength, the fundamental limit on spatial resolution becomes more and more serious. As demonstrated in Fig. 1.1, any conventional microscope is accompanied with a circular aperture. The impinging light from a point source forms a diffraction pattern in a distant image screen which is composed of a series of concentric circles called Airy disks [8].

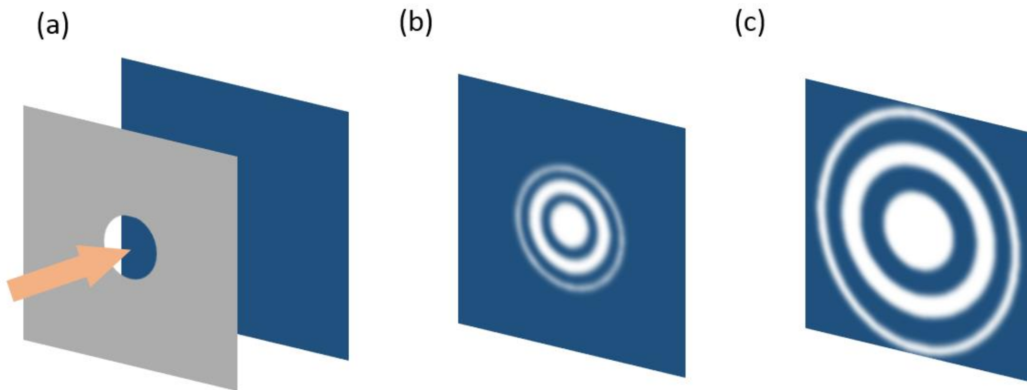

Figure 1.1: Fraunhofer diffraction pattern of a circular aperture. (a) Schematic setup of the image of incoming plane wave through a circular aperture. Airy pattern with (b) large and (c) small aperture sizes.

The central circular spot with maximum light intensity is called an Airy disk, with radius defined by the distance between the first dark ring and the center. This can be express as:

$$r = 1.22\frac{R\lambda}{D}, \tag{1.1}$$

where D is the diameter of the aperture, R is the distance between the aperture and

screen, and λ is the wavelength. Now suppose we have two closely separated point sources of light. Their Airy patterns through a microscope will partially overlap. The highest spatial resolution of such microscope is dictated by the Rayleigh criterion: two points can be barely distinguished when the center of the first point's Airy disk coincides with the first dark ring of the second point's Airy disk. According to this criterion, the minimum resolvable center-to-center spatial separation of two points can be derived:

$$\Delta l = 1.22 \frac{f\lambda}{nD}. \tag{1.2}$$

Here f is the focal length of objective lens and n is the index of refraction of the medium between the point sources and images.

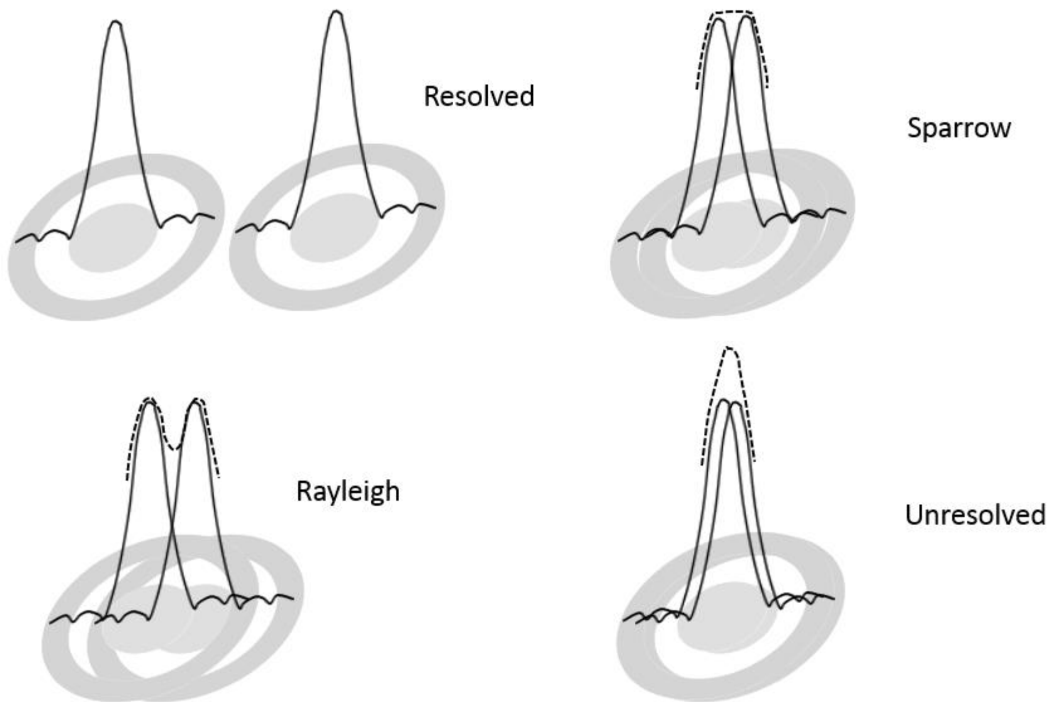

Figure 1.2: Rayleigh and Sparrow criteria for the limit of spatial resolution. Sparrow criteria corresponds to a further decrease of points distance until the central dip of two Airy patterns disappears.

According to Eq. 1.2, the increase of spatial resolution can be realized either by using shorter wavelength such as ultraviolet (UV) light, or by improving the structure of the microscope. Both have numerous engineering difficulties.

The advent of scanning probe microscopy (SPM) in the 1980s has provided people with unpreceded ability to observe various properties of material surfaces with nanometer spatial resolution. Examples are topography (AFM), electron density of state (STM), work function (KPFM), and magnetic domains (MFM). The general working principle of SPM is to apply a very sharp tip (nanometer or even atomic scale) on the sample surface with a short distance and detect the surface-tip interaction while raster-scanning either the tip or sample stage. The combination of optical system and SPM leads to the birth of near-field optical microscopy with deep sub-wavelength resolution[9].

In this thesis, Chapter 2 introduces infrared scattering-type scanning near-field microscopy (IR s-SNOM) in chapter 2. It gives an overview of the development of near field optics, Then the detailed working principle and experimental system setup will be presented. I will compare two theoretical models: Dipole Model and Monopole Model, which are used to compared to simulate tip-sample interaction under the illumination of light. Detection and modulation techniques to get rid of background radiation are described. In chapter 3, I will demonstrate the IR nano-imaging of insulator-to-metal phase transition (IMT) in two representative correlated electron materials VO_2 and Ca_2RuO_4. This shows the delicate interplay between the electronic states and lattice structures. The next part of the thesis is about terahertz techniques. Chapter 4 is about ultrafast terahertz spectroscopy generated by femtosecond pulse laser systems. Experimental measurement of terahertz ultrafast dynamics of $V_{1-x}Nb_xO_2$ thin films is reported. Chapter 5 describes recent progress of our hand-made terahertz s-SNOM. State-of-the-art performance is shown by preliminary experiments on graphene and semiconductor materials. A conclusion and future directions are mentioned in Chapter 6.

Chapter 2

Infrared Scattering-type Scanning Near-field Optical Microscopy (IR s-SNOM)

2.1 History

The idea of using near-field evanescent wave confined to the surface of object for microscopy dates to 1928 when Edward Hutchinson Synge proposed to bring an opaque screen with a small hole or a sharp metallic aperture probe close to the sample surface for optical imaging[10]. The incoming light from a local region with similar size as the aperture will be scattered in all directions and be focused by an appropriate microscope to the eye of an observer, while light from other regions of the sample is totally blocked. By scanning the aperture over the sample surface, an image with sub-wavelength resolution can be achieved.

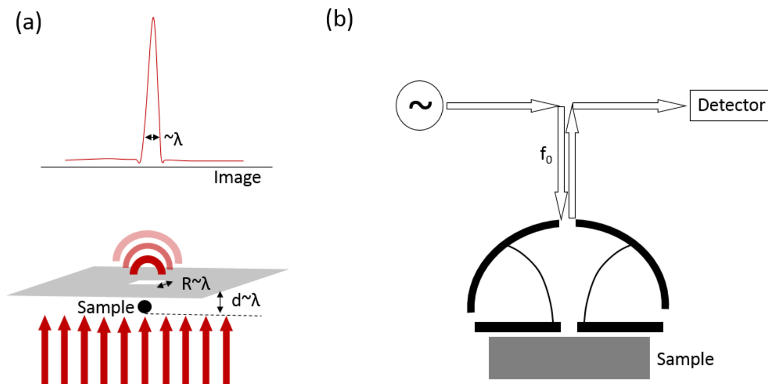

Figure 2.1: (a) Synge's proposal for near-field optical microscopy in 1928. (b) Simplified diagram of the first experimental demonstration in 1972 by Ash and Nicholls.

However, due to the limitation of experimental techniques, the first near-field microscope wasn't invented until 1972 when Ash and Nicholls used 10 GHz microwaves (30 mm) with an aperture of 1.5 mm to image metallic characters with line width around 2 mm, in which a $\lambda/15$ resolution is achieved[11].

The first few optical near field microscopes using apertures were invented in the 1980s by several independent groups and the technique was later termed as SNOM (scanning near field optical microscopy). In 1991 Eric Betzig managed to fabricate an aperture probe at the end of a thermally pulled quartz fiber coated with metal, resulting a widespread application and commercialization in the market. The application of scattering-type SNOM using a metallic tip without aperture began in 1992 by Specht. The apertureless tip is generally used to confine incoming light into a localized region, resulting in near field interaction with the sample surface and scatter light away to the detectors. In 2000, Hillenbrand and Keilmann used IR s-SNOM to study the phonon resonance on SiC sample, showing that the near-field coupling is highly sensitive to the material properties[12]. The experimental results were followed by a lot of theoretical works trying to model the light-tip-sample interaction. In 1998 Novotny proposed that the electric field of the incident light is strongly enhanced between the tip and sample, and the signal containing the near field interaction is then coupled out by the same tip as far field radiation. Details of two interaction models (dipole and monopole) will be discussed in the following sections.

2.2 Working Principle of IR s-SNOM

2.2.1 System Setup and Operation

The schematic setup of IR s-SNOM system is shown in Fig. 2.2. Continuous far infrared light with tunable wavelength from ~10 μm to ~11 μm is generated by a CO_2 laser. The generated light is guided to a beam splitter made of ZnSe single crystal. The reflective part of light is then focused on to the AFM tip which is scanning on a sample surface at tapping frequency Ω. The transmitted light through the beam splitter is reflected by a reference mirror. The back scattered light from the tip-sample system travels through the beam splitter again and collected by a HgCdTe IR detector together with the reference beam from mirror.

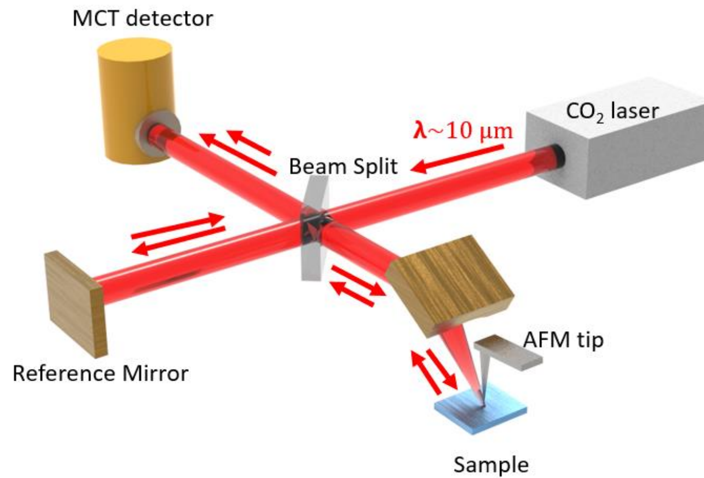

Figure 2.2: Schematic setup of IR s-SNOM. Red arrows represent light direction.

The setup of the control system is illustrated in Fig. 2.3. The collected IR signal produces photo-current in the light sensing material and be amplified and converted to output voltage. The output voltage is connected to the input 1 of a high frequency lock-in amplifier (HF2LI, Zurich Instruments). The tapping frequency Ω signal generated by an atomic force microscope (NT-MDT) is guided to the input 2 of the lock-in amplifier for the demodulation of the output voltage from the detector. The demodulated signal at desired harmonics of tip oscillation frequency is fed back to the AFM controlling software to plot an optical image as the tip is scanning over the sample surface.

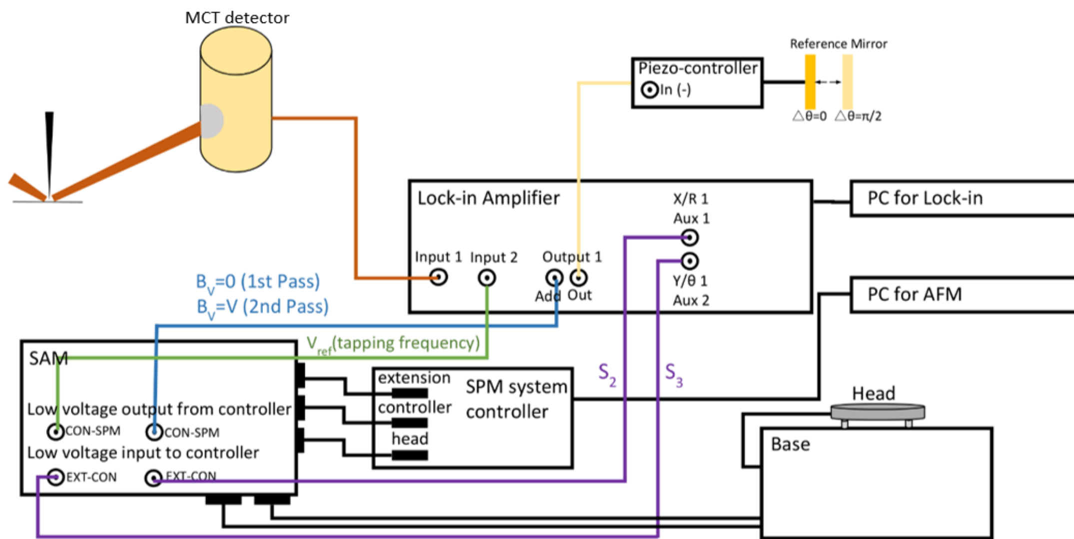

Figure 2.3: Schematic setup of the readout systems. The AFM tip and head are plotted separately for better illustration.

The alignment of the optical system is non-trivial due to the invisibility of IR light. The use of a visible guide beam will ease the setting up work. The guide beam (often a green or red laser diode) is firstly collimated with the IR beam before entering the beam split. The beam splitter is a ZnSe single crystal with one face coated with anti-reflection coating for 10 μm. Fig. 2.4 shows the light path of the guide beam which is not affected by the anti-reflection coating. The guide beam is split into several beams due to multiple refraction and internal reflection, the IR beam will only be following the solid lines. The power ratio of the transmitted IR beam through the beam splitter to that reflected is around 100:1. The reason for using the reference mirror will be explained below in Section 2.2.3.

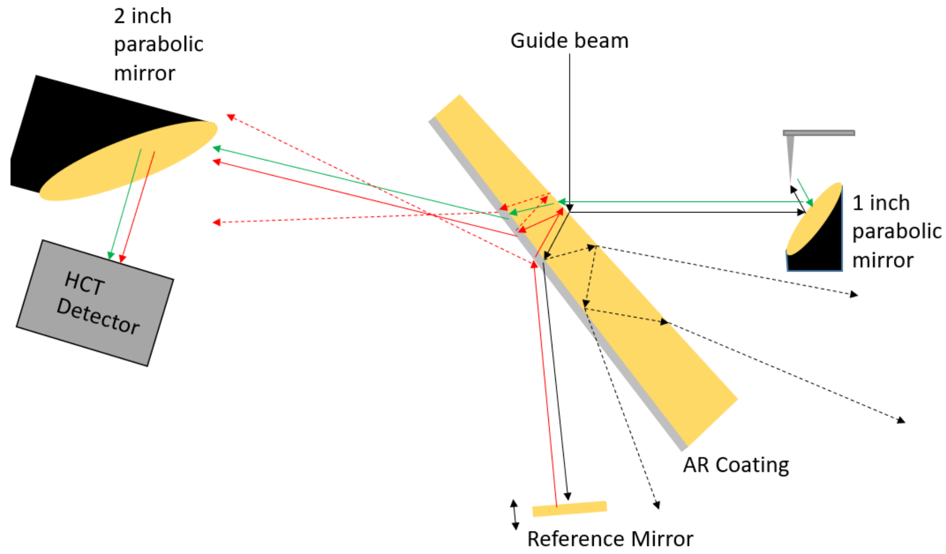

Figure 2.4: Light path of guide beam in the IR s-SNOM setup.

2.2.2 Dipole Model versus Monopole Model

Two models simulating the interaction between tip and sample will be compared[9]. In the dipole model, the electric field E_0 of the incident IR light will polarize a point dipole moment at the tip apex:

$$p = \alpha E_0, \tag{2.1}$$

where α is the dipole polarizability and $\alpha = 4\pi R^3 \frac{\epsilon - 1}{\epsilon + 2}$, and ϵ refers to the dielectric constant of the tip which is usually silicon coated with metal. The induced dipole moment will generate a "mirror dipole" in the sample surface:

$$p' = \beta p \tag{2.2}$$

Here $\beta = \frac{\epsilon_s - 1}{\epsilon_s + 1}$ is called "reflection coefficient" and ϵ_s is the dielectric constant of sample surface. The mirror dipole affects the tip dipole back again to further enhance p, which in turn increase p'. The multiple interactions lead to the final expression of the effective polarizability:

$$\alpha_{eff} = \frac{\alpha}{1 - \frac{\alpha\beta}{16\pi(R+H)^3}} \tag{2.3}$$

Which is proportional to the electric field of scattered light. Here R and H are defined in the Fig. 2.5.

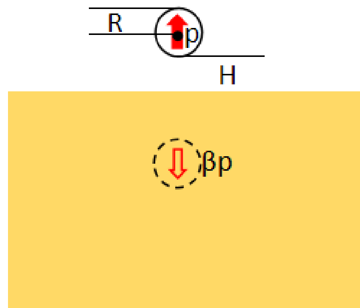

Figure 2.5: Dipole model for near-field interaction.

The monopole model, on the other hand, consider the tip apex as a spheroid. As shown in Fig. 2.6, the incident electric field E_0 creates an extended dipole q_0 and - q_0, which induces a second dipole q_i and – q_i. Here only -q_i participates in the near field interaction.

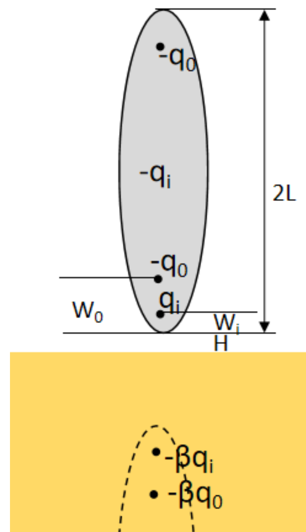

Figure 2.6: Monopole model for near field interaction.

Similar to the dipole model, the charge q_0 induces a mirror dipole $q_0'=-\beta q_0$ inside the sample. The effect of the external point charge q_0' on the spheroid can be approximately equivalent to another monopole q_i. The mirror charge of q_i is $q_i'=-\beta q_0'$ which again acts as an external charge to polarize the spheroid. The charge q_i is balanced by a negative charge $-q_i$ distributed uniformly over the spheroid. The dipole oscillation p_i generated by the oscillation of q_i is $p_i = p_0\eta$, where $p_0 = 2q_0L$ and η is called "near-field factor" which is determined by the geometry of tips and tip-sample distance. The overall dipole moment p_{eff} is responsible for scattering:

$$p_{eff} = p_0 + p_i = 2q_0L(1+\eta) \tag{2.4}$$

Where $q_0 \propto (1 + cr_p)$ and the effective polarizability α_{eff} can be obtained:

$$\alpha_{eff} = \frac{p_{eff}}{E_0} \propto (1+\eta)(1+cr_p) \tag{2.5}$$

The scattering coefficient can be defined as:

$$\sigma = \frac{E_s}{E_0} \propto (1+\eta)(1+cr_p)^2 \tag{2.6}$$

Note that the term $(1 + cr_p)$ in α_{eff} considers the contribution directly from the tip and that reflected from the sample surface to the tip and then to the detectors. $(1 + cr_p)^2$ term in σ adds one more contribution from the near field signal from the tip that is reflected by the sample surface once before entering the detector.

2.2.3 Background Free Detection

The detected signal in real experiment, however, contains not only near field interaction but also background signal coming from the other parts of the AFM tip or directly from the sample's far field scattering and is usually much stronger than near field signal. The background scattering can cause serious artifacts in the final image. Suppose the tip length is L_{tip} ($L_{tip} \gg L$), the background dipole moment induced by incoming light should then be added to the expression for scattering coefficient:

$$\sigma_T = \sigma_B + \sigma_N \propto (1+cr_p)^2(\chi_{tip}+\eta) \tag{2.7}$$

where $\chi_{tip} = L_{tip}/2L$.

To suppress the background signal, the AFM tip is working at tapping mode (oscillating with frequency Ω and amplitude ΔH) as shown in Fig. 2.7. The incident and scattered light will have a phase shift when the tip apex is at different positions during oscillation. The background scattering coefficient σ_B can be modified to $\propto (e^{i\Delta\phi} + cr_p e^{-i\Delta\phi})^2 \chi_{tip}$ where $\Delta\phi = k_0 \Delta H cos\theta cos\Omega t = \Phi_0 cos\Omega t$ is the phase difference. The Fourier expansion of σ_B with respect to Ω can be written as:

$$\sigma_{B,0} \propto \left(1 + cr_p\right)^2 \chi_{tip} \tag{2.8}$$

$$\sigma_{B,n>0} \propto \frac{(i\Phi_0)^n}{n!} \left(1 + c^2 {r_p}^2 (-1)^n\right) \chi_{tip} \tag{2.9}$$

For near field scattering coefficient $\sigma_N \propto (1 + cr_p)^2 \eta$, since η is dependent on time *t*, the Fourier expansion will include η and can be expressed as:

$$\sigma_{N,n} \propto \left(1 + cr_p\right)^2 \eta_n \tag{2.10}$$

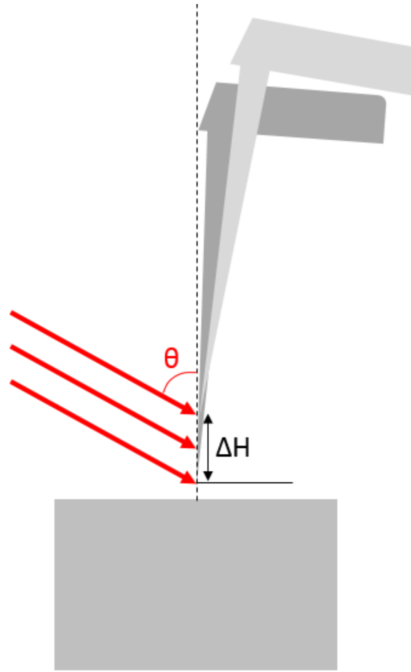

Figure 2.7: Scheme to suppress background signal. Tip is oscillating with frequency Ω and amplitude ΔH. The incident light makes an angle θ with the axis of the tip.

A quantitative estimation of the ratio of $\sigma_{B,n}$ to $\sigma_{N,n}$ shows ~100 for n=0, ~10 for n=1 and ~0.01 for n=2 [9]. It's clear that at higher harmonics (n≥2) σ_B is negligible compared to σ_N.

The scheme to suppress noise discussed above looks plausible but is not realizable in real measurement as least for continuous wave light sources. The reason is that the scattering coefficient σ_T is proportional to electric field of light which can't be directly measured. The output voltage produced by detectors is proportional to the light intensity which is related to the square of σ_T. As shown in Fig. 2.8 (a), the scattering electric field is the sum of background and near field part:

$$E_{total} = E_B + E_N = E_0 \sum_n e^{in\Omega t} (\sigma_{B,n} + \sigma_{N,n}) \tag{2.11}$$

and the output voltage V is expressed as:

$$V = \sum_n e^{in\Omega t} V_n = |E_{total}|^2 \tag{2.12}$$

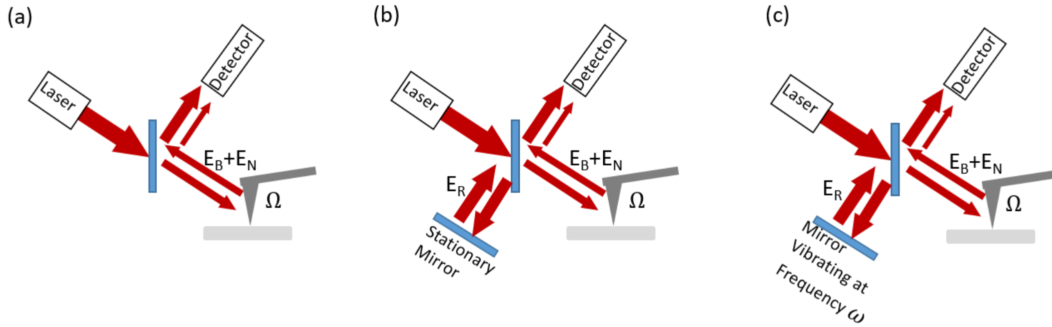

Figure 2.8: Non-interference(a), Homodyne(b) and Pseudo-Heterodyne for background free detection.

The simplification considering that the $\sigma_{B,0}$ is much larger than other terms of $\sigma_{B,n>0}$ and $\sigma_{N,n}$ leads to the expression of the nth harmonics of V:

$$V_n \propto \sigma_{B,0}\sigma_{B,n}{}^* + \sigma_{B,0}\sigma_{N,n}{}^* + \sigma_{N,n}\sigma_{B,0}{}^* + \sigma_{B,n}\sigma_{B,0}{}^* \tag{2.13}$$

Now if we write the complex number $\sigma_{N,n}$ as the combination of amplitude and phase $A_n e^{i\phi_n}$ and $\sigma_{B,n}$ as $b_n e^{i\psi_n}$, and neglect b_n at higher harmonics, V_n can be further simplified to:

$$V_n \propto b_0 A_n \cos(\phi_n - \psi_0) \tag{2.14}$$

The final expression contains the strong 0th order background term and both the amplitude and phase of the near field signal. The result is that any change of V_n during the s-SNOM measurement cannot be reliably attributed to the change of b_0, A_n, ϕ_n, ψ_0 or the combination of them.

To effectively suppress the 0th order background b_0, the homodyne scheme is applied as shown in Fig. 2.8 (b), in which a reference is added, and a large portion of the incident light is directed to the mirror by the beam split and reflected to the detector. A third term of electric field from the mirror $r_M e^{i\varphi_M}$ will be included in the calculation resulting in:

$$V_n \propto b_0 s_n \cos(\phi_n - \psi_0) + r_M A_n \cos(\phi_n - \varphi_M) \tag{2.15}$$

since $r_M \gg b_0$:

$$V_n \propto r_M A_n \cos(\phi_n - \varphi_M) \tag{2.16}$$

Now the phase of light from reference mirror φ_M can be changed by 90 degrees by shifting the mirror by λ/8, V_n becomes:

$$V_n{}' \propto r_M A_n \sin(\phi_n - \varphi_M) \tag{2.17}$$

here A_n and ϕ_n can be separated from the calculation using V_n and $V_n{}'$ and there is no background term.

The homodyne is valid only on the assumption that $r_M \gg b_0$. To completely get rid of b_0, a third method called "pseudo-heterodyne" is shown in Fig. 2.8 (c), in which the reference mirror is vibrating along the direction of light beam shining onto it. The vibration frequency ω is on the order of several hundred Hertz, much smaller than the tip vibrating frequency (hundreds of kilohertz). The result is that the phase of the reference beam is modulated:

$$E_R \propto \rho e^{i\Gamma\cos(\omega t)} \tag{2.18}$$

where Γ refers to the modulation amplitude and $\rho = r_M e^{i\varphi_M}$. The Fourier expansion of E_R is:

$$E_R = \sum_m \rho_m e^{im\omega t} \tag{2.19}$$

where $\rho_m = r_M J_m(\Gamma) e^{i\varphi_M + im\pi/2}$. J_m is mth order Bessel Function. Now the output voltage can be written as:

$$V = \sum_{m,n} e^{i(n\Omega+m\omega)t} V_{m,n} \propto |\sum_n e^{in\Omega t}\left(\sigma_{B,n} + \sigma_{N,n}\right) + \sum_m \rho_m e^{im\Omega t}|^2 \quad (2.20)$$

And

$$V_{m,n} \propto \left(\sigma_{B,n} + \sigma_{N,n}\right)\rho_m{}^* + \left(\sigma_{B,n} + \sigma_{N,n}\right)^* \rho_m \qquad m \neq 0, n \neq 0 \qquad (2.21)$$

In this case the 0th order background term $\sigma_{B,0}$ is completely removed and at higher harmonics n>1 only $\sigma_{N,n}$ and ρ_m are left:

$$V_{m,n} \propto r_M J_m(\Gamma) A_n \cos(\phi_n - \varphi_M - m\pi/2) \qquad (2.22)$$

Let $l = m + 1$ and

$$V_{l,n} \propto r_M J_l(\Gamma) A_n \cos\left(\phi_n - \varphi_M - \frac{l\pi}{2}\right) = r_M J_l(\Gamma) A_n \sin\left(\phi_n - \varphi_M - \frac{m\pi}{2}\right) \quad (2.23)$$

Now A_n and ϕ_n can be obtained using $V_{m,n}$ and $V_{l,n}$. In real experiments usually the first and second side band of the nth harmonic signal (n=2 or 3, m=1, l=2) are used.

Chapter 3

IR s-SNOM Experiments

3.1 IR s-SNOM on Ca_2RuO_4 single crystal

3.1.1 Introduction

The Mott insulator Ca_2RuO_4 is the subject of much recent attention following reports of emergent nonequilibrium steady states driven by applied electric fields or currents. We carry out infrared nano-imaging and optical microscopy measurements on bulk single crystal Ca_2RuO_4 under conditions of steady current flow to obtain insight into the current-driven insulator to metal transition. We observe macroscopic, non-filamentary growth of the current-induced metallic phase, with nucleation regions for metal and insulator phases determined by the polarity of the current flow. A remarkable metal-insulator-metal micro-stripe pattern is observed at the phase front separating metal and insulator phases. The micro-stripes have orientations tied uniquely to the crystallographic axes, implying strong coupling of the electronic transition to lattice degrees of freedom. Theoretical modeling further illustrates the importance of the current density and confirms a sub-micron-thick surface metallic layer at the phase front of the bulk metallic phase. Our measurement confirms that the electrically induced metallic phase is non-filamentary and is not driven by Joule heating, revealing remarkable new characteristics of electrically induced insulator-metal transitions occurring in functional correlated oxides.

Electric-control of nonthermal phase transitions in strongly correlated electron materials (SCEM) is a central theme of modern-day condensed matter research[13]–[21]. While many observations of current or field-driven transitions have been reported, interpretation in terms of true nonequilibrium phases is complicated by the possibilities of Joule heating (which could imply that the current simply heats the system into the higher temperature phase) and microscopic phase separation. This is especially true for SCEM, since the competition between many degrees of freedom including orbital, lattice and magnetic ordering can yield coexistence of multiple phases in the same crystal, triggered by minute perturbations of the electronic and lattice subsystems. Field-induced filament growth and temperature-induced phase percolation at microscopic scales have been extensively reported in 3d transition metal oxides, including vanadates, manganites, and cuprates[22]–[29]. Therefore, direct insight into the spatial structure and thermal aspects of quantum phase transitions is urgently needed.

At thermal equilibrium, Ca_2RuO_4 is a Mott insulator at room temperature and "bad metal" at high temperatures[30]. Both heating above T_c=357 K[31] and applying hydrostatic pressure above 0.5 GPa[32]–[34] can induce the insulator-to-metal transition (IMT). It was recently found that an astonishingly small electric field of 40 V/cm can also induce the IMT, with experimental evidence excluding the major role of Joule heating[35], [36]. Furthermore, X-Ray diffraction measurements revealed a possible intermediate electronic and lattice state preceding the full metallic phase, maintained by DC current[37]. These current induced states in Ca_2RuO_4 can persist to low temperatures, where strong diamagnetism was discovered at a current density of merely 10 A/cm^2 [14]. Therefore, a mounting body of evidence has suggested importance of current-induced non-equilibrium phenomena in Ca_2RuO_4. However, the microscopic spatial structure of the metallic phase and the transition itself have heretofore not been clarified.

3.1.2 Experiments

IR nano-spectroscopy and nano-imaging techniques based on s-SNOM is used here[38], [39]. The experiments are performed at room temperature and ambient pressure, under conditions of controlled constant current flow. The IR nano-spectroscopy covers a wide frequency range from 400 cm^{-1} to 2000 cm^{-1} (25-5 μm) capturing both the phonon and electronic optical response with 20 nm spatial resolution. In addition, CO_2 laser-based IR nano-imaging at ~900 cm^{-1} (~11 μm) with the same spatial resolution is used to investigate the current-induced insulator-metal phase boundary across different stages of the phase transition[39].

The Ca_2RuO_4 single crystals examined here have typical dimensions of ~1 mm × ~1 mm × ~200 μm (thickness). Current is introduced to the sample via needle-like electrodes with a width of ~40 μm deposited on opposite edges of the crystal, enabling two terminal *I-V* characteristics to be obtained simultaneously with acquisition of optical micrographs and s-SNOM imaging across IMT. The main panel of Fig. 3.1(a) presents the two-terminal *I-V* characteristic. Simultaneously acquired optical micrographs obtained under visible light illumination are shown as insets. As the current is increased from zero the sample remains insulating (low *I-V* ratio, region 1) up to a critical voltage of about 5V (electric field *E*~50V/cm for our sample dimension). The corresponding optical micrograph shows that the sample is insulating (visibly bright) at zero voltage. This phase is labeled as S phase to be consistent with the previously reported S-Pbca lattice structure of the insulating phase[40], [41]. At slightly above 5 V, the current discontinuously jumps to a higher value. At the same time, a visibly dark region

(identified as the metallic L-Pbca state and denoted here as L) nucleates from the negative electrode and expands with increasing current. The boundary of the L phase is seen to have a convex arc-like shape surrounding the effectively point-like electrode, suggesting the IMT occurs only where current density exceeds a critical value, thus determining the location of the insulator-metal boundary. As the current increases, the area of the metallic (dark) region increases. The *I-V* curve (curve 2) correspondingly displays a negative differential resistance which correlates with the optically identifies volume fraction of the metal. The sample is completely transformed at sufficiently high currents.

Remarkably, as demonstrated in Fig. 3.1(b) and (c), the L phase consistently emerges from the negative electrodes for all samples we have tested. Reversing the polarity of the applied voltage also reverses the electrode from which the L phase emerges. These observations strongly weaken the importance of Joule heating, which should be a scalar quantity independent of the direction of current. Besides, Peltier effect as the dominant driving mechanism can also be excluded. The Peltier effect in Ca_2RuO_4 leads to a temperature gradient across the two electrodes, which might in principle drive the interface towards the positive electrode via thermoelectric heating. This scenario implies that the nucleated L state has already reached T_c and the movement of the phase boundary is purely due to local heating of the sample. However, we find that further heating of the entire sample within 18-degree Kevin does not move the phase boundary. This observation counter-indicates a thermoelectric mechanism and supports the scenario of an intrinsic electric current-induced IMT in which bulk Joule or thermoelectric heating plays at most a minor role.

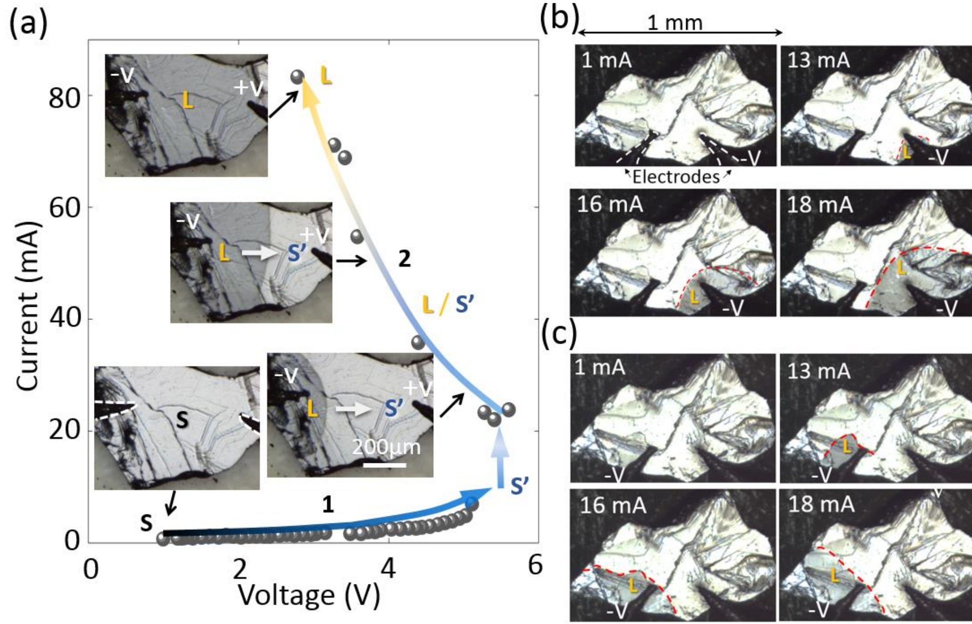

Figure 3.1: DC transport characterization and optical photographs of a Ca_2RuO_4 bulk single crystal at different stages of the IMT. (a) DC *I-V* curve with optical images taken by a CCD camera in the visible range. The insets show the emergence and expansion of the L phase (dark region) at each stage of the phase transition. The white dashed line in the bottom inset outlines the silver paint electrodes on the sample surface. (b) and (c) show the switching of L phase from the right to left electrode via reversing the polarity of the two electrodes (outlined by the white dashed lines).

The microscopic origin of the polarity dependent switching most likely arises from the strong electron-hole asymmetry of the many-body density of states of frontier (the t_{2g} symmetry Ru *d*) orbitals. At room temperature in equilibrium, the gap in insulating Ca_2RuO_4 is formed between an *xy*-orbital derived valence band and *xz/yz*-orbital derived upper-Hubbard bands. The resulting many body density-of-states is highly asymmetric about the Fermi level, with the filled bands exhibiting a large peak at the band edge and the empty states having a smoother spectral structure[42]. During the IMT, there is a considerable redistribution of electrons from doubly occupied *xy* (and singly occupied *xz/yz*) orbitals in the insulating phase to approximately equal occupancy of each orbital in the metallic phase[43]–[45]. Therefore, under small changes in electrochemical potential, the strong electron-hole asymmetry yields much more pronounced hole doping compared with electron doping in the metallic L phase. This vast asymmetry in the electrostatic susceptibility of Ca_2RuO_4 may explain the initial nucleation of L phase

at negative electrodes and may imply a current dependent force across a domain wall.

The broadband nano-IR spectra at different current-controlled stages of the IMT with ~20 nm spatial resolution is shown in Fig. 3.2 (a). At 0 V, the nano-IR spectrum reveals a peak at ~603 cm^{-1} with an apparent dip at about 680 cm^{-1} (grey curve, S state). This peak is identified as the previously reported transverse optical in-plane Ru-O stretching mode of Ca_2RuO_4[46]–[48]. The amplitude of this phonon response is continuously suppressed with increasing electric current and its peak position is weakly blue-shifted (~8 cm^{-1}), which we take as signifiers of an intermediate state we label as the S' state. As shown in Fig. 3.3, IR spectra are collected with nanometer spatial resolution at a fixed point on the sample surface near the negative electrode. With the increasing electric current (but still below the current value at which the L-Pbca phase begins to appear), the phonon peak gradually decreases in amplitude and slightly blue shifts in frequency. At the same time, the sample resistance gradually decreases but the IR near-field response at 700-900 cm^{-1} range does not change with current. This is in agreement with other experimental observations of an intermediate S state that is induced by current[37]. Thus, we label this current-suppressed state as the S' state. It is a precursor to the structural phase transition to the L state. Note that the lack of significant change in higher frequency (700-900 cm^{-1}) response strongly suggests that the S' phase is not simply an inhomogeneous mixture of S and L phases, because in the inhomogeneous mixture scenario the higher response of the L phase would lead to changes in the higher frequency response.

The nano-IR spectrum collected in the L phase (golden curve) shows a totally different behavior: the infrared signal presents a ~4-fold increase over the entire spectrum range without the phonon peak at 603 cm^{-1}. This behavior, in combination with the visible brightness reduction in the metallic L phase, suggests that the L (metallic) phase is characterized by a large spectral weight transfer from higher energies (visible light frequencies) to lower energies (IR and DC) which is consistent with the onset of a Drude response. While the electromagnetic response of inhomogeneous mixtures is complicated, the absolute normalization and spatial resolution of our nano-IR spectroscopy shows that the IR signal of S' state above 700 cm^{-1} is comparable to S but much lower than L, ruling out the possibility that S' state comprises any mixture of L and S phases. Here S' is attributed to a non-equilibrium intermediate state emerging under electric current flow, distinct from S and L phases, in agreement with other experimental observations in Ca_2RuO_4 under similar steady-state current conditions[35], [37].

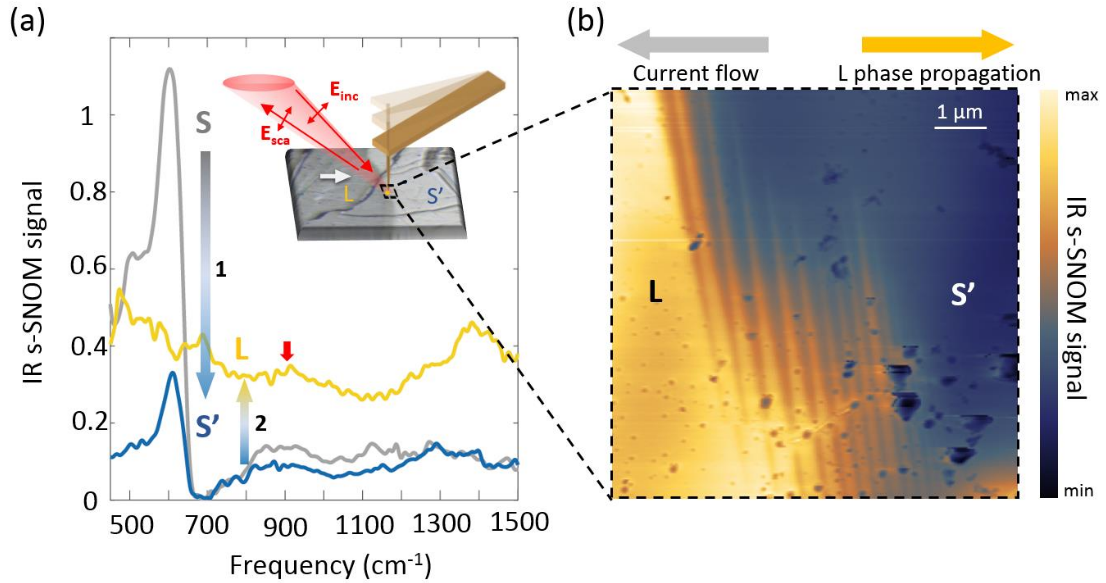

Figure 3.2: (a) IR nano spectra of S, S' and L states. Spectrum of S (grey) is taken without current, while spectra of S' (blue) and L (golden) are taken at two different regions several microns apart across the L-S′ phase boundary under the same current. The spectra are normalized to that of a thick gold film. Inset, schematic of the nano-spectroscopy setup and the optical photo of the L-S′ PB. (b) IR s-SNOM imaging of the L-S' boundary stripes at the phase boundary at frequency of 900 cm^{-1} marked by a red arrow in (a).

Fig. 3.2(b) shows IR nano-imaging of the L-S' phase boundary (PB) which is observed at intermediate currents. The probe laser at ~900 cm^{-1} (11 μm wavelength, or ~110 meV) is chosen to avoid energetic overlap with the transverse optical phonon response and to probe the genuine Drude response of the charge carriers in metallic Ca_2RuO_4. Higher IR response (more metallic) is rendered golden in false color, whereas dark blue represents a lower IR response characteristic of insulating regions. A striking pattern of alternating bright and dark stripes (lines of metallic and insulating behavior) is found to spontaneously develop within a few microns of the PB. The number and periodicity of these stripes vary in different regions. In some regions, no stripes at all are visible with only a simple step-like change in optical response.

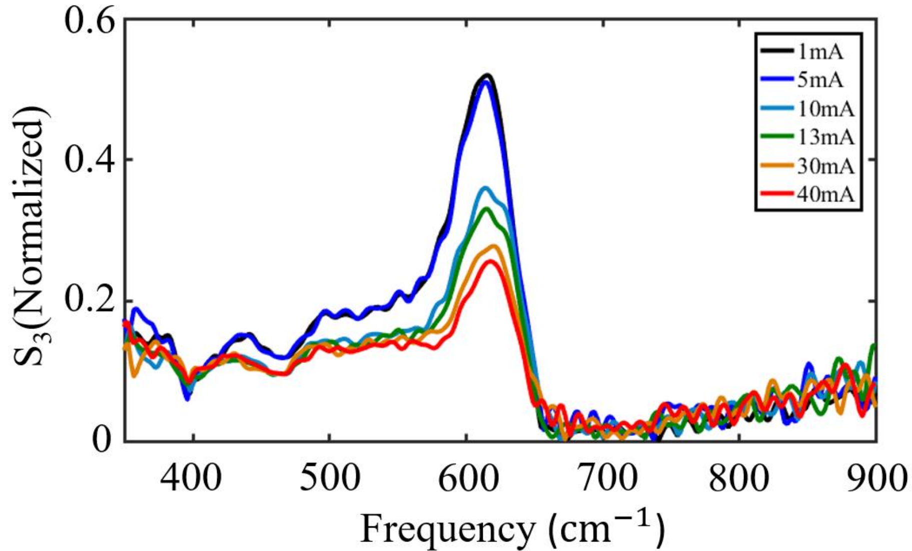

Figure 3.3: Current dependent near-field phonon response at currents lower than those needed to initiate the IMT, showing gradual suppression and slight blue shift of Ca_2RuO_4 phonon peak with the increase of electric current. All spectra are taken at the same spot on the sample surface; for all of the currents studied the optically dark L phase is not observed.

3.1.3 Analysis of Insulator-Metal Phase Boundary

We argue that the stripes arise from the difference in stress exerted by the electrons on the lattice in the two phases. While the insulating and metallic phases of Ca_2RuO_4 share the same Pbca symmetry, their lattice parameters are distinct. This leads to an elastic mismatch stress at insulator-metal phase boundaries. We focus here on the large in-plane orthorhombic anisotropy developed across the Ca_2RuO_4 structural transition[33], [35], [49]. The difference in the 'a_o' lattice parameter between the metallic L-Pbca phase and the S' state phase is within 0.03 Å, whereas difference in the 'b_o' lattice parameters is ~0.15Å[50], developing a spontaneous strain of approximately 3%. We argue that the elastic energy cost of the b_o-axis misfit stress can be mitigated by a striped alternation of L and S′ structural phases parallel to the a_o-axis.

A minimal theoretical model of the experiments includes the following ingredients:

- an electronic energy function that describes the metal-insulator transition at fixed strain and depends on an electronic order parameter ϕ and the applied current. We express the spatially resolved free energy density associated with a first-order structure transition involving two locally stable phases: a metallic phase (order parameter $\phi = \phi_M$) and an insulating phase (order parameter $\phi = \phi_I$).
- a coupling of the order parameter to the strain tensor ε**.**
- an elastic theory describing the energy cost of a given strain pattern.

These considerations lead to a function given by

$$F = F_{\text{electronic}} + F_{\text{elastic}} \quad (3.1)$$

with

$$F_{\text{elastic}} = \int d^3r \left[-\sum_{ij}\sigma_{ij}^{*}\varepsilon_{ji}\left(\vec{r}\right)\left(\phi\left(\vec{r}\right) - \phi_I\right) + \frac{1}{2}\sum_{ijkl}\varepsilon_{ij}(\vec{r})K^{ij;kl}\varepsilon_{kl}(\vec{r})\right]$$

and

$$F_{\text{electronic}} = \int d^3r(f_{\text{electronic}}(\phi) + f_{\text{current}})$$

$\varepsilon_{ij} = \frac{1}{2}(\partial_i u_j + \partial_j u_i)$ is the usual strain tensor given in terms of the components u_j of the displacement vector. The elastic response is specified by the force tensor $K^{ij;kl}$ of linear elasticity theory. The order-parameter/strain coupling arises physically because the metal and insulating states have different orbital occupancy[51] and is given in terms of the stress σ^* caused by a deviation of the order parameter from its reference state (here chosen to be the room temperature insulating phase). In the insulating phase near the transition the in-plane orthorhombic lattice parameters a_o and b_o are nearly equal, but in the metallic phase b_o is longer by 2%, implying that the metal-insulator transition induces a stress, which we model as a misfit stress $\sigma_{xx}^{*}(r) = \sigma^{*}(\phi_M(r) - \phi_I)$ within the crystal, with the direction of stress (x) aligned to the b_o-axis. The strain fields induced by this spontaneous stress extend throughout the crystal and are computed using the isotropic solid approximation of linear elasticity.

We write $f_{\text{electronic}}$ as

$$f_{\text{electronic}} = \frac{d}{2}W(\nabla\phi)^2 + df(\phi) \quad (3.2)$$

where the first term gives the domain wall energy density as defined by f_{DW} in the main text; $f(\phi)$ describes a strong first order energy landscape with deep minima at $\phi = \phi_{I,M}$ in the insulating and metallic states respectively.

The driving term $f_{\text{current}} = f_M - f_I$, a difference in the energy density of the metallic and insulating phases, that increases linearly with in-plane position ($\vec{r}$) along the direction ($\hat{n}$) of current flow. This term is due physically to the spatial variation of the current density. We write $f_{\text{current}} = A\hat{n} \cdot (\vec{r} - \vec{r}_0)\phi(\vec{r})$

We minimize the free energy with respect to ε by solving

$$K^{ij;kl} \frac{\partial^2 u_k}{\partial x_j \partial x_l} = \sigma^*_{ij} \frac{\partial \phi}{\partial x_j} \tag{3.3}$$

for $u(r)$. From u we compute ε as a functional of $\phi(r)$. Substitution into the free energy then gives a function of $\phi(r)$ which we proceed to minimize energy function using a finite element gradient descent method to determine the equilibrium configuration of the order parameter. As we find, in many circumstances a spatially textured function $\phi(r)$ minimizes the energy.
In our calculations we make the following simplifications:

1. We assume that in the vicinity of the phase front the material may be considered to be insulating almost everywhere, except that a metallic phase may occur within a thin skin at the top surface. The depth d of the metallic region is assumed to be much less than sample depth D and we take $\varphi(x,y,z)$ to be independent of z in this region. This assumption is motivated by the reasoning that expansion of the c-axis lattice constant upon the insulator-metal transition is most naturally accommodated at the free outer surface of the crystal; as a consequence, we might expect the formation of metallic regions first at the top surface of the crystal.

2. We model the elastic properties in the isotropic solid approximation
$$K^{ij;kl} = \lambda\delta_{ij}\delta_{kl} + \mu(\delta_{ik}\delta_{jl} + \delta_{il}\delta_{jk}) \tag{3.4}$$
This simplifies the algebra but does not change any essential features.

3. Based on the observation that the in-plane lattice mismatch between metal and insulator is large only for one direction (crystallographic b, which we define to be x) we assume that the only important component of the strain tensor is σ_{xx}

Representative results are shown in Fig. 3.4(d) – (f). We found that stripes can afford the minimal energy configuration of coexistent metal and insulator phases at the PB. This particularly depends on the magnitude of the current density

gradient, the relative values of the domain wall and elastic energies, and the orientation of the phase boundary with respect to the crystallographic axes. It's found that stripes are most easily produced when the PB normal coincides with the direction of spontaneous stress – that is when the direction of current is aligned to the in-plane b_o (x) axis. Once formed, these stripes align perpendicular to the direction of greatest elastic mismatch. The spatial extent of the striped region is set by the gradient of the current density change (denoted as B) across the PB from L to S' state, whereas the width of the stripes is set by the interplay of domain wall and elastic energies. When B is large enough, no stripes form (compare Fig. 3.4(d) with (f)). The relative widths of the insulating (or metallic) stripes shrink gradually towards the homogeneous phases (Fig. 3.4(e)), which coincides with our experimental observations (Fig. 3.4(b)). The stripe periodicity is set by a combination of elastic energy, the gradient of the current density change, and thickness d of the metallic layer.

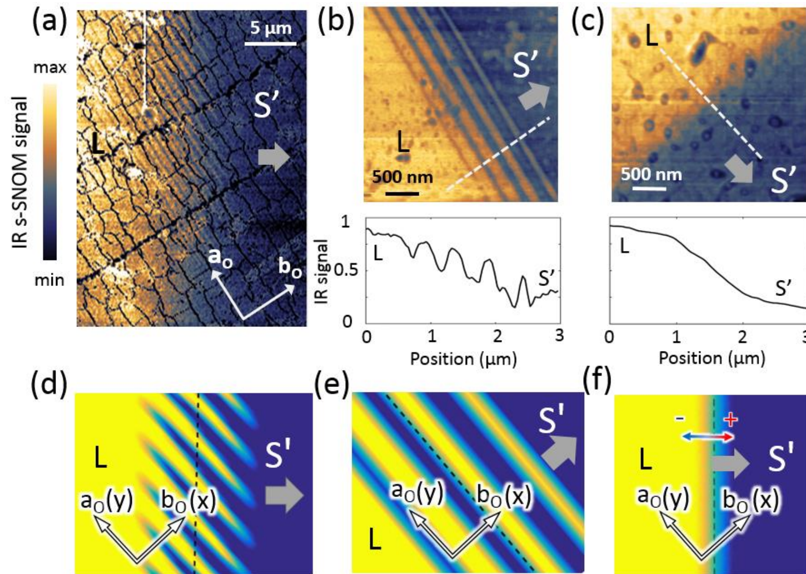

Figure 3.4: Oriented stripe formation across the PB. (a), (b), & (c) IR s-SNOM imaging (2nd harmonic) of S′-L phase boundaries on three different Ca_2RuO_4 samples. Lower panels of (b) and (c): line cuts of the s-SNOM signal along the dashed lines in the upper panels. (d), (e) Results of numerical minimization of the free energy for PB oriented at 45° and 90° to the crystalline b_o direction[39]. Yellow indicates metal and blue insulator. Panel (f) shares the same parameter as (d) except using a larger driving force gradient B. The grey arrows in (a)-(f) indicate the direction of the L state expansion (normal of the PB) under increasing current.

We next present results for the sample topography from atomic force microscopy, conducted concurrently with our IR nano-imaging. In Fig. 3.5(a), the s-SNOM image overlaid with corresponding topography, demonstrating a gradual rise of the IR response (black curves) toward the higher end of the metallic side. Since the probing depth of s-SNOM is typically less than 50 nm[52], [53], this gradual increase of the IR response suggests a growing depth of the metallic layer from S’ state to L phase across the PB, as schematically shown in Fig. 3.5(c). In addition, Fig. 3.5(b) reveals that topography over the metallic stripes is ~1 nm higher than the insulating phase, which can be understood through the fact that the S′ to L transition is accompanied by an out-of-plane lattice expansion by as much as 2% (c_L/c_s=1.023). Therefore, the surface metallic layer near the vicinity of the PB is estimated to be no more than a few hundred nanometers in depth. This is much smaller than the full thickness of the crystal, which is hundreds of microns.

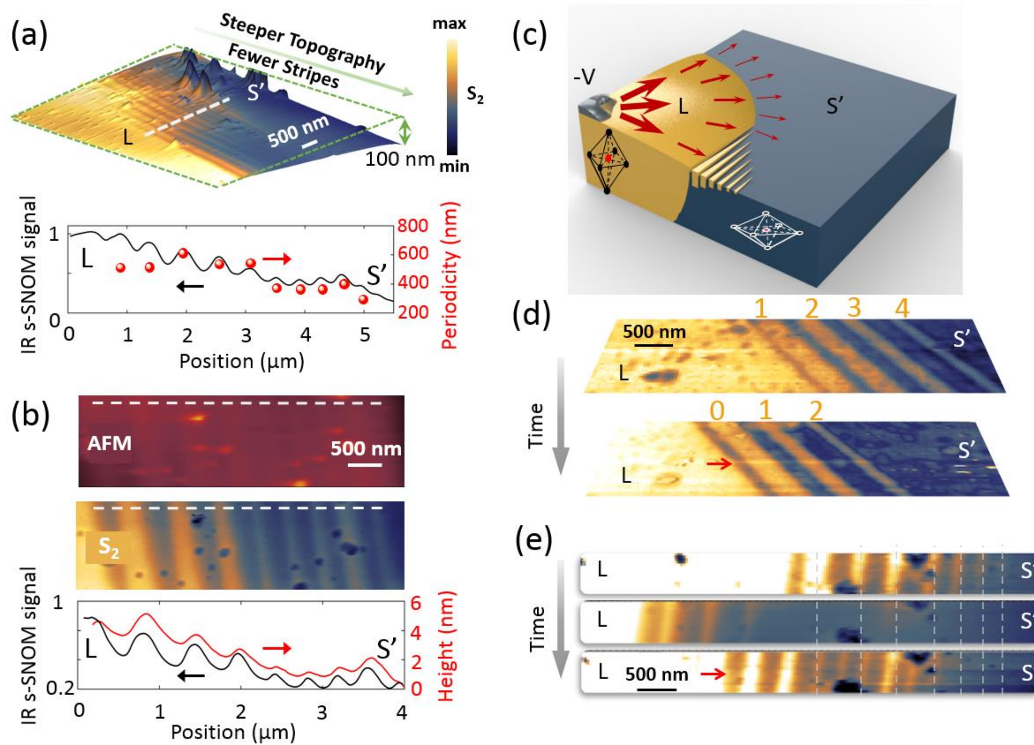

Figure 3.5: Topography and progression/regression of the PB. (a) Top: the sample topography overlaid with the s-SNOM image. For larger height change from L to S' state, fewer stripes are observed. (b) AFM topography (top) and IR s-SNOM signal S_2 imaging (middle) of 8 stripes across the PB. The bottom figure shows that the variations in topography (red curve) has a one-to-one correspondence to the IR signal (black curve). (c) Schematic of striped surface metallic layer at the PB, L phase bulges due to larger out-of-plane lattice constant, red arrows represent the magnitude and direction of negative charge flow density (d), (e) Progression or regression of the PB taken with repeated IR s-SNOM imaging on three different samples under current fluctuation around 12 mA. (d) The occurrence of new metallic and insulating stripes with a width on the order of ~100 - 200 nm during the retraction of the phase front. (e) The fluctuation of the phase front. The current fluctuation and the time elapsed between the consecutive images taken in all the subfigures are less than 0.1 mA and 20 min.

Fig. 3.5(d) shows retraction of the L phase when the current is decreased by ~0.1 mA from around ~12.0 mA. Top and bottom panels show the same sample region imaged by consecutive scans. Rather than a translational shift of pre-existing stripe patterns, we observe that previous metallic stripes disappear (e.g. "3" and "4") or become narrower at their same fixed locations (e.g. "1" and "2"), whereas

a new stripe ("0") nucleates at locations prescribed by the stripe periodicity. In Fig. 3.4(e), multiple stripes are shown to emerge or vanish relative to the existing stripes. Such self-organized spontaneous phase separation mediated by long-range strain interactions remains an underexplored phenomenon in the context of the IMT in single crystals, motivating future study by nano-imaging probes with time-resolved capabilities.

3.1.4 Conclusions

In conclusion, we have used a combination of visible-frequency microscopy and infrared nano-imaging to resolve the spatial structure and dynamics of the current-driven nonequilibrium IMT in Ca_2RuO_4 single crystals. The phase transition is initiated by a polarity-asymmetric nucleation of the current-induced bulk metallic phase at the negative electrode, consistent with strong electrostatic susceptibility due to electron-hole asymmetric electronic structure of the insulating S phase. The phase nucleation proceeds by expansion of the metal phase across the sample as current density is increased. A spontaneous surface stripe texture of coexisting metal and insulating phases is observed at the global metal-insulator phase boundary. We argue that this stripe formation is driven by minimization of elastic mismatch strain and is well described by a minimal theory considering a thin surface metallic layer. Our results support an electrically-induced insulator-metal transition scenario which is fundamentally distinct from the filamentary metallization common to high-field resistive switching reported in other oxides[54], [55]. Future studies will include low temperature experiments of Ca_2RuO_4 single crystals and epitaxial thin films driven through the electrically-induced IMT. Nano-imaging experiments under *in situ* applied strain would provide valuable insight to orbital ordering under static strain[56] to further clarify the microscopic mechanism of current-induced metallization in this compound.

(Section 3.1 is based on paper no. 1 in the publication list above.)

3.2 IR s-SNOM on VO_2 film

3.2.1 Introduction

Domain nucleation and growth is one of the hallmarks of a first-order phase transition. An example comes from the study of vapor bubbles in liquid, where heat or pressure determines the nucleation threshold [57]. In solids, such phenomena can

frequently be observed in an electronic or structural phase transition, where small "droplets" of new or intermediate phases emerge at the nanoscale [23], [58]. Conventional optical spectroscopies such as ellipsometry are successful in determining the complex optical constants of homogeneous electronic phases[59].However, due to diffraction limit, they fall short in characterizing structured inhomogeneous states that are small on the scale of the light wavelength.

By gathering the scattered light from s-SNOM we can effectively detects near-field interactions between the nanometer-sized tip apex and the sample surface, providing a spatial resolution far beyond the diffraction limit of traditional optics [60], [61]. However, due to the non-trivial nature of tip-sample interactions, accurate extraction of ε_1 and ε_2 from the measured "near-field signal" (real/imaginary parts or, equivalently, its amplitude/phase) is not straightforward, as has already been discussed in numerous pioneering works in the field [62]–[73]. To further previous efforts, here we apply a comprehensive approach to analyze near-field optical images of solid-state systems, especially in materials that display optical characteristic of "bad" metals (with negative real part and positive imaginary part of dielectric constant but their absolute values are much smaller than noble metals) in the infrared (IR) frequency range.

s-SNOM is ideal for quantitatively studying phase transitions in Mott insulators, bad metals, and other strongly correlated electron systems (SCES), for two primary reasons. First, unlike noble metals and 2D polaritonic semiconductors, which might possess geometry or dispersion-induced nonlocal responses, the carrier mobilities in SCES are exceedingly low. The optical response at IR frequencies can therefore be ascribed chiefly to effective quasiparticle behavior with large electron mass and high scattering rate of charge carriers [59], [74]. As a result, across insulator-metal phase transitions (IMT), the absolute value of ε_1 and ε_2 at IR frequencies remains smaller than in the noble metals (e.g. Au) while ε_2 can be larger than that of nominal semiconductors (e.g. Si) [59], [75]. Although the physics behind the dynamic evolution of optical permittivity in SCEM often involve a wide range of complex phenomena, the unique range of optical reflectivity expressed by ε_1 and ε_2 promises a relatively straightforward opportunity to extract them from near-field imaging experiments. As we will describe in detail below, quantitative analysis of the spatially resolved near-field signal recorded from SCES can be much easier compared to other solid-state materials such as plasmonic media, doped semiconductors, or noble metals. Second, through spatially-dependent spectral mapping, the high spatial resolution afforded by s-SNOM measurements allows for direct observation of intrinsic material properties even among nano-structured phases. At the same time, the large spatial scan range (up to $100\ \mu m \times 100\ \mu m$) conventionally accessible to s-SNOM

affords study of mesoscopic textures that are induced by long-range interactions such as strain or magnetic fields, which are important for systematic investigations of the evolution of competing phases at multiple relevant length-scales across a solid-solid phase transition [61], [76]–[82].

3.2.2 Methodology for Nanoscale Permittivity Extraction

To extract the nanoscale dielectric constants from nano-imaging experiments, a reliable roadmap is established to link the optical properties of the sample to the near-field signal. It's insightful to plot ε_1- and ε_2-dependent values predicted for $Re(S_n)$ and $Im(S_n)$ and to use these as a guide for interpretation of optical contrasts in the measured near-field signal.

As has been introduced in Chapter 2, the near-field signal in a dipole model can be regarded as proportional to the effective polarizability α_{eff} of a point dipole above the sample surface:

$$\alpha_{eff} = \frac{\alpha}{1 - \frac{\alpha\beta}{16\pi(a+d)^3}} \tag{3.5}$$

where $\alpha = 4\pi a^3 \frac{\epsilon_{tip}-1}{\epsilon_{tip}+2}$, $\beta = \frac{\varepsilon-1}{\varepsilon+1}$. Here a is the radius of the dipole sphere, d is the distance between the center of the sphere and the sample surface, and ϵ_{tip} is the dielectric function of the probe tip (usually a good metal at the selected probing frequency) [62], [63]. $\varepsilon = \varepsilon_1 + i\varepsilon_2$ is the local dielectric constant of sample under tip apex. The real and imaginary part of the predicted near-field signal (in this case S_3) versus ε_1 and ε_2 can therefore be plotted analytically, as shown in Fig. 3.6.

The second and third treatments go far beyond the point dipole approximation and address the realistic geometry of the probe-sample interaction, which includes the angle of incidence of illuminating radiation, the geometric effect of the AFM probe (e.g. length and angle of the tip shank) as well as physical oscillation of the tip that enables lock-in detection of the experimental signal. Predictions of the second method are shown in Fig. 3.6(b), where S_3 is mapped following Eq. 45 in reference [83], an approximation which reduces the calculation down to an effective algebraic form using the *lightning rod model* [83], [84]. As is clearly demonstrated, S_3 predicted in Fig. 3.6(b) is considerably different from α_{eff} in Fig. 3.6(a), especially within the relevant regime of $-10 < \varepsilon_1 < 0$ and $0 < \varepsilon_2 < 10$. In addition, Fig. 3.6(b) shows a highly resonant region slightly below $\varepsilon_1 = -1$ at small values of ε_2 – a regime which hosts localized "polariton modes" (encircled by the white dotted curves) whose excitation is predicted to reside within

the tip-sample gap. These modes appear where the Fresnel reflection coefficient R_p for p-polarized near-fields emitted from the tip is relatively large in amplitude [71], [72]. Fig. 3.6(c) presents a third model in which the essentially conical metal shell of the near-field probe is mapped into a flat disk by the method of conformal mapping, where the electric fields and currents are efficiently represented through basis functions with built-in singularities [85]. This method accurately represents the strong quasi-electrostatic fields anticipated at the sharp asperities of a realistic tip geometry.

Both the lightning-rod (Fig. 3.6(b)) and conformal mapping (Fig. 3.6(c)) models calculate the charge distribution on the surface of a realistic near-field probe geometry, and consequently the back-scattered light field, in a quasi-electrostatic approximation. Mathematical presentation of these two methods are discussed in previous publications [84], [85]. Due to the nature of the tip-sample interaction, different models yield distinct quantitative results. However, outside of the regime of strong tip-sample polariton-like resonances, all three models yield qualitatively similar trends. This is especially the case for the latter two models, which are quantitatively comparable within non-resonant regimes (far from the regime of "localized polaritons"). The charts in Fig. 3.6 therefore provide a roadmap for back-extracting spatially resolved values of ε_1 and ε_2 and serve the basis for our forthcoming analysis.

SCES usually possess very high carrier scattering rates, and therefore large ε_2 at infrared energies. As a result, the temperature-dependent "trajectory" of near-field signals on the conceptual phase space of ε of a SCES material during its IMT will typically "avoid" the highly resonant region. Two representative cases are demonstrated in Fig. 3.6(b), where the temperature-dependent traces of ε_1 and ε_2 deduced from prior spectroscopies of VO_2 and V_2O_3 thin films during the IMT are plotted as dashed grey and yellow lines, respectively[75], [76], [86]. Note these optical permittivities at ~925 cm^{-1} associate with the results of area-averaging far-field IR ellipsometry studies as shown in Table. 3.1 and 3.2. This frequency range is well separated from the optical response of low energy phonon modes in the representative material.

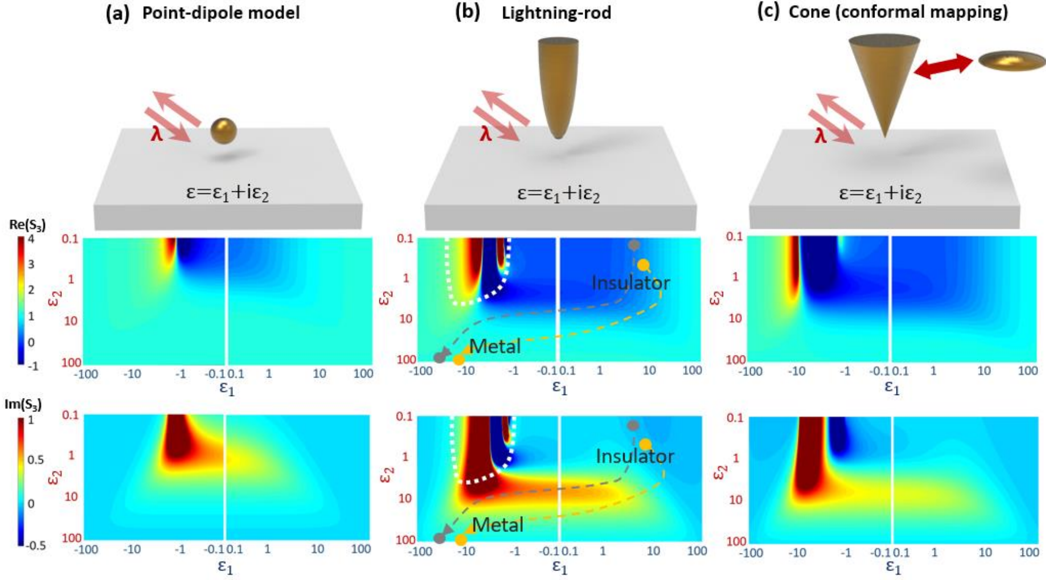

Figure 3.6: The quantitative relationship between predicted near-field signal S_3 and optical permittivity $\varepsilon = \varepsilon_1 + i\varepsilon_2$ calculated using three different theoretical models. (a) Real and imaginary parts of α_{eff}, calculated from the point-dipole model, assuming $S_3 \propto \alpha_{eff}$. (b) Real and imaginary parts of S_3 calculated with the lightning rod model using an IR probing wavelength of 11 μm. The ε regime encircled by the white dotted line corresponds to the strongly resonant regime where the point dipole approximation is expected to fail. Gray dashed arrows indicate the temperature induced evolution of ε during IMT in a SCEM, here corresponding to VO_2 from T = 295 K (top right) to 345 K (bottom left). The yellow dashed curve similarly associates with the IMT in a measured V_2O_3 thin film. (c) Real and imaginary parts of S_3 calculated by the conformal mapping method applied to a sharp metallic cone, with predictions comparable to those of the lighting rod model.

Temp	ε_1	ε_2
295 K	4.77	0.07
340 K	3.02	1.34
341 K	1.47	2.41
342 K	0.44	3.03
344 K	-3.79	40.86
345 K	-23.32	90.88

Table 3.1: Dielectric constant of VO_2 film on sapphire substrate measured by ellipsometry at ~1000 cm^{-1}.

Temp	ε_1	ε_2
120 K	8.63	0.29
140 K	9.57	2.21
150 K	10.505	3.11
160 K	9.27	9.23
180 K	-18.09	82.64
200 K	-36.74	129.03

Table 3.2: Dielectric constant of V_2O_3 film on sapphire substrate measured by ellipsometry at ~1000 cm^{-1}.

3.2.3 Nanoscale Permittivity Extraction from Infrared s-SNOM Imaging of VO_2

Fig. 3.7 studies spatially resolved electronic states of a representative SCES, vanadium dioxide, demonstrating new physical information revealed by a detailed infrared near-field analysis combined with x-ray diffraction (XRD) measurements. Fig. 3.7 displays images of the real and imaginary parts of S_3 recorded from a 50 nm thick VO_2 film grown on $[110]_{Rutile}$ TiO_2 substrate during the IMT at elevated temperatures near T_{MI} = 340 K. The bright yellow stripes seen in Fig. 3.7(a) reveal the emergence of striped metallic domains whose geometry results from epitaxial strain present in the samples at elevated temperature, as described previously[58], [61], [87], [88]. In contrast to the real part of S_3, at these temperatures the imaginary part shows notably high contrast against the surrounding insulating material especially at opposing ends of these metallic stripes, whereas the center of these stripes presents a weaker contrast in $Im(S_3)$ as they elongate with increasing temperature (Fig. 3.7(b)). At a later stage of the transition, as the metallic stripes elongate and reach a percolation threshold across the film, $Im(S_3)$ reveals contrast instead across the transverse direction of the stripes whereas the "hot spots" at the two ends gradually weaken. This evolving contrast in the imaginary part of the near-

field optical signal has not been systematically investigated in previous nano-imaging studies of SCEM and leads to a novel finding after our extraction of the spatially resolved optical permittivity. As will be discussed below, these “hot spots” in $Im(S_3)$ are the result of a unique electronic state well correlated with the spatially inhomogeneous nano-scopic strain environment inferred in such thin VO_2 films.

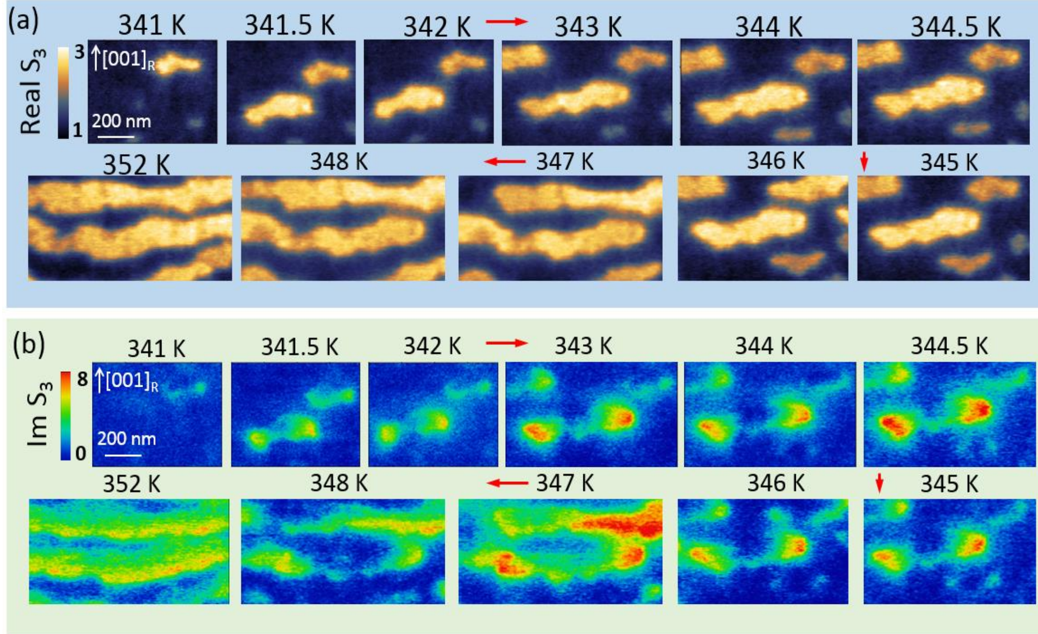

Figure 3.7: Temperature dependent evolution of metallic stripes in VO_2/[110]$_R$ TiO_2 thin films, measured by s-SNOM. a) The real part $Re(S_3)$ and b) imaginary part $Im(S_3)$ of the near-field signal resolved at the same location of the film at sequential temperatures from T=341 K to 352 K at ω~1000 cm^{-1}.

The position dependent optical permittivity of a typical metallic stripe resolved in the experimental data of $Re(S_3)$ and $Im(S_3)$ at 342 K is shown in Fig. 3.8. Maps of extracted ε_1 and ε_2 following from each of the three models discussed above are presented in Fig. 3(c) and (d), respectively. From the maps, we can see that the two ends of metallic stripes present a value of $\varepsilon_1$close to 0 and a value of ε_2 exceeding 10, corresponding physically to a highly damped surface plasmon mode. This novel “epsilon near zero” (ENZ) electronic state is intimately linked with spatially coincident “hot spots” emerging within microscopic strain environment of the film.

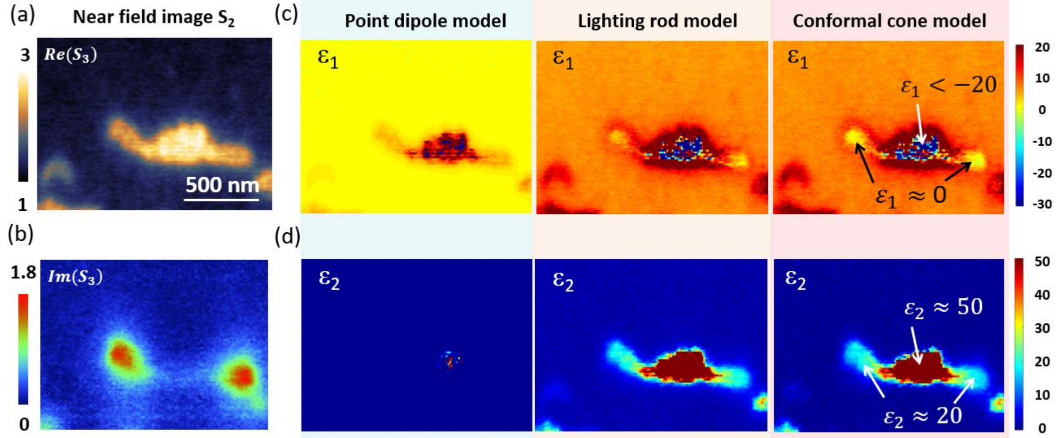

Figure 3.8: Self-consistent extraction of spatially resolved optical permittivities $\varepsilon = \varepsilon_1 + i\varepsilon_2$ throughout a metallic domain in the IMT of VO_2. Near-field images of a) $Re(S_3)$ and b) $Im(S_3)$ acquired by infrared nano-imaging at 342 K and ω~1000 cm^{-1}, enabling extraction of the c) real part ε_1 and d) imaginary part ε_2 of the optical permittivity according to predictions by the point dipole model, lighting rod model, and conformal mapping model.

The lattice structure of the film especially at these ENZ regions can be inferred from reciprocal space maps (RSMs) of the film crystallography resolved by synchrotron X-ray diffraction at different stages of the thermal IMT, contextualized by numerical simulations of the spatially inhomogeneous lattice strain emerging across the phase transition. As demonstrated by the RSM shown in Fig. 3.9(a), there are at least three crystallographic peaks along the ***k*** axis, corresponding to a variation of lattice constants along the $[001]_R$ direction lying within the plane of the film (c-axis of the rutile phase) during the phase transition (346 K), confirming the coexistence of both compressive and tensile strain. As expected, when the sample enters the fully insulating (metallic) state at T=300 K (364 K), only the monoclinic (rutile) peak remains. These temperature-resolved RSMs reveal that 1)a distinct structural phase with lattice parameter values different from conventional monoclinic and rutile phases (i.e. strain states) emerges and simultaneously coexist with monoclinic and rutile phases in the film during MIT, and 2) that the diffraction-intensity-weighted average of in-plane lattice constants associated with monoclinic and rutile phases exhibit a temperature-dependent "mode repulsion" effect across the IMT, in which the two structural phases experience opposing relative accommodation strains (Fig. 3.9(b)).

We develop a Landau theory of strain-coupled first-order phase transitions that reproduces the thermal "mode repulsion" of c-axis lattice constants resolved in our X-ray diffraction experiments and associated with rutile and monoclinic regions

of VO_2. By taking account of the energetic competition between inter-phase domain walls and accommodation strains of the dissimilar insulator and metal structural states, numerical simulations of the IMT according to this Landau theory successfully predict the stripe-like spatial evolution of insulator and metal domains as depicted in Fig. 3.9(d).

These results imply that ENZ regions identified by our nano-scale extraction of optical permittivity in fact correspond with metallic regions of exceptionally compressive c-axis strain. Uniaxial c-axis strains in excess of 1% have been theoretically associated with a modulated electronic state within the metallic phase of VO_2, as predicted by Kotliar et al [89]. Moreover, the Landau theory follows from linear elasticity theory assuming a temperature-independent VO_2 elastic modulus. On the other hand, super-elastic anomalies have been identified in the rutile metallic phase proximate to the IMT, with potential to enhance the strain susceptibility of metallic "hot spots" to the inhomogeneous accommodation stress predicted by our simulations. Thus, our theory may provide even an underestimate for strain levels at ENZ hot spots in VO_2, affording further rationale for an unforeseen electronic state induced by spontaneous strain.

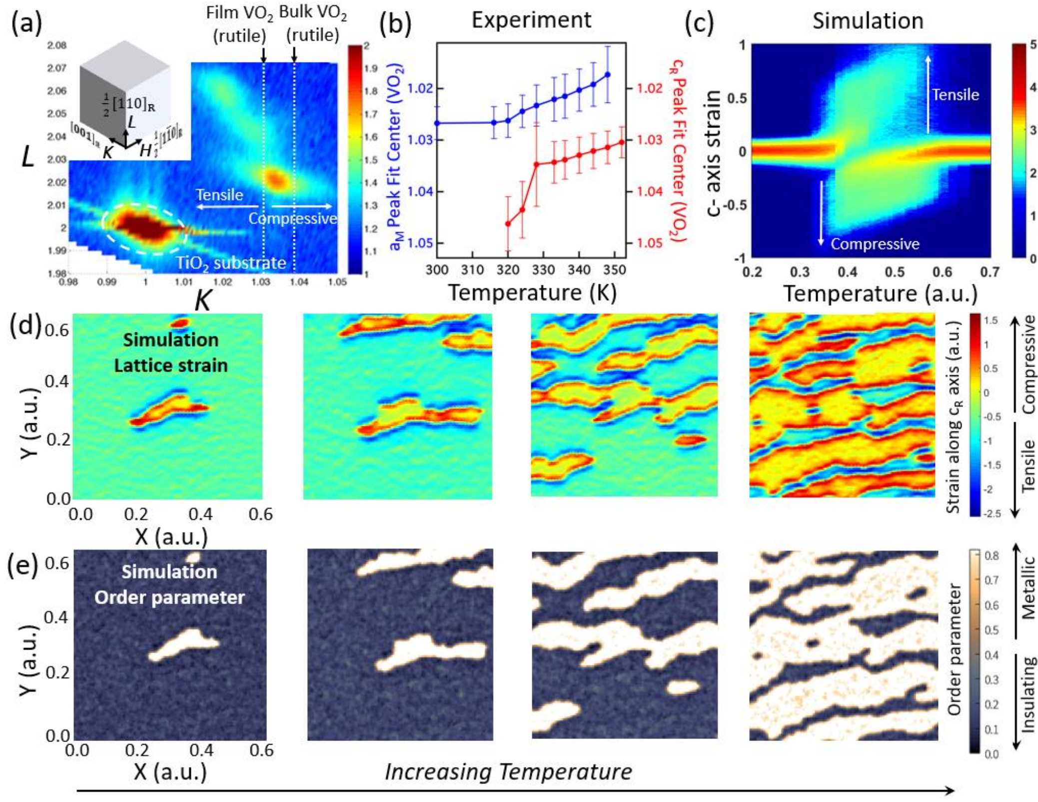

Figure 3.9: X-ray diffraction study and strain simulation of VO_2 films. (a) Crystallographic reciprocal space map of X-ray diffraction at 346 K. The inset illustrates the definition of pseudo-cubic unit cell of $[110]_R$ TiO_2 substrate and the corresponding reciprocal axes (*H, K, L*). (b) Temperature evolution of the monoclinic peak and rutile peak positions along *K*, corresponding to lattice parameters along rutile c-axis. The vertical bars represent the fitted peak width at different temperatures. (c) Simulation of the population of c-axis strains (relative to the TiO_2 substrate) encountered during the IMT. (d) Real space simulation of c-axis strains among metallic stripes, showing “hot spots” of compressive strain exceeding 1% at opposing ends of metallic stripes, which are characterized by comparatively reduced c-axis (negative strain). (e) Real space simulation of insulator/metal (dark blue/gold) regions evolving through the IMT of the VO_2/TiO_2 thin film.

3.2.4 Conclusions

The correlative study combining s-SNOM, X-ray diffraction, and Landau theory simulations reveal that the ENZ region hosts a unique intermediate state due

to strain redistribution in the thin films at the IMT. The ability to understand and spatially identify the “epsilon near zero” phase can be important for advancing fundamental understandings of exotic strain states in SCES. It will also expand our capacity to detect and locate novel states in semiconductors for nonlinear optical applications since the index of refraction $\Delta n \propto \frac{\Delta \varepsilon}{2\sqrt{\varepsilon}}$ can be dramatically changed with relatively small changes in lattice strain [90]. In this fashion, nano-imaging with the imaginary part (or the phase) of the near-field optical signal can be routinely used as better means of identifying nanoscale intermediate states between bad metals and bad insulators, which is important for the study of insulator-metal phase competition in correlated electron materials.

(Section 3.2 is based on an unpublished paper in submission in June 2019.)

Chapter 4

Terahertz Time Domain Spectroscopy

4.1 Introduction

The generation of strong ultrafast terahertz pulses has been a challenging task for a long period[91], the observation of optical rectification, i.e. the dc polarization of a potassium dihydrogen phosphate (KDP) crystal under the passage of an intense ruby laser in 1962 made the generation of high intensity broadband terahertz light possible[92]. In 1996, Budiarto *et al.* first demonstrated a 0.4 μJ terahertz pulse energy with ultrafast optical pulses at 800 nm, 150 fs pulse width and 500 μJ per pulse[93] and GaAs based photoconductive antenna. In 2002, Hebling *et al.* proposed a phase matching method to match the group velocity of optical pulses with the phase velocity of terahertz radiation[94], paving the way to the rapid increase of terahertz pulse energy to ~ 30 μJ in 2008, which used 28 mJ, 50 fs laser pulses and large-scale MgO: $LiNbO_3$ crystal[95], on the same order of that generated from accelerator-based terahertz sources (~ 100 μJ)[96]. In 2011, Hirori *et al.* reported the generation of terahertz pulses with energy ~ 3 μJ and peak electric field exceeding 1MV/cm using optical pulse energy of 4 mJ at 85 fs and repetition rate of 1 kHz.

In this Chapter I will discuss the generation of THz pulses using nonlinear optical method. A detailed experimental setup will be introduced with experimental method and data analysis for THz time-domain-spectroscopy. Then the principle of optical-pump-terahertz-probe (OPTP) will be demonstrated which is followed by an experiment on $V_{1-x}Nb_xO_2$, showing the ultrafast electron dynamics with decay time tunable with different stoichiometric ratio between vanadium and niobium.

4.2 Terahertz Generation and Detection

4.2.1 Terahertz Time Domain Spectroscopy

The ultrafast terahertz pulses discussed here are generated using optical rectification by nonlinear optical processes. In a nonlinear crystal, the relation between the electric field and electric polarization is expressed as:

$$P(t) = \chi^{(1)}E(t) + \chi^{(2)}E^2(t) + \chi^{(3)}E^3(t) + \cdots \quad (4.1)$$

Here $\chi^{(n)}$ is the electric susceptibility, $\chi^{(1)}$ is the linear term which dominates when the incoming light intensity is low. $\chi^{(2)}$ is responsible for both second harmonic generation (SHG) and optical rectification (difference frequency generation) for terahertz generation.

Nonlinear crystal zinc telluride (ZnTe) is typically used for thz generation for its simplicity in realizing phase matching between THz and optical pulses. The second order non-linear interaction is:

$$P^{(2)}(\omega_i - \omega_j) = \chi^{(2)}E^2(\omega) \quad (4.2)$$

Where ω_1 and ω_2 are frequencies within the bandwidth of optical pulses $E(\omega)$ (e.g. 60 nm around central wavelength 800 nm). The radiated terahertz electric field is proportional to the second derivative of $P^{(2)}$ and is schematically presented in Fig. 4.1.

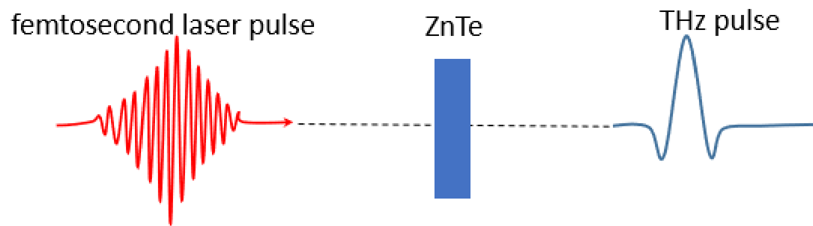

Figure 4.1: Scheme of optical rectification for terahertz generation.

Fig. 4.2 shows the schematic setup for terahertz time-domain-spectroscopy. The optical pulses with energy of several mJ/pulse are generated by a *Spitfire Ace*™ amplifier system. Femtosecond laser pulses from a independent mode-locked, Ti:sapphire seeding laser called Spectra-Physics Mai Tai SP at 80 MHz repetition rate. The seeding laser pulses are picked by a Pockels cell (electro-optical effect) so that 1000 pulses enter the amplifier per second. The amplification is realized

with a second Ti:sapphire crystal. Ti:sapphire is made by replacing a small percentage of Al^{3+} in Al_2O_3 with Ti^{3+} whose ground state is split into two broadened energy levels, the Ti:sapphire is pumped by green laser (400 nm-600 nm) from a Nd:YLF laser (*Empower 45*), and the fluorescence emission from 600 nm to 1000 nm with peak at 800 nm is illustrated in Fig. 4.3[97].

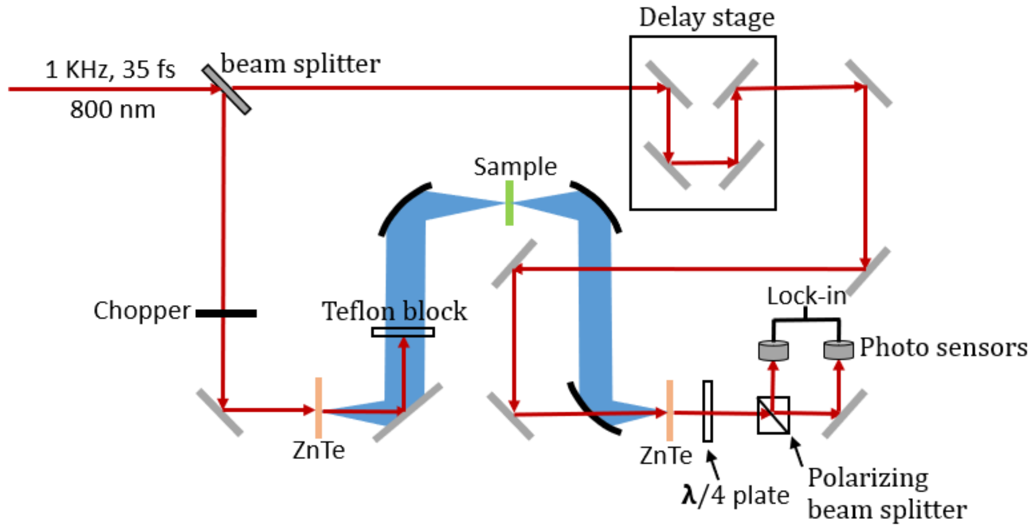

Figure 4.2: Scheme of terahertz time domain spectroscopy (THz-TDS).

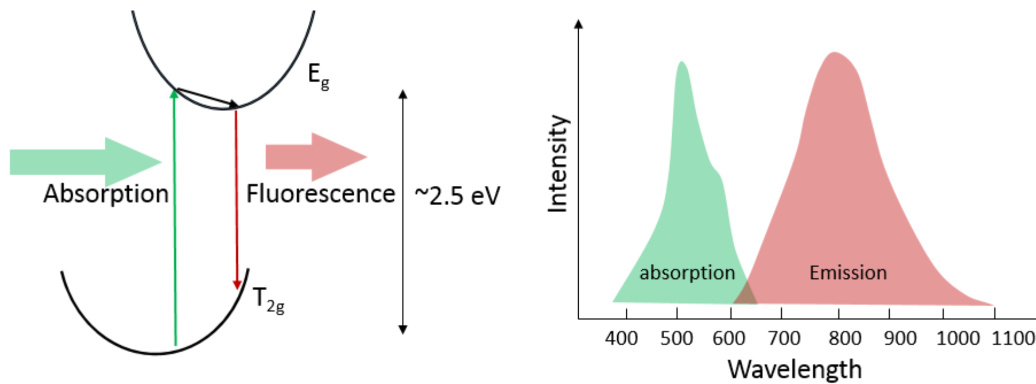

Figure 4.3: Absorption of green and blue light by Ti: sapphire crystals and emission of near infrared light.

The Ti: sapphire crystal in the amplifier is pumped to its excited state right before the seeding laser enters. The lasing process is realized by stimulated emission which duplicate the seeding pulses with the same wavelength and direction. The pulses are reflected back and forth in the Ti:sapphire crystal for several times until saturation and released from the crystal. The relation between the pulse duration time Δt and wavelength bandwidth $\Delta \nu$ is:

$$\Delta\nu \cdot \Delta t \geq 0.441 \tag{4.3}$$

For example, around 800 nm central wavelength, 100 fs pulse duration corresponds to about 9 nm bandwidth, and 35 fs pulse duration corresponds to 60 nm bandwidth. The seeding laser is stretched in time duration to reduce its peak power before entering into the amplifier which reduce the potential damage to the Ti:sapphire crystal. The stretched pulses are amplified and then compressed back again to achieve high peak power, as shown in Fig. 4.4, the scheme is called chirped pulse amplification (CPA). Stretching is realized by optical dispersion with the help of diffraction grating, in which different wavelength components have slightly different path lengths after diffracted by a pair of gratings, see Fig. 4.5, so that different wavelengths are separated in space and pulses are stretched. Compression is realized in the reversely.

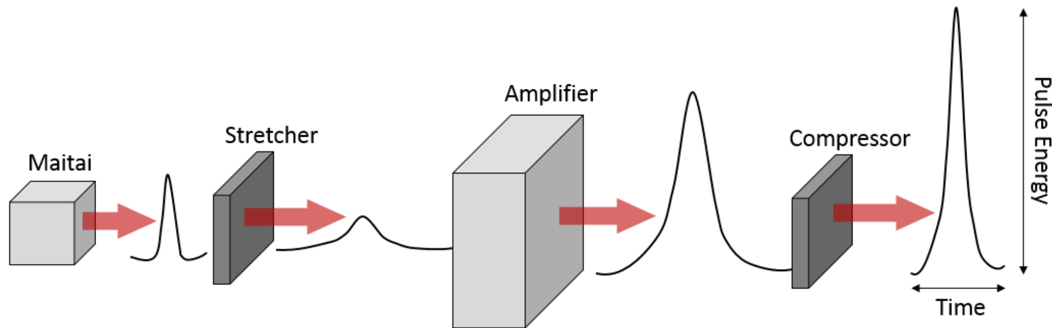

Figure 4.4: Scheme of chirped pulse amplification (CPA).

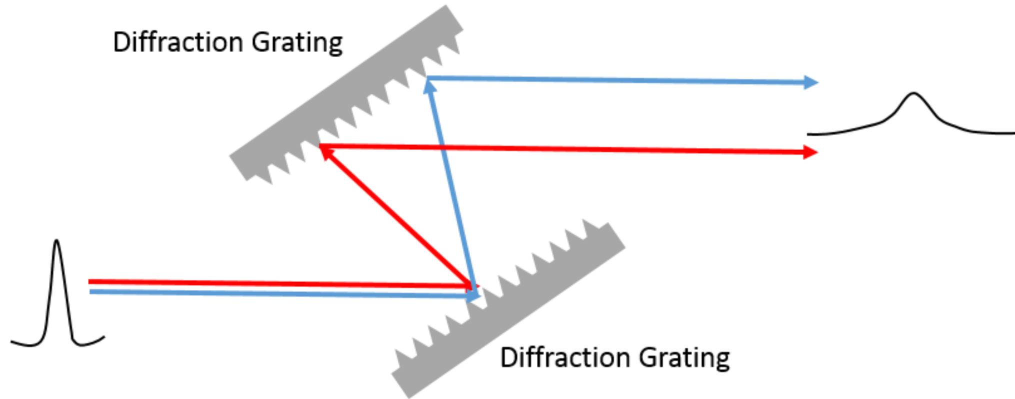

Figure 4.5: Working principle of a stretcher to expand the seeding pulses in time duration.

The output pulses from the amplifier have central wavelength at 800 nm, bandwidth 60 nm, average power of ~ 5W, time duration time ~ 35 fs and repetition rate at 1 KHz. The pulses are attenuated and guided to a beam splitter as shown in Fig. 4.2, the reflected part is used for the generation of terahertz pulses (probe beam) while the transmitted pulses are used for detection (gate beam). The IR probe beam with an average power of 560 mW is modulated by a mechanical chopper at 500 Hz and then transmit through a ZnTe single crystal, the generated terahertz pulses transmit through a Teflon plate which blocks the IR beam. Terahertz pulses are focused by a 2-inch parabolic mirror on a sample and transmit, guided by another pair of parabolic mirrors and focused onto a second ZnTe crystal. The total beam length of the gate beam with average power of ~125 mW is controlled by a motorized delay stage from *Newport* (UTS100PP) with a controller (model ESP301). The probe beam is then guided to the focal point of the terahertz beam on the second ZnTe.

The detection scheme is called “electro-optical sampling”, which is also a second order nonlinear effect[98]. The electric field of terahertz pulses causes a change of index of refraction of ZnTe in the near infrared range (gate beam). As shown in Fig. 4.6, the THz and gate beam transmit through 1 mm-thick (110)-orientated ZnTe crystal, here α is the angle between the THz (gate) beam polarization and (001) direction of ZnTe. In absence of THz beam, due to the anisotropy of crystal direction, the transmitted gate beam is elliptically polarized, the elliptically polarized gate beam is modified by a subsequent quarter wave plate to become a circularly polarized beam. At last, the circularly polarized beam is spit into in-plane and out-of-plane polarized beam by a Wollaston prism and the two beams with equal intensity are detected by two photosensors connected anti-

parallel, the generated anti-parallel electric currents cancel each other so the output is zero. The existence of THz electric field changes the index of refraction for gate beam along two transverse orthogonal directions. The change of ellipticity is dependent on the strength of THz electric field E_{THz}, the result is a difference in the

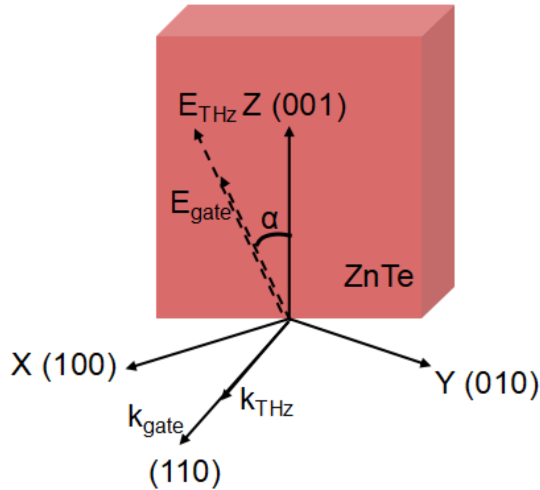

Figure 4.6: ZnTe crystal used for electro-optical sampling.

intensity of two separated gate beams, leading to net output currents at several micro amperes. The output current is amplified by a low noise preamplifier SR570 (*Stanford Research Systems*) and connected to a lock-in amplifier SR830 (*Stanford Research Systems*). The synchronization signal from the chopper is also connected with the lock-in amplifier, since the chopper is at 500 Hz, the THz is overlapped with every other gate pulse, as shown in Fig. 4.7:

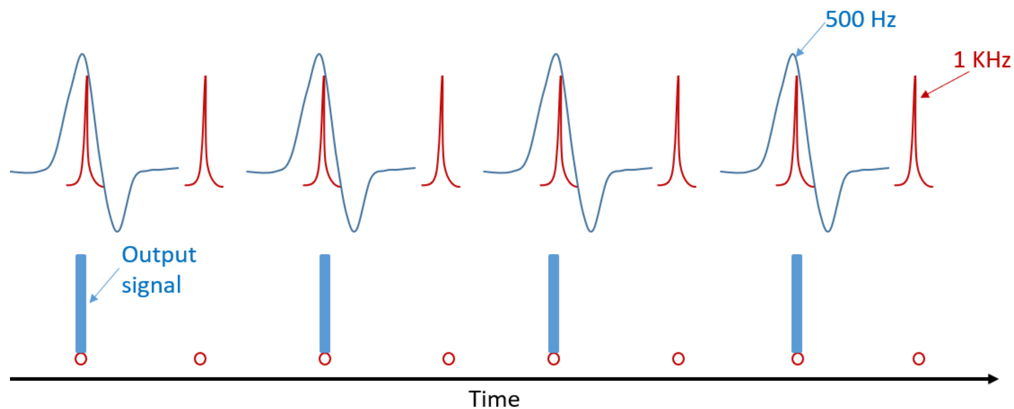

Figure 4.7: Synchronization between THz and gate pulses.

Thus, the readout signal represents the strength of electric field of THz pulse at the time overlapping with the gate pulse. By changing the delay time between THz and gate beam, a complete time dependent THz electric field can be mapped out. A typical measured THz time domain spectroscopy and spectrum after Fourier transform is shown in Fig. 4.8:

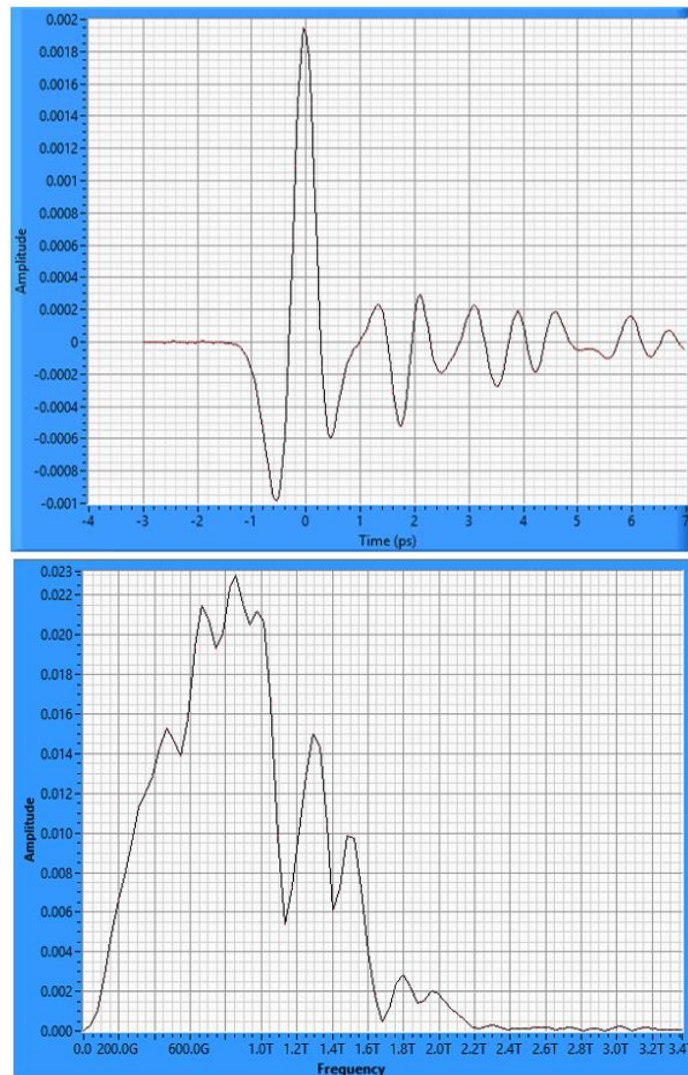

Figure 4.8: Measured THz time domain spectroscopy through air and corresponding Fourier transformed spectrum.

The following data analysis can help figure out the optical properties of samples such as the complex index of refraction:

$$\tilde{n}_2 = n_2 + ik_2 \tag{4.4}$$

The terahertz plane wave travelling through the sample with $\tilde{n}_2$ can be expressed as:

$$E(z,t) = E_0 e^{i(Kz-\omega t)} = E_0 e^{i((n_2+ik_2)\omega z/c-\omega t)} = E_0 e^{-\frac{k_2\omega z}{c}+\frac{in_2\omega z}{c}-i\omega t} \tag{4.5}$$

Here K is light momentum, the term $-\frac{k_2\omega z}{c}$ represents the decay of THz electric field during propagation. As shown in Fig. 4.9, the incident terahertz wave is reflected at both the front and back side of a sample, with transmission $T_1=2n_1/(n_1+n_2)$ and $T_2=2n_2/(n_1+n_2)$. If the sample thickness is d, the incident THz field is E_0, then the transmitted THz field is:

$$E_T(z,t) = T_1T_2E_0e^{i(Kd-\omega t)} = T_1T_2E_0e^{-\frac{k_2\omega d}{c}+\frac{in_2\omega d}{c}-i\omega t} \tag{4.6}$$

For reference, the transmitted THz field through $\tilde{n}_1$ ($\tilde{n}_1 = n_1 + ik_1$) with the same thickness d is:

$$E_{Ref}(z,t) = E_0e^{-\frac{k_1\omega d}{c}+\frac{in_1\omega d}{c}-i\omega t} \tag{4.7}$$

The total transmission $T=\frac{E_T(z,t)}{E_{Ref}(z,t)} = Ae^{i\phi}$ is a complex number with amplitude and phase which can be both obtained from the THz transmission measurements. Then with the knowledge of the index of refraction of surrounding medium $\tilde{n}_1$ (for air $\tilde{n}_1 = 1 + 0i$), $\tilde{n}_2$ can be extracted.

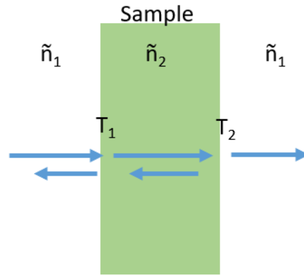

Figure 4.9: THz wave transmission through a sample.

From the index of refraction $\tilde{n}_2$ both the complex dielectric constant and conductivity can be easily inferred by the relation:

$$\tilde{\epsilon}_2 = (\tilde{n}_2)^2 \text{ and } \tilde{\epsilon}_2 = \tilde{\epsilon}_\infty + i\tilde{\sigma}/\omega\epsilon_0 \quad (4.8)$$

4.2.2 Optical Pump Terahertz Probe (OPTP)

The direct incidence of pump pulses to a sample will cause the non-equilibrium dynamics of excited electrons. Such dynamics can then be probed by a second THz pulse by varying the time delay between the pump and probe pulses. The schematic setup is shown in Fig. 4.10:

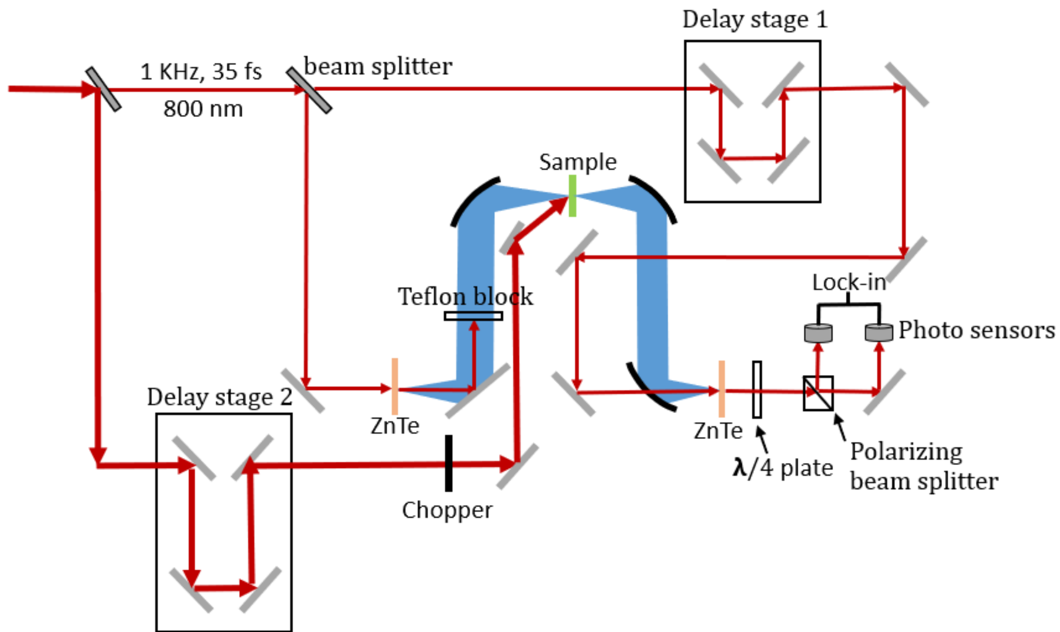

Figure 4.10: Scheme of optical pump terahertz probe (OPTP).

The setup is similar to THz TDS with the addition of stronger pump pulse (average power~ 3W, pulse energy~2 mJ/cm^2) directly from the amplifier, and a second delay stage for changing the relative arrival time between the pump and THz probe onto the sample. Note here the chopper is placed in the optical pump beam. In real measurement, the gate pulse and THz pulse are usually overlapped at the THz peak position in a THz TDS setup (Fig. 4.2). Then the delay stage for gate beam (delay stage 1) is fixed and the delay stage for pump beam (delay stage 2) is

adjusted to change the time delay between pump and THz beam. The time and frequency relation of the pump, THz and gate pulses are illustrated in Fig. 4.11.

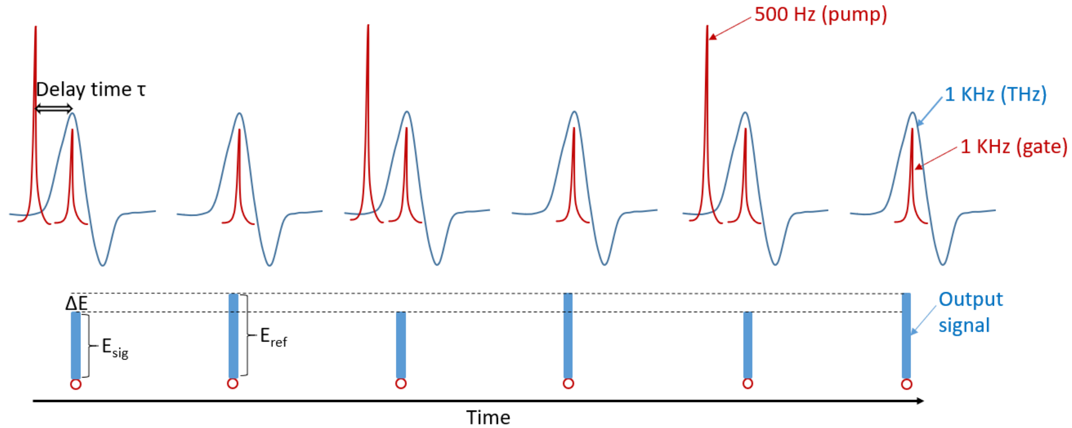

Figure 4.11: Time relation of the pump, THz and gate pulses. The pump pulses are chopped at 500 Hz

Fig. 4.12 shows the physical behavior of pump pulse excited electrons. The initial ultrafast pump pulse excites most electrons to higher energy due to the small electronic specific heat compared with lattices, leading to non-equilibrium distribution of electron energies, this non-equilibrium distribution relaxes to a hot Fermi distribution due to electron-electron interactions within several hundred femtoseconds, this process is accompanied with a change of transmission ΔT of probing THz wave. The second step is the loss of electron energy to the lattice due to electron-phonon interaction (several ps), followed by thermal diffusion of phonon energy to the substrate in the (hundreds of ps) and ΔT decays back to zero.

When the time delay between the pump and THz pulse is τ, i.e. the THz pulse arrives with time τ behind the pump, the excited electrons in the sample will block the transmission of THz peak, corresponding to a decrease in detected output signal ΔE, as shown in Fig. 4.11. The next THz pulse without pump (assuming the sample has fully recovered to its initial state within the time between the two pulses) will still give the original readout. The lock-in amplifier will output the varying part of detected signal at 500 Hz frequency, which is just the pump induced change of THz electric field with time delay τ. A real OPTP experiment will be presented in the next section.

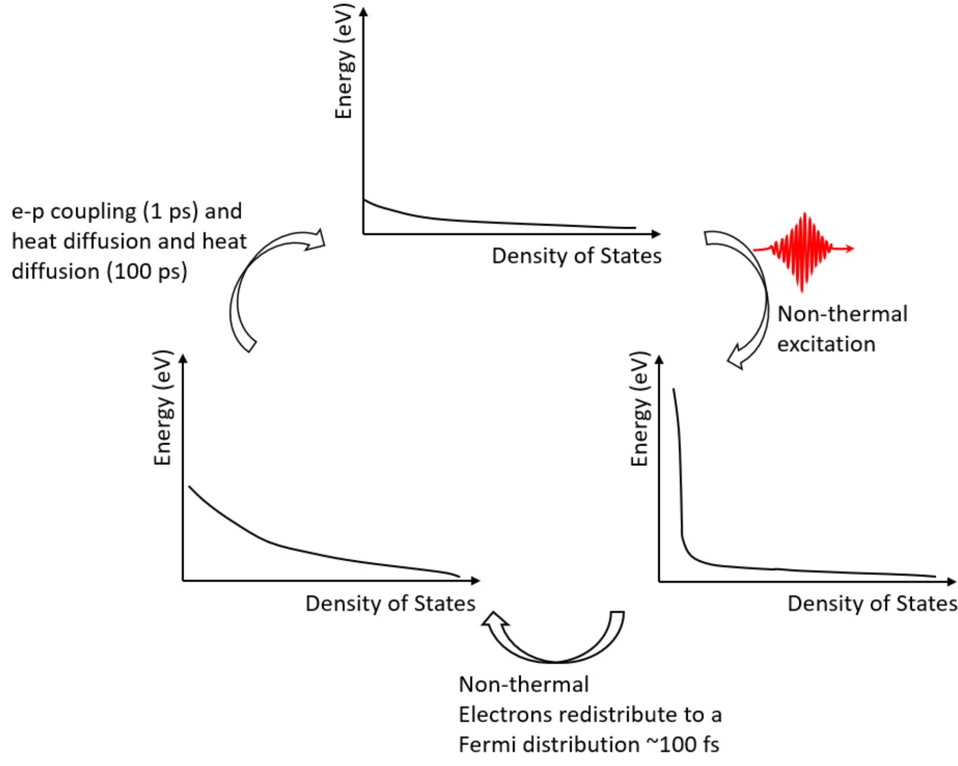

Figure 4.12: Electron energy redistribution and relaxation during the ultrafast carrier dynamics.

The time dependent change of conductivity $\Delta\tilde{\sigma}$ is a function of both frequency ω and delay time τ. For a thin film sample (thickness *d*) grown on a thick substrate with complex index of refraction $\tilde{n}_3$, the relation between the total transmission T and $\tilde{\sigma}$ of the sample (without pump) is[99]:

$$T(\omega) = \frac{E_{sig}(\omega)}{E_{ref}(\omega)} = \frac{\tilde{n}_3+1}{\tilde{n}_3+1+Z_0\tilde{\sigma}(\omega)\omega d/c} \tag{4.9}$$

So, the change of conductivity $\Delta\tilde{\sigma}$ can be deduced from the change of $T(\omega)$:

$$\Delta\tilde{\sigma}(\omega,\tau) = -\frac{\Delta T(\omega,\tau)}{T(\omega,\tau)}\frac{1}{T(\omega,\tau)}\frac{\tilde{n}_3+1}{Z_0\omega d/c} = \frac{\Delta E(\omega,\tau)}{E_{sig}(\omega,\tau)}\frac{E_{ref}(\omega)}{E_{sig}(\omega,\tau)}\frac{\tilde{n}_3+1}{Z_0\omega d/c} \tag{4.10}$$

Here the signal $E_{ref}(\omega)$, $E_{sig}(\omega,\tau)$ and $\Delta E(\omega,\tau)$ are marked in Fig. 4.11. The intuitive measurement steps to extract $\Delta\tilde{\sigma}(\omega,\tau)$ would be: 1) Take THz TDS without pump to obtain $T(\omega,\tau)$ through Fourier transforms. 2) Fix the time delay between the pump and THz pulses at a specific value τ. 3) Take THz TDS with

pump on and get a new transmission $T'(\omega, \tau)$, $\Delta T(\omega, \tau) = T(\omega, \tau) - T'(\omega, \tau)$. 4) calculate $\Delta\tilde{\sigma}(\omega, \tau)$. 5) change τ to another specific value and repeat steps 1)-4). This method is, although easy to understand, time consuming. If we assume the excitation of electron is frequency independent in the measured frequency range, a more practical way for the measurement is:

1) Measure $E_{ref}(\omega)$ using the substrate with THz TDS without pump pulses.

2) Chop and scan the pump line while fixing the THz peak with the gate pulse to obtain $\Delta E(\tau)$.

3) Chop and scan THz beam with pump pulse overlapped with gate, $E_{sig}(\omega, \tau = 0)$ is obtained which is assumed to be a constant independent of ω.

4) Calculate $\Delta\tilde{\sigma}(\omega, \tau)$ using the equation shown above.

A representative example of OPTP experiments can be found in reference[100]. In this work the ultrafast near-infrared pump pulse (1.5 eV) is used to excite quantum wells with 10 stacks of undoped 14-nm-wide GaAs layers separated by 10-nm-wide $Al_{0.3}Ga_{0.7}As$ barriers. Electron-hole pairs are generated within a few picoseconds which forms exciton population due to the scattering with phonons and defects. The THz pulse is then used to probe the transitions between internal exciton levels with energy in the range of several meV. The real part of the change of conductivity $\Delta\sigma$ and dielectric constant at 6 Kelvin are extracted. Frequency dependent $\Delta\sigma$ at a fixed time delay of 5 ps between pump and THz pulses shows a peak at 7 meV (1.7 THz) and is explained as the transition from 1*s* to 2*p* level of the excitons, and the broader shoulder at higher energy is attributed to the transition to continuum energy states. At 300 Kelvin, however, the characteristic of exciton disappears, and the spectrum matches a Drude response, indicating the formation of unbounded electron-hole pairs.

4.3 Optical Pump Terahertz Probe on $V_{1-x}Nb_xO_2$

4.3.1 Introduction

Niobium dioxide (NbO_2), a cousin dioxide of VO_2, exhibits IMT at a much higher temperature (~1081 K), which is also accompanied by a structural transformation from a body centered tetragonal (bct) to a regular rutile lattice[101]–[104]. Demonstrated in limited previous investigations, NbO_2 also appears to be a

good candidate for practical applications such as resistive memories and ultrafast switching using electric bias[105]–[107] or optical excitation[108], especially for high temperature operations.

Besides the transition temperature, the IMTs in VO_2 and NbO_2 demonstrate discrepancies in several other aspects. Compared to that of VO_2, the change in electrical conductivity of NbO_2 across IMT upon heating is less abrupt and much smaller in magnitude (> 10^5 times in single crystal VO_2 versus <10^2 times in NbO_2)[109], [110]. Moreover, for optically induced IMT, ultrafast experiments have demonstrated fast insulator to metal switching dynamics in both VO_2 and NbO_2[111]–[118]. However, in VO_2, the long recovery time from the metallic phase back to the insulator phase has prohibited fast on/off switching applications.[119] Unlike other semiconductors[120], [121], where the recovery time governed by electron-hole recombination process can be modified by forming internal electric field or introducing moderate density of defects,[122] effective tuning of response time and optical contrast between phases in correlated metal oxides is still lacking. In NbO_2, on the other hand, recent near-infrared pump-probe[108] and optical pump terahertz pump (OPTP)[123] studies showed that the recovery time can be orders of magnitude faster than VO_2. However, the photoinduced relative change of near-infrared (800 nm) reflectivity ($\Delta R/R$) or THz conductivity ($\Delta\sigma$) of NbO_2 are much smaller than those of VO_2. Therefore, by alloying these two dioxides together one may achieve better device performance (e.g. optical switching with faster recovery rates or larger optical responses). In addition, studying this alloyed system is also particularly interesting from the scientific perspective. Being formed by transition metals in the same column of the periodic table, both VO_2 and NbO_2 have one *d* valence electron that is not engaged in metal (M) - oxygen (O) bonding. Both of their IMTs at respective critical temperatures are companied by structural transformations with similar distortion in lattice.

4.3.2 Experiments

The $V_{1-x}Nb_xO_2$ ($0 \leq x \leq 1$) thin films are by reactive bias target ion beam deposition (RBTIBD) technique, with a full set of x values ranging from 0 to 1. This technique has been employed to prepare high-quality epitaxial VO_2[124] and NbO_2[125] thin films on various substrates and its capacity of co-sputtering allows for exploration of alloyed material systems[126]. The evolution of lattice structures, DC transport, THz conductivity, and photoinduced THz dynamics of the films against composition is systematically investigated.

The $V_{1-x}Nb_xO_2$ thin films are deposited on sapphire (0001) substrates using RBTIBD. During the deposition, optimized growth conditions of VO_2 (NbO_2) are employed for the deposition of V-rich ($0 \leq x \leq 0.52$) (Nb-rich, $0.55 \leq x \leq 1$) films, as listed in Table 4.1. For the deposition of V-rich (Nb-rich) films, Nb (V) target is co-sputtered using a dc pulsed bias at a frequency of 10.10 kHz (71.43 kHz) with a positive pulse period ranging from 36 μs to 55 μs (3 μs to 12 μs). All the V-rich (Nb-rich) samples are deposited for 60 min (30 min).

Deposition conditions	Parameters for VO_2	Parameters NbO_2
Substrate temperature	400 °C	450 °C
Process pressure	9×10^{-4} Torr	8.5×10^{-4} Torr
Ar/O_2 80/20 mix flow rate	6 SCCM	6 SCCM
Target potential bias	-900 V and +20 V	-900 V and +20 V
DC pulse frequency	71.43 kHz	71.43 kHz
Positive duty cycle	3 μs	3 μs
Cathode Ar flow rate and	10 SCCM and 7 A	10 SCCM and 7 A
Anode Ar flow rate and	70 SCCM and 6.5 A	70 SCCM and 6.7 A

Table 4.1: Optimized deposition condition parameters for VO_2 and NbO_2 films on sapphire (0001) substrates.

The Nb concentration, defined as x = Nb/[Nb+V] (at.%), is measured by Rutherford backscattering (RBS). The film thicknesses are determined by the X-ray Reflectivity (Smartlab, Rigaku Inc.). The film growth rate (nm/min) as a function of composition is plotted in Fig. 4.13.

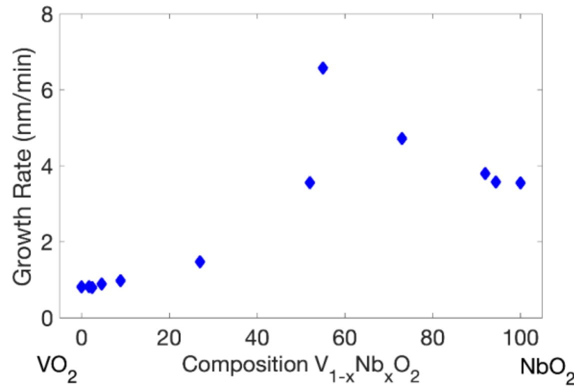

Figure 4.13: Growth rate of $V_{1-x}Nb_xO_2$ films (nm/min) as a function of film composition.

X-ray 2θ scans (Smartlab, Rigaku Inc.) are conducted to characterize phase composition, microstructures and lattice parameters of the films. In addition, X-ray ϕ scans (Smartlab, Rigaku Inc.) are employed to confirm the identification of the 2θ diffraction peaks and to find out the orientation relationship between the $V_{1-x}Nb_xO_2$ films and the substrates. Raman spectra are measured with an Raman spectroscope (Renishaw System Ltd.) using a 514 nm laser source. Temperature dependence of DC resistivity is measured using a VersaLab system (Quantum Design Inc.) from 200 K to 400 K, with a temperature ramp rate of 5 K/min. For dynamic properties, the static and photoinduced terahertz (0.2-2 THz) conductivity dynamics are characterized by applying the time-resolved optical pump (800 nm) terahertz pump (OPTP) spectroscopy with a pump power ~ 2 mJ/cm^2.

It is known that both VO_2 and NbO_2 take a regular rutile lattice ($P4_2/mnm$) for their metallic phases, which is formed by chains of edge-sharing (along *c*-axis) MO_6 octahedra linked at their corners. For their semiconducting phases, VO_2 adapts a monoclinic ($P2_1/c$) lattice and NbO_2 takes a bct ($I4_1/a$) lattice, sharing essentially the same local deviation from the rutile lattice: formation of M-M dimers along *c*-axis to yield alternating M-M bond lengths[102], [103], [127], [128].

Raman spectra of all the $V_{1-x}Nb_xO_2$ films are shown in 4.14(a). Considering their similar lattice structures, it is not surprising that the pure VO_2 and NbO_2 films (x = 0 and 1) exhibit similar Raman features, which agree well with the previously reported results[129], [130] . The two bands at lower frequencies (194 cm^{-1} and 225 cm^{-1}) correspond to the stretch and twist modes of the V-V dimers[131], and the Raman shift near 620 cm^{-1} in VO_2 spectrum is related to the symmetric stretching mode of the basal oxygen ions within the VO_6 octahedra[132]. Accordingly, for the spectrum of NbO_2, the Raman bands at 158 cm^{-1} and 183 cm^{-1} could be related to the vibration modes of the Nb-Nb dimers due to the heavier Nb atoms, and the band near 860 cm^{-1} could be associated with certain vibrational mode within the NbO_6 octahedra.

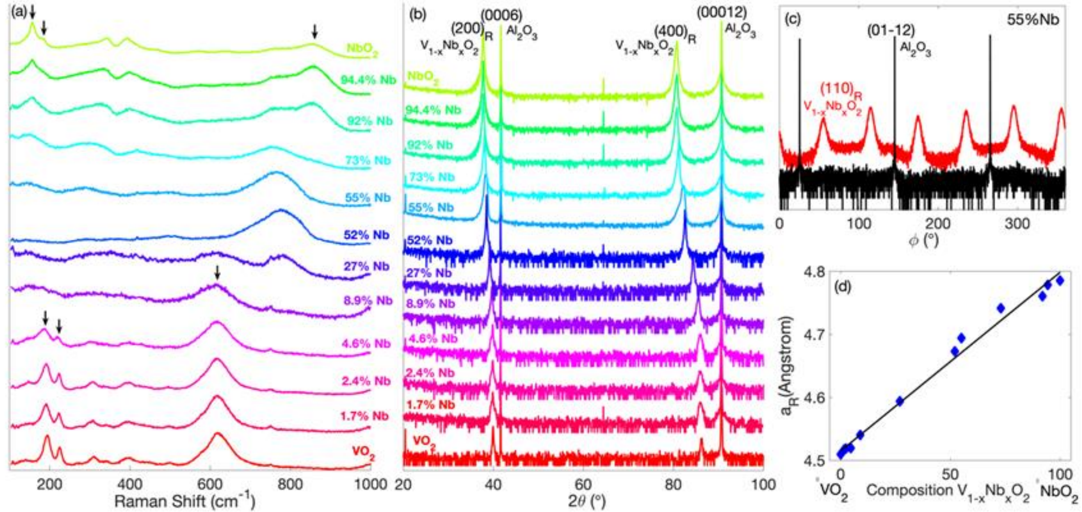

Figure 4.14: (a) Raman spectra and (b) X-ray 2θ scans of $V_{1-x}Nb_xO_2$ films; (c) X-ray ϕ scans of (400) diffraction of rutile lattice for the $V_{0.45}Nb_{0.55}O_2$ film at 2θ = 26° and χ = 45°, and $(01\bar{1}2)$ diffraction of sapphire substrate at 2θ = 25.5° and χ = 12.8°; (d) Lattice constant (a_R) as a function of Nb concentration (x). Measurements are taken at room temperature.

As the composition moves from pure VO_2 or NbO_2 towards $V_{0.5}Nb_{0.5}O_2$, the two bands related to M-M dimers decrease rapidly in intensity and become absent for samples with composition $0.089 \leq x \leq 0.73$. As Nb(V) substitution is introduced into VO_2(NbO_2), it is expected that the M-M dimers will be broken, leading to a decrease of M-M chains tilting along c-axis, detwisting of MO_6 octahedra, and therefore transition of surrounding lattice to a more symmetric, rutile structure[133]. The disappearance of the low-frequency Raman features could indicate the collapse of respective low-temperature symmetry of VO_2 and NbO_2. The broad Raman band developed between 620 cm^{-1} and 860 cm^{-1} for samples with composition ranging from $x = 0.27$ to $x = 0.73$ is suspected to be related to certain M-O vibration modes within MO_6 octahedra, with the strength of vibration being varied by M-O bond length and local distortion of MO_6 octahedra. It is worth noting that no Raman feature of other oxide phases of vanadium or niobium is observed, suggesting that a solid solution has been maintained over the whole range of composition.

4.14(b) shows the out-of-plane X-ray 2θ scans of the $V_{1-x}Nb_xO_2$ films, where 2θ is the angle between the incident and diffracted X-ray beams. All samples

exhibit diffraction peaks near $2\theta = 40°$ and $2\theta = 86°$. For clarity, all the samples are indexed on the basis of the rutile structure, although the rutile symmetry is distorted when x is close to 0 (VO_2) or 1(NbO_2). The diffraction peaks correspond to (200) and (400) peaks of the rutile lattice. (For the low-temperature lattices, they correspond to (020) and (040) diffractions of the VO_2 lattice, and (440) and (880) diffractions of the NbO_2 lattice, respectively.) No other diffraction peaks corresponding to any other vanadium oxide or niobium oxide phases are present, which again confirms that solid solutions instead of mixed phases are formed over the whole range of composition.

To confirm the assignment of out-of-plane 2θ diffraction peaks, X-ray ϕ (the in-plane orientation of the sample stage) scans are conducted on (110) diffraction of rutile $V_{1-x}Nb_xO_2$ lattice at $2\theta = 26°$ and $\chi = 45°$ (χ is the tilted angle of the sample stage) based on the lattice symmetry, an example of which is shown in 4.14(c) (on the sample with composition $x = 0.55$). Furthermore, the observation of six diffraction peaks, combined with the X-ray ϕ scans of sapphire $(01\bar{1}2)$ diffraction at $2\theta = 25.5°$ and $\chi = 12.8°$, indicates that the orientation relation between the deposited films and substrates is $\langle 001\rangle(100)_R V_{1-x}Nb_xO_2 \| \langle 10\bar{1}0\rangle(0001)Al_2O_3$, the same as that between pure VO_2/NbO_2 films deposited by RBTIBD technique and (0001) sapphire substrates[125], [134].

With the increase of x, film peaks shift towards lower 2θ angles, corresponding to an increase of lattice constant along a-axis of the rutile lattice (a_R). 4.14(d), values of a_R are extracted from the 2θ peak positions of $(200)_R$ diffraction and plotted as a function of x, with the black line showing the linear fitting. The increasing trend of a_R with the increase of Nb concentration is due to the larger size of Nb ion, as the effective ionic radius of V^{4+} and Nb^{4+} in octahedral coordination are 0.58 Å and 0.68 Å, respectively[135]. In addition, previous studies have pointed out that the Nb (V) substitution introduced into VO_2 (NbO_2) would exist as Nb^{5+}(V^{3+}), with resulting V^{3+}(Nb^{5+}) nearby, because of the instability of Nb 4d electrons compared with that of the V 3d electrons[136], [137]. The effective ionic radii of V^{3+} and Nb^{5+} in octahedral coordination are both 0.64 Å[135]. Thus, the deviation from the linear fitting can be accounted for by the variation in the size of ions.

Fig. 4.15(a) shows the temperature dependence of DC conductivity in all $V_{1-x}Nb_xO_2$ samples from 200 K to 400 K. First, samples with Nb concentration up to $x = 0.089$ demonstrate the temperature-driven IMT. With the increase of x, IMT occurs at lower temperatures with smaller and less abrupt changes in the film conductivity at IMT. The film conductivity of the semiconducting state is enhanced significantly by the Nb substitution, while that of the metallic state only exhibits a

slight reduction. As Nb substitution is introduced into VO_2 films, it is expected that the breaking of Peierls distortion geometry and weakening of electronic correlation within the V-V dimers would result in the decrease of band gap, leading to the decrease of transition temperature and increase of conductivity (of semiconducting phase) [138]–[140]. Similarly, for samples with composition close to pure NbO_2 ($0.92 \leq x \leq 1$) and maintain the bct lattices, the conductivity also increases as the V substituting level increases.

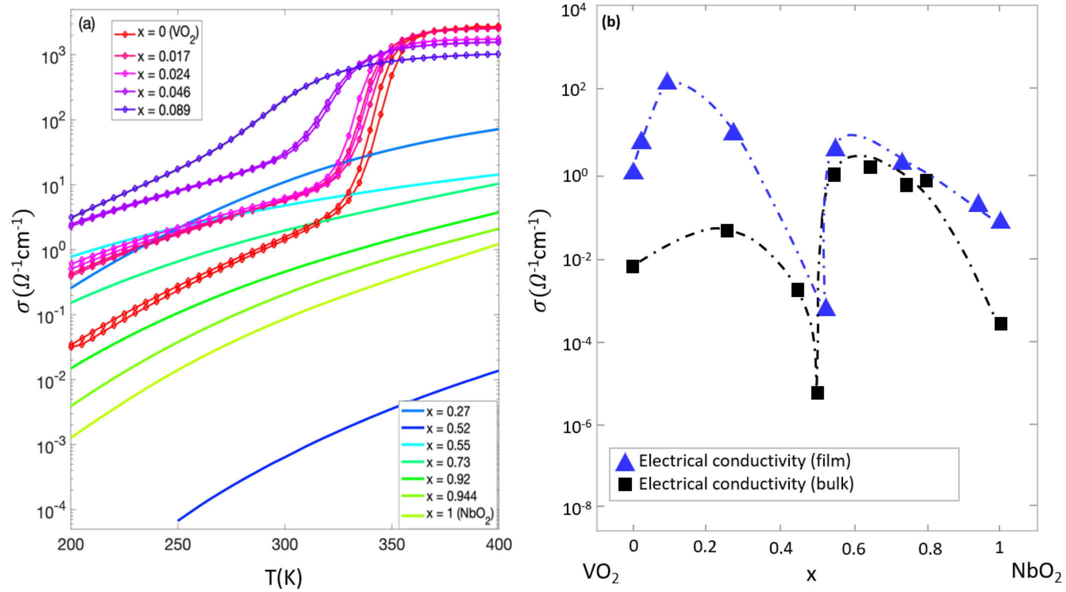

Figure 4.15: (a) Temperature dependence of film resistivity of $V_{1-x}Nb_xO_2$ films from 200 K to 400 K; (b) Electrical conductivity and photoinduced conductivity change of $V_{1-x}Nb_xO_2$ as a function of Nb concentration (x). The conductivity data of bulk $V_{1-x}Nb_xO_2$ crystals is adapted from reference [141].

An interesting observation is that for those samples with intermediate Nb concentration ($0.27 \leq x \leq 0.73$), the films remain semiconducting despite that the monoclinic (bct) symmetry of VO_2 (NbO_2) has collapsed. In addition, the film with composition closest to $V_{0.5}Nb_{0.5}O_2$ (the one $x = 0.52$) exhibits conductivity much lower than all the other samples. The composition dependence of the film conductivity at 300 K is summarized in 4.15(b). Similar composition-dependent behavior of conductivity has also been observed in bulk crystals previously (as is shown by the black line in Fig. 4.15(b)).[141] In addition, we notice that the photoinduced THz conductivity change shares roughly the same trend. As shown in 4.15(b), the maximum change of photoinduced THz conductivity at a pump

fluence of ~2 mJ/cm^2 also demonstrate the valley behavior for the sample with x = 0.52. The detailed ultrafast dynamics features will be described below.

To investigate the effect of cation substitution on the ultrafast dynamics of the $V_{1-x}Nb_xO_2$ samples, time-resolved THz conductivity dynamics are characterized by the OPTP spectroscopy, which are shown in Fig. 4.16(a) and (b). As is shown in Fig. 4.16(a), the samples with Nb content up to 27% demonstrate a long-lived conductivity upon the excitation of the pump pulse, while for other samples with higher Nb concentration, the THz dynamics exhibit long-lived but slowly decaying conductivity after the initial fast partial decay (shown in Figure 4.16(b)). The magnitude and lifetime of the photoinduced THz conductivity strongly depend on the film composition.

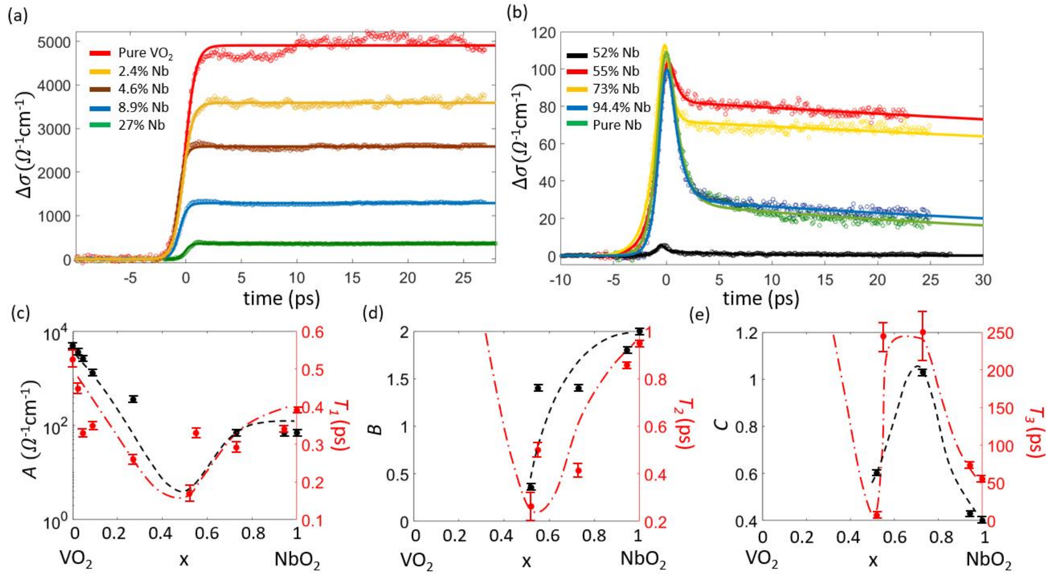

Figure 4.16: Optically induced THz photoconductivity change ($\Delta\sigma$) of $V_{1-x}Nb_xO_2$ films as a function of time for Nb concentration x (a) below and (b) above 0.27; **(**c)-(e) composition dependence of fitted parameters describe (c) the rise term, (d) the fast decay term, and (e) the slow decay term.

To quantitatively describe the measured THz conductivity dynamics of these samples, the THz conductivity transient is fitted using the following equation

$$\Delta\sigma(t) = \frac{A}{1+e^{-\frac{t-a}{T_1}}}\left(Be^{-\frac{t}{T_2}} + Ce^{-\frac{t}{T_3}}\right) \tag{4.11}$$

in which there is one rise term characterized by time T_1 with amplitude A, and two decay terms described by time constant T_2 with amplitude B (fast decay), and time constant T_3 with amplitude C (slow decay), respectively. The composition dependence of these fitted parameters is summarized in Fig. 4.16(c) to (e). Both T_1 and A are first suppressed with the increasing of x, reaching a minimum at $x = 0.52$ and then increase again at higher Nb concentration, as is shown in Fig. 4.16(c). For the THz conductivity transients shown in Fig. 4.16(a), only the rise term ($\frac{A}{1+e^{-\frac{t-a}{T_1}}}$) is employed in the fitting, as negligible decay is observed during the first 30 ps for samples with low Nb doping. Thus, in Fig. 4.16(d) and (e), the fitted decay parameters (B, T_1, C, and T_2) are absent for $x \leq 0.27$ and only speculated trends are plotted. As shown in Figure 3(d), the fast decay (for x> 0.5) takes place within ~1 ps after the photo-excitation, and its magnitude takes increasing percentage of the maximum photoinduced THz conductivity change as the Nb content increases. Compared with the fast decay, the slow decay term varies more dramatically against composition. The value of T_3 drops from several hundreds of picoseconds to a few tens of picoseconds as the film composition approaches pure NbO_2.

It is important to see that the sample $x = 0.52$ exhibit smallest photoinduced $\Delta\sigma$ and fastest "semiconductor-like" decay. This suggests the strong immobility of carriers following the excitation of above bandgap photoexcitation and is consistent with its insulating nature in DC transport.

4.3.3 Discussions

A. Semiconducting DC transport behavior of $V_{1-x}Nb_xO_2$ samples with rutile lattice

VO_2 and NbO_2 have similar band structures near the Fermi level, which are composed by the π-type overlap between V 3d/Nb 4d and O 2p orbitals with t_{2g} octahedral symmetry determined by the symmetry of MO_6 octahedra. In addition, as the MO_6 octahedra share edges along c-axis, the orthorhombic symmetry of the crystalline field further degenerates the antibonding π band into the $d_{||}$ and the e_g^{π} band. For metallic phase, the $d_{||}$ band overlaps with the e_g^{π} band, with the Fermi level lying in the middle of them. For semiconducting phase, the $d_{||}$ band is split into the bonding and antibonding band and the e_g^{π} band is lifted up, giving up to the band gaps[129], [142]–[144]. Regarding the origin of the IMT or the nature of the semiconducting phase, for VO_2 dispute centers about the relative contribution from the increased electronic correlation (Mott-Hubbard mechanism) and the metal dimerization (Peierls mechanism). For NbO_2 it is generally agreed that the latter

should play a more important role due to the larger overlap of 4*d* orbitals/stronger Nb-Nb bonding, but electronic correlation also contribute to the band gap formation, although to a less extent, as is revealed by recent DFT and cluster-dynamical mean-field calculations[145].

For samples with composition ranging from x = 0.089 to x = 0.73, it is expected that the Peierls insulation is destroyed because of the transformation in lattice structure due to cation substitution, and the semiconducting transport behaviors despite the rutile lattices could be attributed to the electronic correlation (Mott-Hubbard mechanism) and the enhanced randomness of film lattice (Anderson localization). A strong enough combination of Coulomb repulsion and lattice disorder could result in the localization of charge carriers and give rise to the observed semiconducting transport behavior[136]. In this scenario, the intrinsic electrical conduction could be realized by the electronic hopping of charge carriers. Since the cation substitution result in the formation of Nb^{5+} and V^{3+} in the $V_{1-x}Nb_xO_2$ system, the real structure of the film is $V_{1-2x}^{4+}V_x^{3+}Nb_x^{5+}$for 0<x<0.5 and $V_{1-x}^{3+}Nb_{1-x}^{5+}Nb_{2x-1}^{4+}$ for 0.5<x<1. In principle the charge carrier hopping will occur between the same type of cations, which is essentially the position change of the same type of cations. This might explain why the film conductivity exhibits enhancement around the composition where the amount of V^{3+} and V^{4+} (Nb^{4+} and Nb^{5+}) are close[136], [141]. The change in the cations that conduct the electricity, combined with the distribution of lattice disorder, could account for the observed variation in the DC transport features against the film composition. At last, the conductivity minimum occurs at x ~ 0.5 can be interpreted as the complete demobilization of conduction carriers due to the valence states V^{3+}/Nb^{5+}[146].

B. Ultrafast dynamics of $V_{1-x}Nb_xO_2$ samples

Since the pump energy (1.55 eV) is well above the bandgap of VO_2 (0.6-0.7 eV)[114] and NbO_2 (indirect bandgap of 0.7 eV and direct bandgap of 1.24 eV)[147], [148], the interband photoexcitation will lead to generation of a large number of non-equilibrium carriers and thus the rise of THz conductivity. Previous studies of VO_2 have shown that when the excitation density (pump pulse fluence) falls below certain critical value, the full IMT cannot be triggered and the photo-induced carriers relax through various pathways in a few picoseconds, giving rise to the semiconductor-like decay features of $\Delta\sigma$[131], [149]. When the excitation density exceeds a certain threshold, the persistence of photoconductivity change indicates that the film has transitioned to a uniform metallic state[150]. It has been reported that the instantaneous modification of electronic correlation by optical excitation could cause sub-picosecond band gap collapse and metal-like optical response, while the establishment of the long-range rutile order may take up to several 10-100 ps[151]. Moreover, under certain pump fluence or certain external

conditions (such as low temperature), the VO_2 films were found to transit to an electronic metallic state with the monoclinic symmetry maintained[152], [131].

As a tentative explanation to the measured photoinduced conductivity dynamics, the long-lived THz conductivity observed for all the samples (except for the sample x = 0.52) indicates that a metastable metallic state is formed by the excitation of pump pulse. Moreover, the absent of slow increase of the THz conductivity change over a time scale of ~ 10^2 picoseconds suggest that the full structural transition to rutile lattice has not been triggered. This observation is consistent with other OPTP studies on VO_2[131] and NbO_2[123] films, where the threshold pump fluence to trigger the structural transition is higher than what has been used in our study (2 mJ/cm^2). The metallic response can be attributed to the suppression of the Coulomb repulsion and the resulted collapse of the band gap, which essentially breaks the Mott insulation. The fast partial decay shown in Fig. 4.16(b) can be ascribed to the electron-phonon interaction during which the energy is transferred to the lattice, and much shorter processes (within 1 ps) such as electron-electron scattering, localization or self-trapping of photocarrier can also be included.[123], [131] The slow decay characterized by T_3 can be assigned to the recovery of the metastable metallic state to the initial semiconducting state, which is faster in Nb-rich samples. The recovery rate of the photoinduced metallic state, as well as the magnitude of the THz photoconductivity change exhibited by the metallic state, could be mediated by factors including the remaining semiconducting percentage of the film, pathways of energy relaxation, and so on, with strong dependence on the film composition. Further temperature-dependent and pump fluence-dependent studies can be conducted to achieve a more comprehensive understanding on the transition and recovery mechanisms of the alloyed films upon photo-excitation.

4.3.4 Conclusion

In summary, $V_{1-x}Nb_xO_2$ ($0 \leq x \leq 1$) thin films on sapphire (0001) substrates have been prepared using RBTIBD technique. Structural characterization demonstrated that the whole system constituted a continuous series of the solid solution, and no separated phases were observed. With the increase of cation substitution, the low temperature lattices of pure VO_2 and NbO_2 transited to more symmetric rutile lattices. Despite the changes in the lattice symmetry, the orientation relationship between the films and substrates remained unchanged by cation substitution as $\langle 001\rangle(100)_R V_{1-x}Nb_xO_2 \| \langle 10\bar{1}0\rangle(0001)Al_2O_3$. Temperature-dependence of DC conductivity has been examined from 200 K to

400 K and temperature-driven IMT was observed for films with Nb concentration below 8.9%. Films adapting rutile lattices still demonstrate semiconducting electrical transport behaviors at the vicinity of the T_c. Dramatic composition dependence of DC transport and ultrafast dynamics properties has been observed and an "inert" substituting level at $x \sim 0.5$ was demonstrated to display a lack of both static and photoinduced conductivity. The highly tunability of decay time makes $V_{1-x}Nb_xO_2$ a potential candidate for ultrafast optical switches in wire or wireless data transmission.

(Section 4.4 is based on paper no. 4 in the publication list above.)

Chapter 5

Terahertz Near Field Microscopy and Spectroscopy

5.1 Introduction

The early demonstration of terahertz (THz) subwavelength imaging using metal tips dates to 2002 when van der Valk et al. applied a tip to the proximity of a (100) oriented GaP crystal which was illuminated with a THz pulse and synchronized optical gate pulse as shown in the THz TDS setup in Chapter 4. The detected THz signal by electro-optical effect near the tip is strongly enhanced and smallest resolved THz focal spot has a diameter of 18 μm[153]. In 2003, Chen et al. realized a spatial resolution of 150 nm for 2 THz pulses using a tungsten tip to scan across metallic stripes on silicon substrates[154]. In the two experiments the metallic tips have no amplitude modulation and the detected signal contains a large portion of background radiation. In 2008, Huber et al. demonstrated a THz s-SNOM with interferometric detection method used in the IR s-SNOM system to reach a resolution of ~ 40 nm at 2.5 THz. By imaging the cross section of a transistor, a map of nano-scale carrier density distribution can be clearly seen[155].

In this chapter I will briefly introduce the scheme of THz s-SNOM and the near field OPTP which is the combination of AFM with THz far field systems. An example of THz s-SNOM on graphene samples will be presented in the following section.

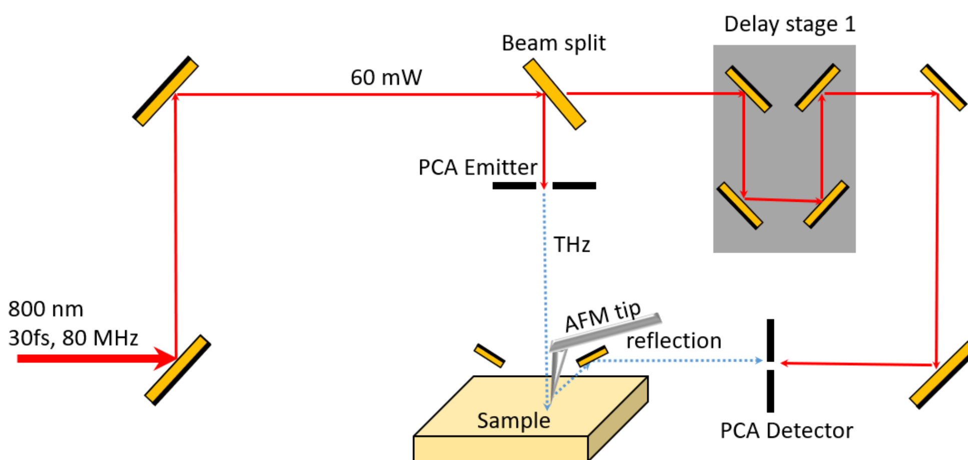

Figure 5.1: Terahertz s-SNOM on semiconductor transistors.

The THz s-SNOM is similar with the far field THz TDS with several minor differences. First, the mechanical chopper used in far field THz TDS system is absent and the signal modulation is realized by the AFM tip (~ 80 μm long, Rocky Mountain Nanotechnology, 25Pt300B-40) tapping at frequency of ~ 30 KHz. Second, the infrared pulse for THz generation comes directly from the seeding laser with repetition rate at 80 MHz. This is because the repetition rate of incident light should be higher than the tip modulation frequency so that the pulses from the amplifier which is 1 KHz can't be used. Third, the generation and detection of THz wave is realized by a pair of photoconductive antennas (PCAs) for the need for high peak power. The PCAs are made on a low-temperature epitaxial grown GaAs substrate (LT-GaAs) and a high-resistive collimating silicon lens. The structure of the generator (T-Era-100A-800-Air, TeraHertz Store) is shown in Fig. 5.2.

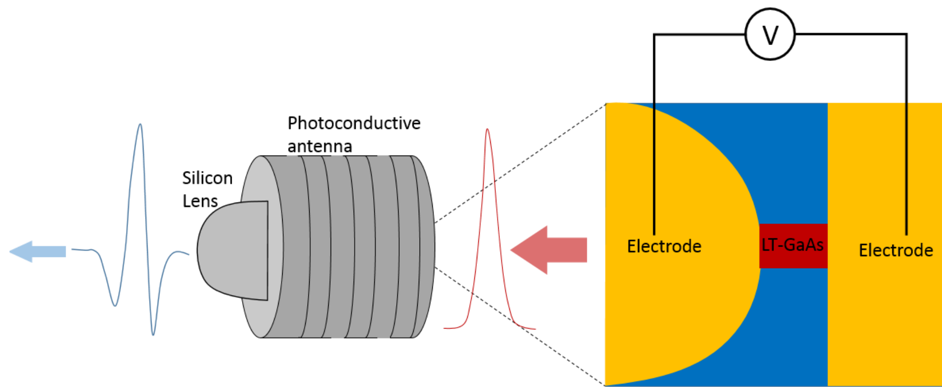

Figure 5.2: Structure of photoconductive antenna for THz generation.

The incident 800 nm optical pulses (average power ~ 30 mW) generate photocarriers at a rate proportional to the profile of pulse envelope in the LT-GaAs and are accelerated under a DC bias (~ 70 V), producing a rising electric current. The decay of the current is determined by the carrier life time which is controlled to be below 1 ps by introducing defects in LT-GaAs. The transient current is responsible for the generation of THz pulses[156].

The generated THz pulses are guided and focused to the AFM tip. Due to the difficulty of direct visualization of THz light, a visible diode laser is used for alignment with an ITO plate transparent to visible light and effectively reflects THz wave. The scattered THz light from the tip-sample interaction region is guided and focused to a second antenna for detection. The detection antenna has similar structure with the generator and is illuminated with a 30 mW 800 nm optical pulse spit from the incident beam (gate beam). The generated photocarriers is accelerated by the electric field of the THz pulse without DC bias applied to the detector. The

output current (~10 pA) is dictated by the amplitude of electric field in THz pulses and is amplified with an ultra-low-noise current amplifier (LCA-400K-10M, 10^7 V/A, Femto) to a lock-in amplifier. By changing the delay time between the gate beam and THz beam, the THz TDS can be mapped out similar to that using nonlinear crystals.

The near-field OPTP is schematically shown in Fig. 5.3 with the addition of pump line with a second delay stage, the working principle is identical to that introduced in Chapter 4 except that the output signal is E_{sig} rather than ΔE because the pump and THz beam are both modulated by the oscillating AFM tip at 30 KHz.

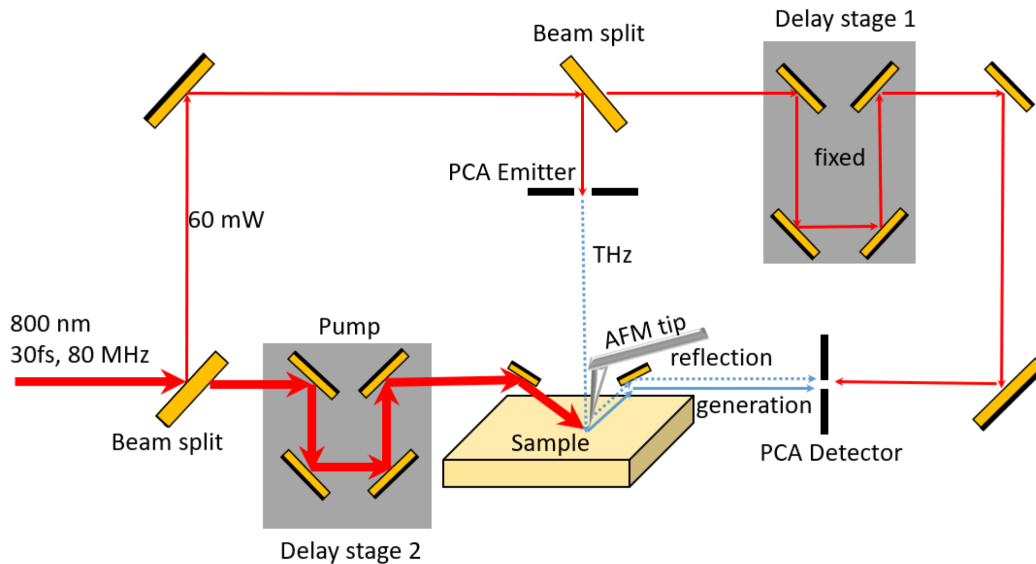

Figure 5.3: Image and structure of photoconductive antenna for THz generation.

A comparison between the far field and near field THz spectrum is shown in Fig. 5.4(a), the red curve represents the "far-field" terahertz spectrum (S_0) of a gold sample, which is measured by modulating the terahertz light with a chopper at 500 Hz without involving the tip (experimental schematics shown in Fig. 5.4(b)). S_1 (black curve) and S_2 (blue curve) are obtained by measuring the tip scattered signal of the same sample (Fig. 5.4(c)) and demodulating at the 1st and 2nd harmonic of tip tapping frequency, respectively. The experiments between far-field and near-field experiments share the same setup, except for the fact that the near-field measurements detect tip-scattered signal instead of the direct reflection from the sample surface. Therefore, the dip at 0.75 THz is clearly linked to the light

interaction with the tip-cantilever ensemble. The drop of THz signal at lower frequency below 0.5 THz could be due to the fact that the electromagnetic wave with longer wavelength can't effectively focus and efficiently induce enhancement between tip and sample surface due to the mismatch of the tip and the wavelength. This low frequency drop of the near-field signal has been observed in previous work as well[157].

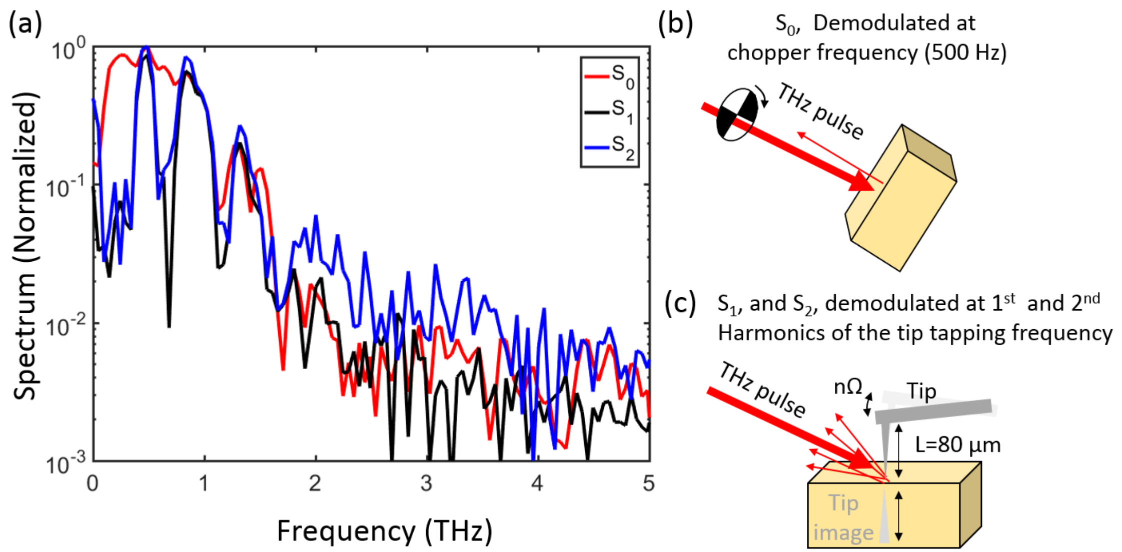

Figure 5.4: Comparison between far field and near field spectrum and measurement setup on gold. (a), rescaled THz spectrum of S_0 (far field) and S_1, S_2 (near field) signal. A dip is clearly visible in S_1 and S_2 compared to S_0 at around 0.7 THz. (b), schematic setup for the measurement of S_0. (c), schematic setup for the measurement of S_1 and S_2.

5.2 THz s-SNOM on Graphene

5.2.1 Introduction

Terahertz technology, the application of electromagnetic wave ranging from 0.1-10 THz (~3000 μm to ~30 μm), has demonstrated a great potential in material identification[158], security screening[5], and high-speed communications[159]. In particular, THz imaging promises to be a unique and powerful technique for low energy and spatially resolved spectroscopy of

biological[160]–[162] and solid state materials[163], [164]. Conventional THz 'far-field' imaging with q close to zero, however, only reaches sub-millimeter resolution due to the diffraction limit[163], [165]. Therefore, to image small objects such as biological molecules or nanoparticles with sizes far below micrometer sizes, a near-field THz system is highly demanded[155], [166]–[168].

Graphene has been demonstrated to possess fascinating optical properties in the THz frequency range, primarily due to its unique Dirac band structure, high carrier mobility and good electrostatic tunablity[169]–[173]. In the far-field, graphene and graphene devices can be used as THz modulators with a tunable absorption ranging from below 10% to above 90% [174]. In the near-field, graphene carries plasmon polaritons at IR and THz ranges[175]–[179], promising on-chip optoelectronic applications at the nanoscale. Previous studies has revealed that the number of graphene layer has a dramatic impact on the near-field response in the mid-infrared regime[180]. In this work, using a THz scattering-type scanning near-field optical microscope, we show that, in contrast to the low THz reflection in the far-field measurements[181], graphene can be regarded as an almost perfect THz reflector down to a monolayer at sufficiently high in-plane momentum q ($> 10^5$ cm^{-1}). Such strong near-field THz reflection is directly associated with graphene's large in-plane conductivity probed by high q optics.

The schematic of THz s-SNOM introduced in section 5.1 is shown in Fig. 5.5(a).

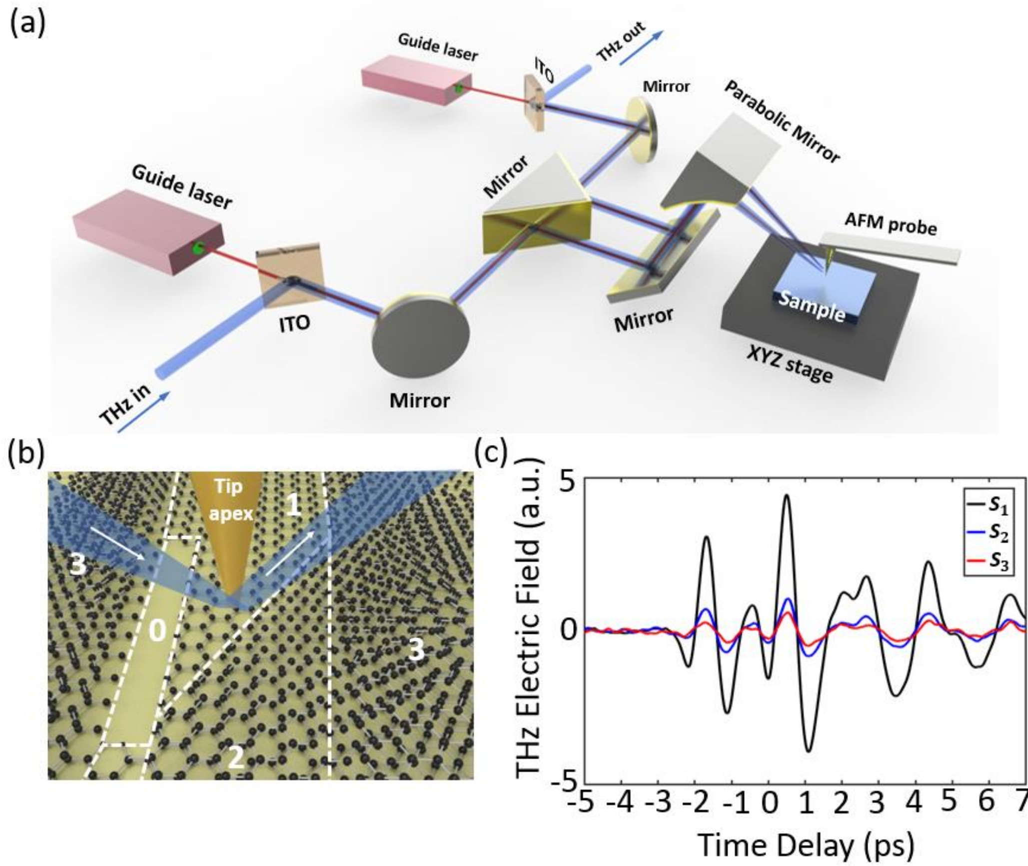

Figure 5.5: (a) Schematic of the THz s-SNOM setup. The Blue (red) beam represents THz (guide) beam path. The THz PCA emitters, receivers, the 800 nm gate beam and the delay stage are omitted from the schematic. The two visible guide lasers are used to trace the THz beam path for THz-tip alignment. (b) Schematic of graphene on SiO_2 with various numbers of layers. The region of the bare SiO_2 area is marked as 0. (c) Demodulated time domain THz signal on a gold film at 1st (S_1), 2nd (S_2), and 3rd (S_3) harmonics of tip-tapping frequency.

THz TDS signals S_1, S_2, and S_3 from a gold film can be obtained by demodulating the detected signal at 1st (Ω), 2nd (2Ω) and 3rd (3Ω) harmonics of the tip tapping frequency. Here S_1 is approximately 3 orders of magnitude smaller than the far-field THz signal and is composed of both near-field and background signal that scattered from the AFM tip shank and cantilever. S_2 is usually 3 to 10 times smaller than S_1 and S_3 2~3 times smaller than S_2, using a typical 100 nm to 180 nm tip tapping amplitude. With a scan rate of 0.03 Hz/line and a lock-in time constant 100 ms, a signal to noise ratio more than 20 for S_2 can be achieved. The

spatial resolution is found to be better than 100 nm. Before taking the near-field images, we maximize the peak of the near-field THz-TDS signal by adjusting the phase of the lock-in amplifier and the time delay. This ensures that we are plotting the spectral integrated peak THz electric field.

5.2.2 Experiments

Using the THz near-field system, nano-imaging of micrometer size graphene samples on SiO_2 (300 nm)/Si substrate is performed. The graphene was mechanically exfoliated onto PDMS (Polydimethylsiloxane) and dry transferred onto a pre-patterned Au lead (30nm thick). Here the Au lead is used for electrostatic gating and serves as a reference for graphene imaging. Fig. 5.6(a) and 5.6(b) show the simultaneously collected AFM topography and near-field images with a size of 10 by 10 μm, respectively. As shown in Fig. 5.6(b), there is clearly a large optical contrast between single layer graphene (SLG, marked as 1) and the SiO_2 substrate (marked as 0). However, no obvious contrasts between SLG and multilayer graphene can be observed (the multilayers are marked by the number of layers as 2, 3, 4 and 5+). Moreover, a comparison between single-layer graphene and a 30-nm gold film revealed comparable THz near-field signals (see Fig. 5.6(c) and 5.6(d)). These observations suggest that monolayer graphene has close-to-perfect near-field THz reflection[182]. This near-unity THz near-field reflectivity is found to be independent of the carrier density when the back-gate voltage is swept between $\pm$30 V at room temperature (RT).

To compare the THz near-field spectra between SiO_2 and graphene, we plot the time domain signal in Fig. 5.6(e) and the Fourier-transformed THz spectrum in Fig. 5.6(f). The normalized THz nano-spectrum S_2 (graphene)/S_2 (SiO_2) reveals that the near-field signal of graphene is 3 to 4 times larger than that on the bare SiO_2 over the 0.2-1 THz frequency range. In the inset of Fig. 5.6(f), the unnormalized spectra of graphene and SiO_2 are plotted. A dip at about 0.75 THz can be observed, which was reported in previous THz near-field experiments[157], [182]. Since this dip is absent in the far-field THz measurements using the same optics but excluding the involvement of the AFM tip, it is considered to be caused by the complex tip-light interactions and can be an interesting point for further investigation.

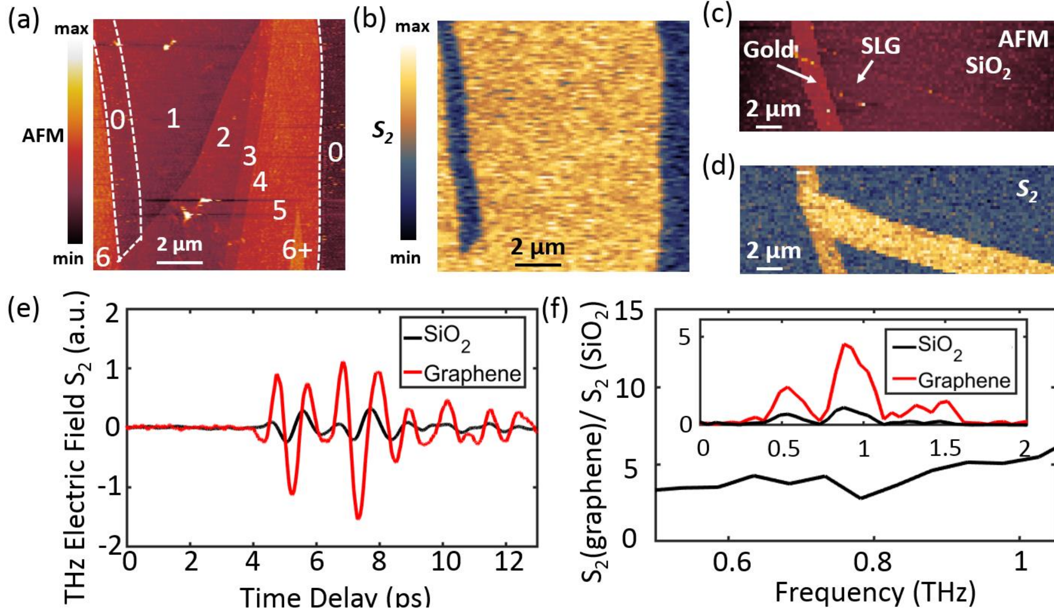

Figure 5.6: (a) and (b), AFM topography and THz near-field (S_2) mapping of graphene on SiO_2, respectively. The numbers of graphene layers are marked in (a), with bare SiO_2 marked as 0. (c) and (d), AFM and THz near-field (S_2) images of a SLG with a gold electrode. The near-field signal in graphene is comparable to that on the thin gold films. (e) Near field THz-TDS signal of SiO_2 (black) and graphene (red). (f) Normalized graphene THz near-field spectrum (to SiO_2). The inset shows a Fast Fourier transform (FFT) of (e), which is the unnormalized S_2 spectra of graphene (red) and SiO_2 (black).

The THz s-SNOM image of graphene is clearly different from those taken at IR frequencies, in which graphene shows distinct near-field reflectivity depending on the layer thickness and stacking[180]. In the theoretical studies of far-field IR or THz properties of graphene, it is customary to consider the momentum-independent optical conductivity[183], [184]. In previous graphene near-field studies in the mid-infrared regime, the momentum-dependence (nonlocal effect) in the conductivity is usually ignored as well[177], [179]. This can be well justified by the fact that at IR frequencies, $\frac{\omega}{q} > v_f$, a local approximation ($\sigma(\omega, q) \approx \sigma(\omega, q{=}0)$) can be applied. Here ω is the frequency of the incident light, v_f is the fermi velocity, and q is the in-plane momentum of the scattered light, which can be on the order of $10^5 - 10^6$ cm^{-1}. However, in the THz regime, due to the low light frequency ω, $\frac{\omega}{q} \leq v_f$, the nonlocal effect is expected to be important, and therefore shall be carefully addressed, as we will practice

below[180], [185]. This “local” and “nonlocal” consideration of graphene is schematically demonstrated in Fig. 5.7(a), which illustrates the dispersion relation of graphene at moderate Fermi energy (~0.1 eV). As shown, a typical IR s-SNOM accesses an energy-momentum space shaded by the green, while a typical THz s-SNOM accesses the space shaded by the yellow, which partially covers the intra-band single particle continuum. The red solid curve displays graphene plasmon dispersion relation which, at IR frequencies, resides nominally in the “local” ($\frac{\omega}{q} > v_f$) regime.

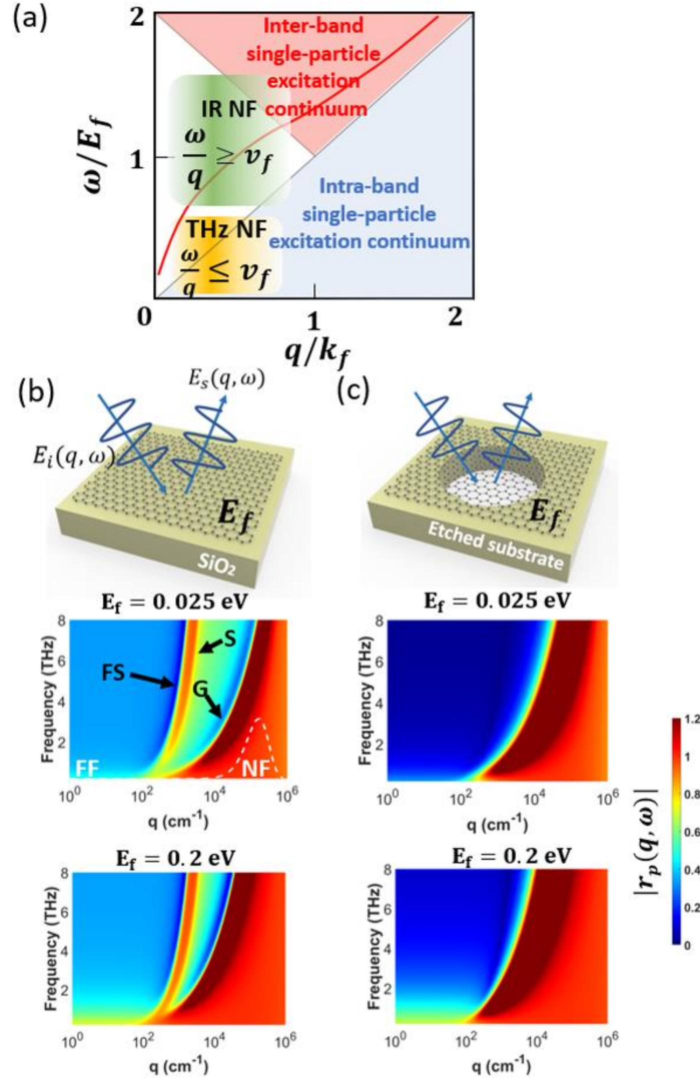

Figure 5.7: (a) Graphene dispersion adopted from Hwang et al[186]. Red curve denotes graphene plasmon dispersion; shaded green region indicates IR near-field accessible regime; shaded yellow region indicates THz near-field accessible regime. (b) and (c) Calculated $|r_p|$ of graphene at the THz range at room temperature using equation (1) to (3). (b) Frequency-momentum dispersion of graphene/(300 nm) SiO_2 with $E_f = 0.025$ eV and $E_f = 0.2$ eV. The tip accessible high momentum region is indicated by the white dashed lines. FF: far-field region. NF: near-field region. FS: light line in free space. S: light line in SiO_2. G: light line in supported graphene. Note the x axis is in log scale. (b) Frequency-momentum dispersion of freestanding graphene with $E_f = 0.025$ eV and $E_f = 0.2$ eV.

5.2.3 Analysis

To understand the high q near-field THz reflectivity, we employ the random phase approximation (RPA) approach, in which the frequency- (ω) and momentum- (q) dependent longitudinal optical conductivity of graphene is given by

$$\sigma(\omega, q) = \frac{ie^2\omega}{q^2}\Pi(\omega, q) \quad (5.1)$$

Π is the density-density response function[185], [186]. With RPA, the conductivity at zero temperature and zero electron interaction has been calculated to be

$$\sigma(\omega, q) = \sigma_0(\omega, q)\left[1 + f\left(\frac{\hbar(\omega + i\tau^{-1}) + 2E_f}{\hbar v_f q}\right) - f\left(\frac{\hbar(\omega + i\tau^{-1}) - 2E_f}{\hbar v_f q}\right)\right] - \frac{2i}{\pi}\frac{e^2\omega E_f}{(\hbar v_f q)^2} \quad (5.2)$$

where e is electron charge, $v_F = 10^6\ m/s$, $k_F = \sqrt{\pi|n|}$ is the Fermi momentum, $E_f = \hbar v_f k_f$ is the Fermi energy, $\tau = 500\ fs$ is the phenomenological relaxation time, corresponding to a carrier mobility of 40,000 cm^2/Vs at carrier density of 10^{12} cm^{-2}, which is kept as a constant for the following calculation. Here we use a relatively high carrier mobility to emphasize the resonant features and their substrate and temperature dependence. With a more realistic τ value (50 fs), which corresponds to a carrier mobility of ~4,000 cm^2/Vs with a carrier density of 10^{12} cm^{-2}, common for graphene on SiO_2, the main conclusion is not altered.

$$\sigma_0(\omega, q) = -i\frac{e^2}{4\hbar}\frac{\omega + i\tau^{-1}}{\sqrt{v_f^2 q^2 - (\omega + i\tau^{-1})^2}} \quad (5.3)$$

is the intrinsic graphene conductivity, and f is defined as $f(x) = -\frac{1}{\pi}(x\sqrt{1 - x^2} - \arccos(x))$. Although finite temperature effect is expected to be relatively small and has no impact on the qualitative features, for the purpose of rigorousness, we invoke the Maldague identity[185], [187] and the temperature dependent graphene conductivity at $T > 0$ can be written as the integral

$$\sigma(\omega, q, ; T, E_f) = \int_{-\infty}^{\infty} dE_f' \frac{\sigma(\omega, q; T = 0, E_f')}{4k_B T cosh^2(\frac{E_f' - E_f}{2k_B T})} \quad (5.4)$$

In graphene, the p-polarized reflection coefficient r_p, which is defined as the ratio of the scattered electric field to incident electric field per unit area, is given by the frequency and momentum dependent Fresnel equation[188]

$$r_p(q,\omega) = \frac{\varepsilon_2 k_1^z - \varepsilon_1 k_2^z + (\frac{4\pi k_1^z k_2^z \sigma}{\omega})}{\varepsilon_2 k_1^z + \varepsilon_1 k_2^z + (\frac{4\pi k_1^z k_2^z \sigma}{\omega})} \tag{5.5}$$

where ε_1 and ε_2 are the permittivity of air and the substrate, $k_i^z = \sqrt{\varepsilon_i \frac{\omega^2}{c^2} - q^2}$ is the out-of-plane momentum in air (i=1) or in the substrate (i=2), and q is the in-plane momentum, the same as defined above. When the absorption is not significant, or, in the graphene case, when it is far away from plasmon dispersion, $r_p(q,\omega)$ has a small imaginary part. Therefore, it is instructive and sufficient to look at the modulus of r_p.

In typical s-SNOM experiments, the accessible in-plane momentum is centered at $q \sim 1/a$, where a is the radius of curvature of the tip apex, which is typically ~10 nm to ~100 nm. More specifically, in a point-dipole approximation, the accessible q in a typical s-SNOM experiments follows a weight function given by $q^2 e^{-2qz_d}$ [188], where z_d is the distance between tip apex and the sample[177], [188], [189]. Assuming $a \approx 50$ nm, the time averaged weight function displays a "bell-shape", which is drawn as white dashed curve in Fig. 5.7(b). Therefore, the most relevant q is in the order of 10^5 cm^{-1} to 10^6 cm^{-1}, much larger than the momentum of the THz light in free space, which is about 10^2 cm^{-1} [188], [189]. For convenience, here we define q > 10^5 cm^{-1} as the "high q" regime, and q < 10^2 cm^{-1} as the "low q" regime. Using above equations, $|r_p(q,\omega)|$ of graphene can be calculated at room temperature with different Fermi levels (e.g. $E_f = 0.025\ eV$ and $E_f = 0.2\ eV$), as shown in Fig. 5.7(b) (graphene on SiO_2) and 5.7(c) (suspended graphene). In graphene on SiO_2, the low q ("far-field") reflectivity $R = |r_p|^2$ is ~20%, while the high q ("near-field") reflection coefficient $|r_p| \approx 1$. Interestingly, in suspended graphene, $|r_p|$ decreases dramatically at low q regime while remains close to unity at moderately high q.

5.2.4 Conclusions

The THz s-SNOM measurements on graphene/SiO_2 at 0.2-1 THz range with < 100 nm spatial resolution shows that graphene has a high near-field reflectivity that is comparable to gold films. The doping level, substrate dielectrics, and temperature have an insignificant effect on the high q response of graphene. The near-unity response results from the unique dielectric properties of graphene and the nature of high momentum optics. Since graphene can be easily made, deformed or transferred onto different surfaces or structures, and most importantly, unlike thick noble metals, graphene does not add edge artifact, it can work as an ideal reference in the future for THz near-field experiments.

(Section 5.2 is based on paper No. 2 in the publication list above.)

Chapter 6

Conclusions and Outlook

This thesis studies the optical microscopy and spectroscopy of correlated electron materials VO_2 and Ca_2RuO_4 using far infrared and terahertz near field probing techniques. The microscopes allow deep subwavelength spatial resolution which is mostly determined by the AFM tip radius (~ 30 nm) regardless of the wavelength of incident light. The deep subwavelength resolution is realized by nonlinear near field interaction between tip apex and sample surface in a highly confined region, which is highly sensitive to the tip-sample distance. The IR s-SNOM is used to image the inhomogeneity of phase transition of transition metal oxides under thermal or electric current excitation, demonstrating rich amount of electronic and structural information of sample surfaces.

The terahertz time domain spectroscopy provides a powerful way of exploring the low energy behaviors in various, with the ultrafast optical pump and terahertz probe, the dynamics of electron excitation and relaxation can be clearly plotted out within the time scale of picoseconds. The OPTP experiment on $V_{1-x}Nb_xO_2$ shows the high tunability of relaxation time by changing the stoichiometric coefficient which has great potential for the development of ultrafast optical switches. The combination of ultrafast optical system with AFM leads to the near field terahertz microscopy and spectroscopy. The study of single layer graphene suggests a near perfect reflectivity of THz wave in the near field regime due to the large increase of light momentum in a confined region around the tip. Future work will be about terahertz near field imaging and OPTP on semiconductor materials due to its high sensitivity to charge carrier densities on the surface. The interface of semiconductor heterojunctions will be excited with optical pump pulses and the response of carriers be probed as an indication of internal electric field and energy level distribution.

With the great success in active s-SNOM, however, the direction exposure of certain samples under probing light may perturb the intrinsic electronic states under measurement, especially for infrared s-SNOMs, giving unreliable information of material properties. To solve this problem, passive infrared SNOM is being developed which directly detects spontaneous surface wave using near field techniques in order to probe genuine local dynamics without external light. The passive IR SNOM will be extremely useful in the thermal designs of detectors and micro-electronics as the functional elements are shrinking to sub-micron scale with the development of modern fabrication techniques, causing serious problems in heat dissipation. For example, in the design of bolometers, thermal conductance of

sensing materials is the most important and tricky factor. The responsivity of the detector (i.e., the amount of output voltage under certain radiation flux) is inversely proportional to the thermal conductance, meaning that a bad thermal isolation is deleterious to the sensitivity. On the other hand, the effective thermal response time, which limits the high frequency performance of thermal detector, is also inversely proportional to thermal conductance. Since a good detector needs response time to be minimized, a large thermal conductance is desirable. This contradiction between high responsivity and response time calls for a careful choice of thermal conductance. For room temperature sensing material, VO_x is the dominantly used, which is a mixture of VO_2, V_2O_3 and V_2O_5. With the help of passive s-SNOM, information of the temperature distribution during IMT are expected to be demonstrated which can help figure out how heat is dissipated during the process and what improvements can be made to optimize it. Besides, since such detector is biased by an electric current, the current induced heat effect also plays a significant role.

Bibliography

[1] M. Vollmer and K.-P. Möllmann, *Infrared Thermal Imaging*. Weinheim, Germany: Wiley-VCH Verlag GmbH & Co. KGaA, 2017.

[2] K. Mangold, J. A. Shaw, and M. Vollmer, “The physics of near-infrared photography,” *Eur. J. Phys.*, vol. 34, no. 6, pp. S51–S71, Nov. 2013.

[3] D. C. Strachan, N. A. Heard, W. J. Hossack, J. F. Boyce, and T. M. Cresswell, “Imaging of hydrocarbon vapours and gases by infrared thermography,” *J. Phys. E.*, vol. 18, no. 6, pp. 492–498, Jun. 1985.

[4] I. F. Akyildiz, J. M. Jornet, and C. Han, “Terahertz band: Next frontier for wireless communications,” *Phys. Commun.*, vol. 12, pp. 16–32, Sep. 2014.

[5] E. Grossman *et al.*, “Passive terahertz camera for standoff security screening,” *Appl. Opt.*, vol. 49, no. 19, p. E106, 2010.

[6] D. Saeedkia, *Handbook of terahertz technology for imaging, sensing and communications*. Woodhead Publishing Limited, 2013.

[7] C. Yu, S. Fan, Y. Sun, and E. Pickwell-Macpherson, “The potential of terahertz imaging for cancer diagnosis: A review of investigations to date.,” *Quant. Imaging Med. Surg.*, vol. 2, no. 1, pp. 33–45, 2012.

[8] E. Hecht, *Optics*. New York, NY: Addison-Wesley, 2002.

[9] N. Ocelic, “Quantitative Near-field Phonon-polariton Spectroscopy,” Verein zur Förderung des Walter Schottky Inst. der Techn. Univ. München e.V., 2007.

[10] L. Novotny, “The history of near-field optics,” in *Progress in Optics*, Elsevier Science, 2007, pp. 137–184.

[11] E. A. Ash and G. Nicholls, “Super-resolution Aperture Scanning Microscope,” *Nature*, vol. 237, no. 5357, pp. 510–512, Jun. 1972.

[12] R. Hillenbrand, T. Taubner, and F. Keilmann, “Phonon-enhanced light matter interaction at the nanometre scale.,” *Nature*, vol. 418, no. 6894, pp. 159–162, 2002.

[13] F. Chudnovskiy, S. Luryi, and B. Spivak, “Switching device based on first-order metal insulator transition induced by external electric field,” in *Future*

Trends in Microelectronics: the Nano Millenium, Wiley-Interscience, 2002, pp. 148–155.

[14] C. Sow *et al.*, “Current-induced strong diamagnetism in the Mott insulator Ca_2RuO_4,” *Science.*, vol. 358, no. 6366, pp. 1084–1087, Nov. 2017.

[15] L. Cario, B. Corraze, A. Meerschaut, and O. Chauvet, “Dielectric breakdown and current switching effect in the incommensurate layered compound $(LaS)_{1.196}VS_2$,” *Phys. Rev. B*, vol. 73, p. 155116, 2006.

[16] S. Yamanouchi, Y. Taguchi, and Y. Tokura, “Dielectric Breakdown of the Insulating Charge-Ordered State in $La_{2-x}Sr_xNiO_4$,” *Phys Rev Lett*, vol. 83, pp. 5555–5558, 1999.

[17] C. Vaju *et al.*, “Electric-pulse-driven electronic phase separation, insulator-metal transition, and possible superconductivity in a mott insulator,” *Adv. Mater.*, vol. 20, no. 14, pp. 2760–2765, 2008.

[18] V. Dubost *et al.*, “Resistive switching at the nanoscale in the Mott insulator compound $GaTa_4Se_8$,” *Nano Lett.*, vol. 13, no. 8, pp. 3648–3653, 2013.

[19] B. Corraze *et al.*, “Electric field induced avalanche breakdown and non-volatile resistive switching in the Mott Insulators AM_4Q_8,” *Eur. Phys. J. Spec. Top.*, vol. 222, no. 5, pp. 1046–1056, 2013.

[20] V. Guiot *et al.*, “Avalanche breakdown in $GaTa_4Se_{8-x}Te_x$ narrow-gap Mott insulators.,” *Nat. Commun.*, vol. 4, p. 1722, 2013.

[21] Y. Taguchi, T. Matsumoto, and Y. Tokura, “Dielectric breakdown of one-dimensional Mott insulators Sr_2CuO_3 and $SrCuO_2$,” *Phys. Rev. B*, vol. 62, no. 11, pp. 7015–7018, Sep. 2000.

[22] M. M. Qazilbash *et al.*, “Mott transition in VO_2 revealed by infrared spectroscopy and nano-imaging.,” *Science*, vol. 318, no. 5857, pp. 1750–3, Dec. 2007.

[23] A. S. McLeod *et al.*, “Nanotextured phase coexistence in the correlated insulator V_2O_3,” *Nat. Phys.*, vol. 13, no. 1, pp. 80–86, Sep. 2016.

[24] J. Zhang *et al.*, “Cooperative photoinduced metastable phase control in strained manganite films,” *Nat. Mater.*, vol. 15, no. 9, pp. 956–960, Sep. 2016.

[25] M. H. Hamidian *et al.*, “Atomic-scale electronic structure of the cuprate d-symmetry form factor density wave state,” *Nat. Phys.*, vol. 12, no. 2, pp.

150–156, Oct. 2015.

[26] C. McGahan *et al.*, "Geometric constraints on phase coexistence in vanadium dioxide single crystals," *Nanotechnology*, vol. 28, no. 8, 2017.

[27] J. Wu, Q. Gu, B. S. Guiton, N. P. De Leon, L. Ouyang, and H. Park, "Strain-induced self organization of metal-insulator domains in single-crystalline VO_2 nanobeams," *Nano Lett.*, vol. 6, no. 10, pp. 2313–2317, 2006.

[28] J. Cao *et al.*, "Extended mapping and exploration of the vanadium dioxide stress-temperature phase diagram," *Nano Lett.*, vol. 10, no. 7, pp. 2667–2673, 2010.

[29] J. Trastoy, Y. Kalcheim, J. del Valle, I. Valmianski, and I. K. Schuller, "Enhanced metal–insulator transition in $V_2O_3$by thermal quenching after growth," *J. Mater. Sci.*, vol. 53, no. 12, pp. 9131–9137, 2018.

[30] S. Nakatsuji, S. I. Ikeda, and Y. Maeno, "Ca_2RuO_4: New Mott Insulators of Layered Ruthenate," *J. Phys. Soc. Japan*, vol. 66, no. 7, pp. 1868–1871, 1997.

[31] C. Alexander *et al.*, "Destruction of the Mott insulating ground state of Ca_2RuO_4 by a structural transition," *Phys. Rev. B*, vol. 60, no. 12, pp. R8422–R8425, 1999.

[32] F. Nakamura *et al.*, "From Mott insulator to ferromagnetic metal: A pressure study of Ca_2RuO_4," *Phys. Rev. B*, vol. 65, no. 22, p. 220402, May 2002.

[33] P. Steffens *et al.*, "High-pressure diffraction studies on Ca_2RuO_4," *Phys. Rev. B*, vol. 72, no. 9, p. 094104, Sep. 2005.

[34] S. Riccò *et al.*, "In situ strain tuning of the metal-insulator-transition of Ca_2RuO_4 in angle-resolved photoemission experiments," *Nat. Commun.*, vol. 9, no. 1, p. 4535, Dec. 2018.

[35] F. Nakamura, M. Sakaki, Y. Yamanaka, S. Tamaru, T. Suzuki, and Y. Maeno, "Electric-field-induced metal maintained by current of the Mott insulator Ca_2RuO_4," *Sci. Rep.*, vol. 3, p. 2536, 2013.

[36] R. Okazaki, Y. Nishina, Y. Yasui, F. Nakamura, T. Suzuki, and I. Terasaki, "Current-induced gap suppression in the mott insulator Ca_2RuO_4," *J. Phys. Soc. Japan*, vol. 82, no. 10, 2013.

[37] J. Bertinshaw *et al.*, "A Unique Crystal Structure of Ca_2RuO_4 in the Current Stabilized Metallic State," *Arxiv*, vol. 1806.06455, 2018.

[38] H. A. Bechtel, E. A. Muller, R. L. Olmon, M. C. Martin, and M. B. Raschke, "Ultrabroadband infrared nanospectroscopic imaging," *Proc. Natl. Acad. Sci.*, vol. 111, no. 20, pp. 7191–7196, May 2014.

[39] J. Zhang *et al.*, "Nano-Resolved Current-Induced Insulator-Metal Transition in the Mott Insulator Ca_2RuO_4," *Phys. Rev. X*, vol. 9, no. 1, p. 011032, Feb. 2019.

[40] M. Braden, G. André, S. Nakatsuji, and Y. Maeno, "Crystal and magnetic structure of Ca_2RuO_4; Magnetoelastic coupling and the metal-insulator transition," *Phys. Rev. B*, vol. 58, no. 2, pp. 847–861, 1998.

[41] M. Sakaki, N. Nakajima, F. Nakamura, Y. Tezuka, and T. Suzuki, "Electric-field-induced insulator–metal transition in Ca_2RuO_4 probed by X-ray absorption and emission spectroscopy," *J. Phys. Soc. Japan*, vol. 82, no. 9, p. 93707, 2013.

[42] Q. Han and A. Millis, "Lattice Energetics and Correlation-Driven Metal-Insulator Transitions: The Case of Ca_2RuO_4," *Phys. Rev. Lett.*, vol. 121, no. 6, p. 067601, Aug. 2018.

[43] T. Mizokawa *et al.*, "Spin-orbit coupling in the Mott insulator Ca_2RuO_4," *Phys. Rev. Lett.*, vol. 87, no. 7, p. 077202, 2001.

[44] E. Gorelov, M. Karolak, T. O. Wehling, F. Lechermann, A. I. Lichtenstein, and E. Pavarini, "Nature of the mott transition in Ca_2RuO_4," *Phys. Rev. Lett.*, vol. 104, no. 22, 2010.

[45] C. G. Fatuzzo *et al.*, "Spin-Orbit-Induced Orbital Excitations in Sr_2RuO_4 and Ca_2RuO_4: A Resonant Inelastic X-ray Scattering Study," *Phys. Rev. B*, vol. 91, no. 15, p. 155104, Mar. 2015.

[46] Ismail, J. Zhang, R. Matzdorf, T. Kimura, Y. Tokura, and E. Plummer, "Surface lattice dynamics of layered transition metal oxides: Sr_2RuO_4 and $La_{0.5}Sr_{1.5}MnO_4$," *Phys. Rev. B*, vol. 67, no. 3, pp. 1–9, 2003.

[47] R. G. Moore *et al.*, "A Surface-Tailored, Purely Electronic, Mott Metal-to-Insulator Transition," *Science.*, vol. 318, no. 5850, pp. 615–619, Oct. 2007.

[48] J. S. Lee *et al.*, "Bond-length dependence of charge-transfer excitations and stretch phonon modes in perovskite ruthenates: Evidence of strong p-d hybridization effects," *Phys. Rev. B*, vol. 70, no. 8, p. 085103, Aug. 2004.

[49] Y. F. Gao, W. Lu, and Z. Suo, "A mesophase transition in a binary

monolayer on a solid surface," *Acta Mater.*, vol. 50, no. 9, pp. 2297–2308, 2002.

[50] O. Friedt, M. Braden, G. Andre, P. Adelmann, S. Nakatsuji, and Y. Maeno, "Structural and magnetic aspects of the metal insulator transition in $Ca_{2-x}Sr_xRuO_4$," *Phys. Rev. B*, vol. 63, no. 17, p. 174432, 2001.

[51] Q. Han and A. Millis, "Lattice Energetics and Correlation-Driven Metal-Insulator Transitions: The Case of Ca_2RuO_4," *Phys. Rev. Lett.*, vol. 121, no. 6, p. 067601, Aug. 2018.

[52] L. M. Zhang *et al.*, "Near-field spectroscopy of silicon dioxide thin films," *Phys. Rev. B*, vol. 85, no. 7, p. 075419, Feb. 2012.

[53] A. A. Govyadinov, S. Mastel, F. Golmar, A. Chuvilin, P. S. Carney, and R. Hillenbrand, "Recovery of permittivity and depth from near-field data as a step toward infrared nanotomography," *ACS Nano*, vol. 8, no. 7, pp. 6911–6921, 2014.

[54] D.-H. Kwon *et al.*, "Atomic structure of conducting nanofilaments in TiO_2 resistive switching memory," *Nat. Nanotechnol.*, vol. 5, no. 2, pp. 148–153, Feb. 2010.

[55] M.-J. Lee *et al.*, "A fast, high-endurance and scalable non-volatile memory device made from asymmetric Ta_2O_{5-x}/TaO_{2-x} bilayer structures," *Nat. Mater.*, vol. 10, no. 8, pp. 625–630, Aug. 2011.

[56] L. Miao *et al.*, "Epitaxial strain effect on transport properties in $Ca_{2-x}Sr_xRuO_4$ thin films," *Phys. Rev. B*, vol. 88, no. 11, p. 115102, 2013.

[57] K. Ando, A.-Q. Liu, and C.-D. Ohl, "Homogeneous Nucleation in Water in Microfluidic Channels," *Phys. Rev. Lett.*, vol. 109, no. 4, p. 044501, Jul. 2012.

[58] M. K. Liu *et al.*, "Anisotropic Electronic State via Spontaneous Phase Separation in Strained Vanadium Dioxide Films," *Phys. Rev. Lett.*, vol. 111, no. 9, p. 096602, Aug. 2013.

[59] D. N. Basov, R. D. Averitt, D. Van Der Marel, M. Dressel, and K. Haule, "Electrodynamics of correlated electron materials," *Rev. Mod. Phys.*, vol. 83, no. 2, pp. 471–541, 2011.

[60] L. Novotny, "The history of near-field optics," in *Progress in Optics*, vol. 50, Elsevier Science, 2007, pp. 137–184.

[61] M. Liu, A. J. Sternbach, and D. N. Basov, "Nanoscale electrodynamics of strongly correlated quantum materials," *Reports Prog. Phys.*, vol. 80, no. 1, p. 014501, Jan. 2017.

[62] F. Keilmann and R. Hillenbrand, "Near-field microscopy by elastic light scattering from a tip.," *Philos. Trans. A. Math. Phys. Eng. Sci.*, vol. 362, no. 1817, pp. 787–805, 2004.

[63] R. Hillenbrand, B. Knoll, and F. Keilmann, "Pure optical contrast in scattering-type scanning near-field microscopy.," *J. Microsc.*, vol. 202, no. Pt 1, pp. 77–83, 2001.

[64] F. Mooshammer *et al.*, "Nanoscale Near-Field Tomography of Surface States on $(Bi_{0.5}Sb_{0.5})_2Te_3$," *Nano Lett.*, vol. 18, no. 12, pp. 7515–7523, Dec. 2018.

[65] J. A. Gerber, S. Berweger, B. T. O'Callahan, and M. B. Raschke, "Phase-Resolved Surface Plasmon Interferometry of Graphene," *Phys. Rev. Lett.*, vol. 113, no. 5, p. 055502, Jul. 2014.

[66] E. A. Muller, B. Pollard, and M. B. Raschke, "Infrared Chemical Nano-Imaging: Accessing Structure, Coupling, and Dynamics on Molecular Length Scales," *J. Phys. Chem. Lett.*, vol. 6, no. 7, pp. 1275–1284, Apr. 2015.

[67] R. Hillenbrand and F. Keilmann, "Complex optical constants on a subwavelength scale," *Phys. Rev. Lett.*, vol. 85, no. 14, pp. 3029–3032, 2000.

[68] R. Hillenbrand and F. Keilmann, "Material-specific mapping of metal/semiconductor/dielectric nanosystems at 10 nm resolution by backscattering near-field optical microscopy," *Appl. Phys. Lett.*, vol. 80, no. 1, pp. 25–27, 2002.

[69] N. Ocelic, A. Huber, and R. Hillenbrand, "Pseudoheterodyne detection for background-free near-field spectroscopy," *Appl. Phys. Lett.*, vol. 89, no. 10, p. 101124, Sep. 2006.

[70] X. G. Xu, M. Rang, I. M. Craig, and M. B. Raschke, "Pushing the sample-size limit of infrared vibrational nanospectroscopy: From monolayer toward single molecule sensitivity," *J. Phys. Chem. Lett.*, vol. 3, no. 13, pp. 1836–1841, 2012.

[71] F. Huth, A. Govyadinov, S. Amarie, W. Nuansing, F. Keilmann, and R. Hillenbrand, "Nano-FTIR absorption spectroscopy of molecular fingerprints

at 20 nm spatial resolution.," *Nano Lett.*, vol. 12, no. 8, pp. 3973–8, 2012.

[72] A. A. Govyadinov, I. Amenabar, F. Huth, P. S. Carney, and R. Hillenbrand, "Quantitative Measurement of Local Infrared Absorption and Dielectric Function with Tip-Enhanced Near-Field Microscopy," *J. Phys. Chem. Lett.*, vol. 4, no. 9, pp. 1526–1531, 2013.

[73] H. A. Bechtel, E. A. Muller, R. L. Olmon, M. C. Martin, and M. B. Raschke, "Ultrabroadband infrared nanospectroscopic imaging," *Proc. Natl. Acad. Sci.*, vol. 111, no. 20, pp. 7191–7196, 2014.

[74] D. N. Basov and T. Timusk, "Electrodynamics of high-Tc superconductors," *Rev. Mod. Phys.*, vol. 77, no. 2, pp. 721–779, Aug. 2005.

[75] M. M. Qazilbash *et al.*, "Electrodynamics of the vanadium oxides VO_2 and V_2O_3," *Phys. Rev. B*, vol. 77, no. 11, p. 115121, 2008.

[76] M. M. Qazilbash *et al.*, "Mott Transition in VO_2 Revealed by Infrared Spectroscopy and Nano-Imaging," *Science.*, vol. 318, no. 5857, pp. 1750–1753, Dec. 2007.

[77] M. M. Qazilbash *et al.*, "Nanoscale imaging of the electronic and structural transitions in vanadium dioxide," *Phys. Rev. B Condens. Matter Mater. Phys.*, vol. 83, no. 16, p. 165108, 2011.

[78] A. C. Jones, S. Berweger, J. Wei, D. Cobden, and M. B. Raschke, "Nano-optical investigations of the metal-insulator phase behavior of individual VO_2 microcrystals.," *Nano Lett.*, vol. 10, no. 5, pp. 1574–81, May 2010.

[79] S. A. Dönges *et al.*, "Ultrafast Nanoimaging of the Photoinduced Phase Transition Dynamics in VO_2," *Nano Lett.*, vol. 16, no. 5, pp. 3029–3035, May 2016.

[80] B. T. O'Callahan, A. C. Jones, J. Hyung Park, D. H. Cobden, J. M. Atkin, and M. B. Raschke, "Inhomogeneity of the ultrafast insulator-to-metal transition dynamics of VO_2," *Nat. Commun.*, vol. 6, no. 1, p. 6849, Nov. 2015.

[81] H. T. Stinson *et al.*, "Infrared nanospectroscopy and imaging of collective superfluid excitations in anisotropic superconductors," *Phys. Rev. B - Condens. Matter Mater. Phys.*, vol. 90, no. 1, pp. 1–10, 2014.

[82] A. Charnukha *et al.*, "Nanoscale layering of antiferromagnetic and superconducting phases in $Rb_2Fe_4Se_5$ single crystals," *Phys. Rev. Lett.*, vol.

109, no. 1, p. 017003, 2012.

[83] B.-Y. Jiang, L. M. Zhang, A. H. Castro Neto, D. N. Basov, and M. M. Fogler, "Generalized spectral method for near-field optical microscopy," *J. Appl. Phys.*, vol. 119, no. 5, p. 054305, 2016.

[84] A. S. McLeod *et al.*, "Model for quantitative tip-enhanced spectroscopy and the extraction of nanoscale-resolved optical constants," *Phys. Rev. B*, vol. 90, no. 8, p. 085136, Aug. 2014.

[85] S. T. Chui, X. Chen, M. Liu, Z. Lin, and J. Zi, "Scattering of electromagnetic waves from a cone with conformal mapping: Application to scanning near-field optical microscope," *Phys. Rev. B*, vol. 97, no. 8, p. 081406, Feb. 2018.

[86] M. M. Qazilbash *et al.*, "Correlated metallic state of vanadium dioxide," *Phys. Rev. B Condens. Matter Mater. Phys.*, vol. 74, no. 20, p. 205118/1-205118/5, 2006.

[87] M. Liu *et al.*, "Symmetry breaking and geometric confinement in VO_2: Results from a three-dimensional infrared nano-imaging," *Appl. Phys. Lett.*, vol. 104, no. 12, p. 121905, Mar. 2014.

[88] M. Liu *et al.*, "Phase transition in bulk single crystals and thin films of VO_2 by nanoscale infrared spectroscopy and imaging," *Phys. Rev. B*, vol. 91, no. 24, p. 245155, Jun. 2015.

[89] B. Lazarovits, K. Kim, K. Haule, and G. Kotliar, "Effects of strain on the electronic structure of VO_2," *Phys. Rev. B*, vol. 81, no. 11, p. 115117, Mar. 2010.

[90] M. Z. Alam, I. De Leon, and R. W. Boyd, "Large optical nonlinearity of indium tin oxide in its epsilon-near-zero region," *Science.*, vol. 352, no. 6287, pp. 795–797, 2016.

[91] K.-L. Yeh, M. C. Hoffmann, J. Hebling, and K. A. Nelson, "Generation of 10μJ ultrashort terahertz pulses by optical rectification," *Appl. Phys. Lett.*, vol. 90, no. 17, p. 171121, Apr. 2007.

[92] M. Bass, P. A. Franken, and J. F. Ward, "Optical Rectification," *Phys. Rev.*, vol. 138, no. 2A, pp. A534–A542, Apr. 1965.

[93] E. Budiarto, J. Margolies, S. Jeong, J. Son, and J. Bokor, "High-intensity terahertz pulses at 1-kHz repetition rate," *IEEE J. Quantum Electron.*, vol. 32, no. 10, pp. 1839–1846, 1996.

[94] J. Hebling, G. Almasi, I. Kozma, and J. Kuhl, "Velocity matching by pulse front tilting for large area THz-pulse generation," *Opt. Express*, vol. 10, no. 21, p. 1161, Oct. 2002.

[95] A. G. Stepanov, L. Bonacina, S. V. Chekalin, and J.-P. Wolf, "Generation of 30 μJ single-cycle terahertz pulses at 100 Hz repetition rate by optical rectification," *Opt. Lett.*, vol. 33, no. 21, p. 2497, Nov. 2008.

[96] Y. Shen *et al.*, "Nonlinear Cross-Phase Modulation with Intense Single-Cycle Terahertz Pulses," *Phys. Rev. Lett.*, vol. 99, no. 4, p. 043901, Jul. 2007.

[97] Spectra-Physics, "Spitfire Ace User's Manual," 2011.

[98] P. C. M. Planken, H.-K. Nienhuys, H. J. Bakker, and T. Wenckebach, "Measurement and calculation of the orientation dependence of terahertz pulse detection in ZnTe," *J. Opt. Soc. Am. B*, 2007.

[99] V. K. Thorsmolle, "Terahertz Time-Domain Spectroscopy of High-Tc Superconductors," University of California, Los Angeles, 2001.

[100] R. A. Kaindl, M. A. Carnahan, D. Hägele, R. Lövenich, and D. S. Chemla, "Ultrafast terahertz probes of transient conducting and insulating phases in an electron–hole gas," *Nature*, vol. 423, no. 6941, pp. 734–738, Jun. 2003.

[101] R. F. Janninck and D. H. Whitmore, "Electrical conductivity and thermoelectric power of niobium dioxide," *J. Phys. Chem. Solids*, vol. 27, no. 6, pp. 1183–1187, Jun. 1966.

[102] A. A. Bolzan, C. Fong, B. J. Kennedy, and C. J. Howard, "A Powder Neutron Diffraction Study of Semiconducting and Metallic Niobium Dioxide," *J. Solid State Chem.*, vol. 113, no. 1, pp. 9–14, 1994.

[103] A. K. Cheetham and C. N. R. Rao, "A neutron diffraction study of niobium dioxide," *Acta Crystallogr. Sect. B*, vol. 32, no. 5, pp. 1579–1580, May 1976.

[104] R. Pynn, J. D. Axe, and R. Thomas, "Structural distortions in the low-temperature phase of NbO_2 dagger," *Phys. Rev. B*, vol. 13, no. 7, pp. 2965–2975, 1976.

[105] S. Kim *et al.*, "Threshold-switching characteristics of a nanothin-NbO2-layer-based Pt/NbO_2/Pt stack for use in cross-point-type resistive memories," *Microelectron. Eng.*, vol. 107, pp. 33–36, Jul. 2013.

[106] H. R. Philipp and L. M. Levinson, "NbO_2 devices for subnanosecond transient protection," *J. Appl. Phys.*, vol. 50, no. 7, pp. 4814–4822, Jul. 1979.

[107] "Threshold Switching Characteristics of Nb/NbO_2/TiN Vertical Devices," *IEEE J. Electron Devices Soc.*, vol. 4, no. 1, pp. 11–14, Jan. 2016.

[108] M. R. Beebe *et al.*, "Time-resolved light-induced insulator-metal transition in niobium dioxide and vanadium dioxide thin films," *Opt. Mater. Express*, vol. 7, no. 1, pp. 213–223, Jan. 2017.

[109] L. A. Ladd and W. Paul, "Optical and transport properties of high quality crystals of V_2O_4 near the metallic transition temperature," *Solid State Commun.*, vol. 7, no. 4, pp. 425–428, Feb. 1969.

[110] T. Sakata, K. Sakata, and I. Nishida, "Study of Phase Transition in NbO_2," *Phys. status solidi*, vol. 20, no. 2, pp. K155–K157, 1967.

[111] D. J. Hilton *et al.*, "Enhanced Photosusceptibility near Tc for the Light-Induced Insulator-to-Metal Phase Transition in Vanadium Dioxide," *Phys. Rev. Lett.*, vol. 99, no. 22, p. 226401/1-226401/4, Nov. 2007.

[112] A. Cavalleri *et al.*, "Femtosecond structural dynamics in VO_2 during an ultrafast solid-solid phase transition," *Phys. Rev. Lett.*, vol. 87, no. 23, p. 237401, 2001.

[113] M. Liu *et al.*, "Terahertz-field-induced insulator-to-metal transition in vanadium dioxide metamaterial," *Nature*, vol. 487, no. 7407, pp. 345–348, Jul. 2012.

[114] M. Rini *et al.*, "Optical switching in VO2 films by below-gap excitation," *Appl. Phys. Lett.*, vol. 92, no. 18, p. 181904, May 2008.

[115] A. Cavalleri, T. Dekorsy, H. H. W. Chong, J. C. Kieffer, and R. W. Schoenlein, "Evidence for a structurally-driven insulator-to-metal transition in VO_2 : A view from the ultrafast timescale," *Phys. Rev. B*, vol. 70, no. 16, p. 161102, Oct. 2004.

[116] S. Lysenko, A. Rúa, V. Vikhnin, F. Fernández, and H. Liu, "Insulator-to-metal phase transition and recovery processes in VO_2 thin films after femtosecond laser excitation," *Phys. Rev. B*, vol. 76, no. 3, p. 035104, Jul. 2007.

[117] Y. Zhou, X. Chen, C. Ko, Z. Yang, C. Mouli, and S. Ramanathan, "Voltage-Triggered Ultrafast Phase Transition in Vanadium Dioxide Switches," *IEEE Electron Device Lett.*, vol. 34, no. 2, pp. 220–222, Feb. 2013.

[118] M. D. Pickett and R. Stanley Williams, "Sub-100 fJ and sub-nanosecond

thermally driven threshold switching in niobium oxide crosspoint nanodevices," *Nanotechnology*, vol. 23, no. 21, p. 215202, Jun. 2012.

[119] H. Wen *et al.*, "Structural and electronic recovery pathways of a photoexcited ultrathin VO_2 film," *Phys. Rev. B - Condens. Matter Mater. Phys.*, vol. 88, no. 16, 2013.

[120] S. Nakamura, Y. Ueno, and K. Tajima, "Ultrafast (200-fs switching, 1.5-Tb/s demultiplexing) and high-repetition (10 GHz) operations of a polarization-discriminating symmetric Mach-Zehnder all-optical switch," *IEEE Photonics Technol. Lett.*, vol. 10, no. 11, pp. 1575–1577, Nov. 1998.

[121] A. V. Gopal, H. Yoshida, A. Neogi, N. Georgiev, and T. Mozume, "Intersubband absorption saturation in InGaAs-AlAsSb quantum wells," *IEEE J. Quantum Electron.*, vol. 38, no. 11, pp. 1515–1520, Nov. 2002.

[122] D. H. Auston, *Ultrashort Laser Pulses*, vol. 60. Berlin, Heidelberg: Springer Berlin Heidelberg, 1993.

[123] R. Rana, J. M. Klopf, J. Grenzer, H. Schneider, M. Helm, and A. Pashkin, "Nonthermal nature of photoinduced insulator-to-metal transition in NbO_2," *Phys. Rev. B*, vol. 99, no. 4, p. 041102, Jan. 2019.

[124] K. G. West *et al.*, "Growth and characterization of vanadium dioxide thin films prepared by reactive-biased target ion beam deposition," *J. Vac. Sci. Technol. A*, vol. 26, no. 1, pp. 133–139, 2008.

[125] Y. Wang, R. B. Comes, S. Kittiwatanakul, S. A. Wolf, and J. Lu, "Epitaxial niobium dioxide thin films by reactive-biased target ion beam deposition," *J. Vac. Sci. Technol. A*, vol. 33, no. 2, p. 021516, 2015.

[126] K. G. West *et al.*, "Ferromagnetism in rutile structure Cr doped VO_2 thin films prepared by reactive-bias target ion beam deposition," *J. Supercond. Nov. Magn.*, vol. 21, no. 2, pp. 87–92, 2008.

[127] M. E. A. Warwick and R. Binions, "Advances in thermochromic vanadium dioxide films," *J. Mater. Chem. A*, vol. 2, no. 10, pp. 3275–3292, 2014.

[128] A. Zylbersztejn and N. F. Mott, "Metal-insulator transition in vanadium dioxide," *Phys. Rev. B*, vol. 11, no. 11, pp. 4383–4395, Jun. 1975.

[129] F. J. Wong, N. Hong, and S. Ramanathan, "Orbital splitting and optical conductivity of the insulating state of NbO_2," *Phys. Rev. B*, vol. 90, no. 11, p. 115135, Sep. 2014.

[130] M. Pan *et al.*, “Raman study of the phase transition in VO_2 thin films,” *J. Cryst. Growth*, vol. 268, no. 1, pp. 178–183, Jul. 2004.

[131] T. L. Cocker *et al.*, “Phase diagram of the ultrafast photoinduced insulator-metal transition in vanadium dioxide,” *Phys. Rev. B*, vol. 85, no. 15, p. 155120, Apr. 2012.

[132] C. Marini *et al.*, “Optical properties of $V_{1-x}Cr_xO_2$ compounds under high pressure,” *Phys. Rev. B*, vol. 77, no. 23, p. 235111, Jun. 2008.

[133] Y. Li, Y. Liu, J. Liu, and L. Ren, “The effects of niobium on the structure and properties of VO_2 films,” *J. Mater. Sci. Mater. Electron.*, vol. 27, no. 5, pp. 4981–4987, May 2016.

[134] J. H. Claassen, J. W. Lu, K. G. West, and S. A. Wolf, “Relaxation dynamics of the metal-semiconductor transition in VO_2 thin films,” *Appl. Phys. Lett.*, vol. 96, no. 13, p. 132102, Mar. 2010.

[135] R. D. Shannon, “Revised effective ionic radii and systematic studies of interatomic distances in halides and chalcogenides,” *Acta Crystallogr. Sect. A*, vol. 32, no. 5, pp. 751–767, 1976.

[136] P. Lederer, H. Launois, J. P. Pouget, A. Casalot, and G. Villeneuve, “Contribution to the study of the metal-insulator transition in the $V_{1-x}Nb_xO_2$ system—III theoretical discussion,” *J. Phys. Chem. Solids*, vol. 33, no. 10, pp. 1969–1978, 1972.

[137] G. Villeneuve, A. Bordet, A. Casalot, J. P. Pouget, H. Launois, and P. Lederer, “Contribution to the study of the metal-insulator transition in the $V_{1-x}Nb_xO_2$ system: I — crystallographic and transport properties,” *J. Phys. Chem. Solids*, vol. 33, no. 10, pp. 1953–1959, 1972.

[138] C. J. Patridge, L. Whittaker, B. Ravel, and S. Banerjee, “Elucidating the Influence of Local Structure Perturbations on the Metal–Insulator Transitions of $V_{1-x}Nb_xO_2$ Nanowires: Mechanistic Insights from an X-ray Absorption Spectroscopy Study,” *J. Phys. Chem. C*, vol. 116, no. 5, pp. 3728–3736, Feb. 2012.

[139] Y. Wu *et al.*, “Depressed transition temperature of $W_xV_{1-x}O_2$: mechanistic insights from the X-ray absorption fine structure (XAFS) spectroscopy,” *Phys. Chem. Chem. Phys.*, vol. 16, no. 33, pp. 17705–17714, 2014.

[140] X. Tan *et al.*, “Unraveling Metal-insulator Transition Mechanism of VO_2 Triggered by Tungsten Doping,” *Sci. Rep.*, vol. 2, no. 1, pp. 466–466, 2012.

[141] H. Oppermann, F. von Woedtke, T. Reich, M. A. Denecke, H. Nitsche, and M. Doerr, “Phase relations in the system V/Nb/O. V. Investigation of mixed crystals $V_{1-x}Nb_xO_2$,” *Fresenius. J. Anal. Chem.*, vol. 363, no. 2, pp. 202–205, Jan. 1999.

[142] V. Eyert, “The metal-insulator transitions of VO_2: A band theoretical approach,” *Ann. Phys.*, vol. 11, no. 9, pp. 650–704, 2002.

[143] D. Ruzmetov and S. Ramanathan, “Metal-Insulator Transition in Thin Film Vanadium Dioxide,” in *Thin Film Metal-Oxides: Fundamentals and Applications in Electronics and Energy*, S. Ramanathan, Ed. Boston, MA: Springer US, 2010, pp. 51–94.

[144] J. B. Goodenough, “The two components of the crystallographic transition in VO_2,” *J. Solid State Chem.*, vol. 3, no. 4, pp. 490–500, 1971.

[145] W. Brito, M. Aguiar, K. Haule, and G. Kotliar, “Dynamic electronic correlation effects in NbO_2 as compared to VO_2,” *Phys. Rev. B*, vol. 96, no. 19, p. 195102, 2017.

[146] C. N. R. Rao, G. R. Rao, and G. V. S. Rao, “Semiconductor-metal transitions in NbO_2 and $Nb_{1-x}V_xO_2$,” *J. Solid State Chem.*, vol. 6, no. 3, pp. 340–343, Mar. 1973.

[147] S. Nakao, H. Kamisaka, Y. Hirose, and T. Hasegawa, “Structural, electrical, and optical properties of polycrystalline NbO_2 thin films grown on glass substrates by solid phase crystallization,” *Phys. status solidi*, vol. 214, no. 3, p. 1600604, Nov. 2016.

[148] A. O’Hara, T. N. Nunley, A. B. Posadas, S. Zollner, and A. A. Demkov, “Electronic and optical properties of NbO_2,” *J. Appl. Phys.*, vol. 116, no. 21, p. 213705, Dec. 2014.

[149] J. Lourembam, A. Srivastava, C. La-o-vorakiat, L. Cheng, T. Venkatesan, and E. E. M. Chia, “Evidence for Photoinduced Insulator-to-Metal transition in B-phase vanadium dioxide,” *Sci. Rep.*, vol. 6, p. 25538, 2016.

[150] A. Pashkin *et al.*, “Ultrafast insulator-metal phase transition in VO_2 studied by multiterahertz spectroscopy,” *Phys. Rev. B*, vol. 83, no. 19, p. 195120, May 2011.

[151] P. Baum, D.-S. Yang, and A. H. Zewail, “4D Visualization of Transitional Structures in Phase Transformations by Electron Diffraction,” *Science.*, vol. 318, no. 5851, pp. 788–792, 2007.

[152] V. R. Morrison *et al.*, “A photoinduced metal-like phase of monoclinic VO_2 revealed by ultrafast electron diffraction,” *Science.*, vol. 346, no. 6208, pp. 445–448, 2014.

[153] N. C. J. van der Valk and P. C. M. Planken, “Electro-optic detection of subwavelength terahertz spot sizes in the near field of a metal tip,” *Appl. Phys. Lett.*, vol. 81, no. 9, pp. 1558–1560, Aug. 2002.

[154] H.-T. Chen, R. Kersting, and G. C. Cho, “Terahertz imaging with nanometer resolution,” *Appl. Phys. Lett.*, vol. 83, no. 15, p. 3009, 2003.

[155] A. J. Huber, F. Keilmann, J. Wittborn, J. Aizpurua, and R. Hillenbrand, “Terahertz near-field nanoscopy of mobile carriers in single semiconductor nanodevices,” *Nano Lett.*, vol. 8, no. 11, pp. 3766–3770, 2008.

[156] N. M. Burford and M. O. El-Shenawee, “Review of terahertz photoconductive antenna technology,” *Opt. Eng.*, vol. 56, no. 1, p. 010901, Jan. 2017.

[157] H. T. Stinson *et al.*, “Imaging the nanoscale phase separation in vanadium dioxide thin films at terahertz frequencies,” *Nat. Commun.*, vol. 9, no. 1, p. 3604, Dec. 2018.

[158] Y. Sun, M. Y. Sy, Y.-X. J. Wang, A. T. Ahuja, Y.-T. Zhang, and E. Pickwell-Macpherson, “A promising diagnostic method: Terahertz pulsed imaging and spectroscopy,” *World J. Radiol.*, vol. 3, no. 3, p. 55, Mar. 2011.

[159] T. Nagatsuma, G. Ducournau, and C. C. Renaud, “Advances in terahertz communications accelerated by photonics,” *Nat. Photonics*, vol. 10, no. 6, pp. 371–379, Jun. 2016.

[160] A. G. Markelz, A. Roitberg, and E. J. Heilweil, “Pulsed terahertz spectroscopy of DNA, bovine serum albumin and collagen between 0.1 and 2.0 THz,” *Chem. Phys. Lett.*, vol. 320, no. March, pp. 42–48, 2000.

[161] A. Markelz, S. Whitmire, J. Hillebrecht, and R. Birge, “THz time domain spectroscopy of biomolecular conformational modes,” *Phys. Med. Biol.*, vol. 47, no. 21, pp. 3797–3805, 2002.

[162] Z. Zhou *et al.*, “Multicolor T-Ray Imaging Using Multispectral Metamaterials,” *Adv. Sci.*, vol. 5, no. 7, p. 1700982, Jul. 2018.

[163] H. Nakanishi, S. Fujiwara, K. Takayama, I. Kawayama, H. Murakami, and M. Tonouchi, “Imaging of a polycrystalline silicon solar cell using a laser

terahertz emission microscope," *Appl. Phys. Express*, vol. 5, no. 11, 2012.

[164] P. U. Jepsen, D. G. Cooke, and M. Koch, "Terahertz spectroscopy and imaging - Modern techniques and applications," *Laser Photonics Rev.*, vol. 5, no. 1, pp. 124–166, 2011.

[165] D. Suzuki, S. Oda, and Y. Kawano, "A flexible and wearable terahertz scanner," *Nat. Photonics*, vol. 10, no. 12, pp. 809–813, 2016.

[166] C. Liewald, S. Mastel, J. Hesler, A. J. Huber, R. Hillenbrand, and F. Keilmann, "All-electronic terahertz nanoscopy," *Optica*, vol. 5, no. 2, p. 159, 2018.

[167] H. T. Stinson *et al.*, "Imaging the nanoscale phase separation in vanadium dioxide thin films at terahertz frequencies," *Nat. Commun.*, vol. 9, no.1, p. 3604, Dec. 2018.

[168] F. Kuschewski, H. G. Von Ribbeck, J. Döring, S. Winnerl, L. M. Eng, and S. C. Kehr, "Narrow-band near-field nanoscopy in the spectral range from 1.3 to 8.5 THz," *Appl. Phys. Lett.*, vol. 108, no. 11, 2016.

[169] M. Hasan, S. Arezoomandan, H. Condori, and B. Sensale-Rodriguez, "Graphene terahertz devices for communications applications," *Nano Commun. Netw.*, vol. 10, pp. 68–78, 2016.

[170] P. Tassin, T. Koschny, and C. M. Soukoulis, "Graphene for terahertz applications," *Science*, vol. 341, no. 6146. pp. 620–621, 2013.

[171] B. Sensale-Rodriguez *et al.*, "Broadband graphene terahertz modulators enabled by intraband transitions," *Nat. Commun.*, vol. 3, no. 1, p. 780, Jan. 2012.

[172] T. Palacios, A. Hsu, and H. Wang, "Applications of graphene devices in RF communications," *IEEE Commun. Mag.*, vol. 48, no. 6, pp. 122–128, 2010.

[173] T. Mueller, F. Xia, and P. Avouris, "Graphene photodetectors for high-speed optical communications," *Nat. Photonics*, vol. 4, no. 5, pp. 297–301, 2010.

[174] M. Mittendorff, S. Li, and T. E. Murphy, "Graphene-Based Waveguide-Integrated Terahertz Modulator," *ACS Photonics*, vol. 4, no. 2, pp. 316–321, 2017.

[175] C. X. Zhao, W. Xu, L. L. Li, C. Zhang, and F. M. Peeters, "Terahertz plasmon-polariton modes in graphene driven by electric field inside a Fabry-Pérot cavity," *J. Appl. Phys.*, vol. 117, no. 22, 2015.

[176] X. Gu, I. T. Lin, and J. M. Liu, "Extremely confined terahertz surface plasmon-polaritons in graphene-metal structures," *Appl. Phys. Lett.*, vol. 103, no. 7, 2013.

[177] Z. Fei *et al.*, "Gate-tuning of graphene plasmons revealed by infrared nano-imaging," *Nature*, vol. 486, no. 7405, pp. 82–85, 2012.

[178] A. Y. Nikitin, F. Guinea, F. J. García-Vidal, and L. Martín-Moreno, "Edge and waveguide terahertz surface plasmon modes in graphene microribbons," *Phys. Rev. B - Condens. Matter Mater. Phys.*, vol. 84, no. 16, 2011.

[179] J. Chen *et al.*, "Optical nano-imaging of gate-tunable graphene plasmons," *Nature*, vol. 487, no. 7405, pp. 77–81, 2012.

[180] D.-S. Kim *et al.*, "Stacking Structures of Few-Layer Graphene Revealed by Phase-Sensitive Infrared Nanoscopy," *ACS Nano*, vol. 9, no. 7, pp. 6765–6773, Jul. 2015.

[181] M. Honig, J. A. Sulpizio, J. Drori, A. Joshua, E. Zeldov, and S. Ilani, "Local electrostatic imaging of striped domain order in $LaAlO_3/SrTiO_3$," *Nat. Mater.*, vol. 12, no. 12, pp. 1112–1118, Dec. 2013.

[182] S. Mastel *et al.*, "Terahertz Nanofocusing with Cantilevered Terahertz-Resonant Antenna Tips," *Nano Lett.*, vol. 17, no. 11, pp. 6526–6533, 2017.

[183] A. Andryieuski and A. V. Lavrinenko, "Graphene metamaterials based tunable terahertz absorber: effective surface conductivity approach," *Opt. Express*, vol. 21, no. 7, p. 9144, 2013.

[184] I. Llatser, C. Kremers, A. Cabellos-Aparicio, J. M. Jornet, E. Alarcón, and D. N. Chigrin, "Graphene-based nano-patch antenna for terahertz radiation," in *Photonics and Nanostructures - Fundamentals and Applications*, 2012, vol. 10, no. 4, pp. 353–358.

[185] M. B. Lundeberg *et al.*, "Tuning quantum nonlocal effects in graphene plasmonics," *Science.*, vol. 357, no. 6347, pp. 187–191, 2017.

[186] E. H. Hwang and S. Das Sarma, "Dielectric function, screening, and plasmons in two-dimensional graphene," *Phys. Rev. B - Condens. Matter Mater. Phys.*, vol. 75, no. 20, 2007.

[187] E. Sugawara and H. Nikaido, "Properties of AdeABC and AdeIJK efflux systems of Acinetobacter baumannii compared with those of the AcrAB-TolC system of Escherichia coli.," *Antimicrob. Agents Chemother.*, vol. 58,

no. 12, pp. 7250–7, Dec. 2014.

[188] Z. Fei *et al.*, “Infrared nanoscopy of dirac plasmons at the graphene-SiO_2 interface,” *Nano Lett.*, vol. 11, no. 11, pp. 4701–4705, 2011.

[189] S. Dai *et al.*, “Tunable Phonon Polaritons in Atomically Thin van der Waals Crystals of Boron Nitride,” *Science.*, vol. 343, no. 6175, pp. 1125–1129, Mar. 2014.